D I P L O M A R B E I T

Experimental and Computational Assessment of Aircrew Radiation Exposure

Ausgeführt am Atominstitut
der Technischen Universität Wien

unter der Anleitung von
Univ.Prof. Dipl.-Ing. Dr.techn. Norbert Vana und
Univ.Ass. Dipl.-Ing. Dr.techn. Michael Hajek
als verantwortlich mitwirkenden Universitätsassistenten

durch
Georg Eigelsreiter
1020 Wien, Vorgartenstraße 221/1/12

Wien, am 29. April 2011 ……..……..……...

Abstract

Experimental and Computational Assessment of Aircrew Radiation Exposure

Aircrew personnel is exposed to radiation levels from cosmic rays that on average are equal to or higher than other occupationally exposed personnel receives from artificial sources in medicine, industry and technology. In a pilot experiment in cooperation with *Tyrolean Airways*, the radiation exposure on short and midrange operations has been evaluated. Experimental data have been compared with results from CARI 6, a computation system using Monte Carlo calculation codes in order to calculate aircrew radiation exposure. Austrian legislation defines computer-based dose assessment as an appropriate means of radiation protection as long as the calculations agree within 30% with experimental data. For the experimental assessment of the cosmic ray induced dose, thermoluminescence dosimetry has been used. This is a common method in personal dosimetry. Additionally to the overall exposure, the neutron contribution has been determined by the extended pair method using TLD-600/700 dosemeters. Beside these lithium fluoride phosphors, calcium fluoride dosemeters (TLD-300) have been used to evaluate their reproducibility and applicability to personal dosimetry of aircraft crew. Results provided by the CARI 6 code have been analyzed in comparison with the experimental data from the different types of thermoluminescence dosemeters.

Zusammenfassung

Experimentelle und computerunterstützte Erfassung der Strahlenexposition des fliegenden Personals

Fliegendes Personal ist einer Strahlenbelastung durch Höhenstrahlung ausgesetzt, die im Durchschnitt vergleichbar oder sogar höher ist als jene, welche andere strahlenexponierte Personen in Medizin, Industrie und Technik erhalten. In einem Pilotexperiment in Kooperation mit *Tyrolean Airways* wurde die Strahlenbelastung auf Kurz- und Mittelstreckenflügen bewertet. Die experimentellen Daten wurden mit Ergebnissen von CARI 6 verglichen, einem Computerprogramm, welches mittels Monte-Carlo-Simulation die Strahlenexposition von fliegendem Personal berechnet. Die österreichische Gesetzgebung genehmigt die computerunterstützte Dosiserfassung als ausreichende Strahlenschutzmaßnahme, solange die Berechnungen innerhalb von 30% mit experimentellen Daten übereinstimmen. Zur experimentellen Erfassung der durch Höhenstrahlung bedingten Dosis wurde Thermolumineszenzdosimetrie verwendet, eine weit verbreitete Methode in der Personendosimetrie. Zusätzlich zur gesamten Exposition wurde der Neutronenanteil mit Hilfe der erweiterten Paarmethode auf der Grundlage von TLD-600/700 gemessen. Neben diesen beiden Lithiumfluorid-Dosimetern wurden zusätzlich Kaliziumfluorid-Dosimeter des Typs TLD-300 verwendet, um ihre Reproduzierbarkeit und Anwendbarkeit in der Personendosimetrie von Flugzeugbesatzungen zu überprüfen. Die Ergebnisse von CARI 6 wurden im Vergleich mit den experimentellen Daten der verschiedenen Thermolumineszenzdosimetertypen analysiert.

Contents

Chapter 1

Introduction

1.1 Motivation

Due to the increasing importance of aviation in modern transportation, aircrew radiation exposure has become a matter of growing interest. On average, aircrew personnel is exposed to radiation levels from cosmic rays that are equal to or higher than other occupationally exposed personnel receives from artificial sources in medicine, industry and technology. In 1990, the *International Commission on Radiological Protection (ICRP)* first published recommendations for limiting radiation exposure of aircrew. Six years later, the European Union decreed the *Council Directive 96/29/EURATOM* of 13 May 1996 [1], laying down basic safety standards for the protection of the health of workers and the general public against the dangers arising from ionizing radiation. The Austrian government implemented this European law by amendment of the national legislation on 20 August 2002 (Strahlenschutz-EU-Anpassungsgesetz 2002, BGBl. I Nr. 146/2002), 10 December 2004 (Strahlenschutz-EU-Anpassungsgesetz 2004, BGBl. I Nr. 137/2004) and 22 May 2006 (Allgemeine Strahlenschutzverordnung, BGBl. II Nr. 191/2006), including a supplement for aircrew (Strahlenschutzverordnung fliegendes Personal, BGBl. II Nr. 235/2006a) issued on 22 June 2006. According to this legislation, it is the responsibility of an airline operator to ensure that the radiation exposure received by aircrew members is kept as low as reasonably achievable (ALARA) with respect to the state of technology under consideration of economic and social factors. The accurate assessment of the complex radiation environment usually requires a high effort of instrumentation. The "*Institute of Atomic and Subatomic Physics*" developed an experimental dosemeter system based on thermoluminescence. Thermoluminescence is the thermally stimulated emission of light following the previous absorption of energy from ionizing radiation. Only electrical insulators (or – under special conditions irrelevant to practical applications – semiconductors) may exhibit

thermoluminescence. The most frequently used phosphor is lithium fluoride doped with magnesium and titanium. In this study, two types of this material have been used. Both types have the same structure except for their enrichment in different lithium isotopes. This allows – beneath the measurement of the total absorbed dose – an evaluation of the neutron and non-neutron contributions to dose by means of the "extended pair method", exploiting different neutron sensitivities of the dosemeters. Beside the lithium fluoride phosphors another – more sensitive – dosemeter material based on calcium fluoride doped with thulium has been tested for its reliability in routine measurements of cosmic radiation. Generally, thermoluminescence dosemeters are toxicologically harmless, do not require energy supply nor emit any electromagnetic radiation that could interfere with aircraft electronics. This is why this system is completely passive and does not require special aviation certification. The experimental data have been compared with results from CARI 6, one of the most frequently used computation programs worldwide to calculate radiation exposure on different flight routes. The CARI 6 code, developed at the *Federal Aviation Administration (FAA) Civil Aerospace Medical Institute*, calculates the effective dose from cosmic radiation received by an individual (based on an anthropomorphic phantom) on an aircraft flying a geodesic route between any two airports in the world. The program takes into account changes in altitude and geographic location during the course of a flight, as derived from the flight profile entered by the user. It has been certificated by several nations as a reasonably accurate method for airlines to calculate the radiation exposure received by their personnel. The Austrian legislation allows computer-based calculation as an exclusive source for dose assessment of aircrew personnel, if agreement within ± 30% – compared with experimental techniques – can be ensured. This thesis describes the pilot experiment in cooperation with pilots of *Tyrolean Airways /Austrian Arrows*. The received radiation exposure was measured and calculated on short and mid-range operations of the different *Tyrolean Airways* fleets, *Bombardier Dash 8-Q300/400*, *Bombardier Canadair Regional Jet (CRJ)-100/200* and *Fokker 70/100*.

1.2 Organization of the Thesis

Cosmic Radiation. Chapter 2 will review the properties of cosmic radiation. To be assessed are the origin of the radiation, its acceleration and the interaction processes in the Earth's atmosphere. The secondary radiation field within the atmosphere and the different components of an air shower are described in detail.

Radiation Dosimetry and Effects. The third chapter starts with an introduction of basic quantities and units in dosimetry. Various quantities are used to describe physical properties of a radiation

field, the energy deposition by ionizing radiation or involved risks for biological organisms. In the second part of this chapter, the effects of radiation on humans are presented from the initial ionization of the target structure, via the physical, chemical and biological processes up to deterministic and stochastic radiation effects on the whole organism. Concluding, results of cohort studies, which investigate statistical relations of cosmic radiation and cancer incidence are presented.

Thermoluminescence Dosimetry. The principles of thermoluminescence are described within the energy band model of solid-state crystals. Evaluation of a thermoluminescence dosemeter is implemented by measurement of the light emitted during an appropriate heating process. The light intensity over temperature represents the so-called glow curve. It is shown that simplified theoretical models can approximate the shape of an actual glow curve by appropriate evaluation of the model parameters. Additionally to the theoretical models, in this chapter, the compositions of the used dosemeters are explained. Besides their characteristics and practicability, the extended pair method is explained that allows to differentiate the neutron contribution in the measured overall exposure.

Experimental Assessment. The experimental assessment of cosmic radiation was accomplished by thermoluminescence dosemeters of the types TLD-600/700 and TLD-300. Forty DOSFLIP dosemeter packages were used in three periods on all three Tyrolean Airway fleets, Dash 8, CRJ and Fokker 70/100. The results are presented for each package as the total absorbed dose (rate) and the neutron component of the radiation field. Parallel to the established TLD-600/700 dosimetry, the TLD-300 dosemeters were analyzed to examine its applicability to personal dosimetry of aircrew.

Computational Assessment. The computational assessment is based on CARI 6, which is one the worldwide most frequently used computer programs to calculate radiation exposure of aircrew. CARI 6 is based on Monte Carlo calculations of the effective doses on the shortest – geodesic – route between any two airports in a database using as input flight time, altitudes and geomagnetic cut-off rigidity. The results are presented and compared to the experimental data.

Chapter 2

Cosmic Radiation

2.1 Introduction

The Austrian physicist and Nobel laureate, Victor Hess, discovered cosmic radiation during ballooning experiments [2] in the early 20th century. He detected that the intensity of ionizing radiation rises with increasing altitude and attributed this to an additional source of radiation from outside the Earth's atmosphere. Outside the atmosphere, cosmic rays can be classified in solar, galactic and geomagnetically trapped radiation (see Figure 2-1). Through interaction with the Earth's atmosphere, air showers, a cascade of secondary particles, are created. This secondary radiation is a function of altitude, geomagnetic latitude and solar activity. Some of the secondary particles have a high biological effectiveness. The maximum of the radiation exposure is found at altitudes between 12 and 20 kilometers above sea level. In modern aviation, these altitudes are used primarily for cruise flights. Therefore, the radiation exposure received on civil flights is of special interest.

2.2 Space Radiation

Highly energetic particles from outside the Earth's atmosphere continuously bombard the Earth. The radiation environment in free space is very different from the one on the Earth's surface or that in low-Earth orbit, due to the much larger flux of high-energy galactic cosmic rays and the missing protection from the geomagnetic field.

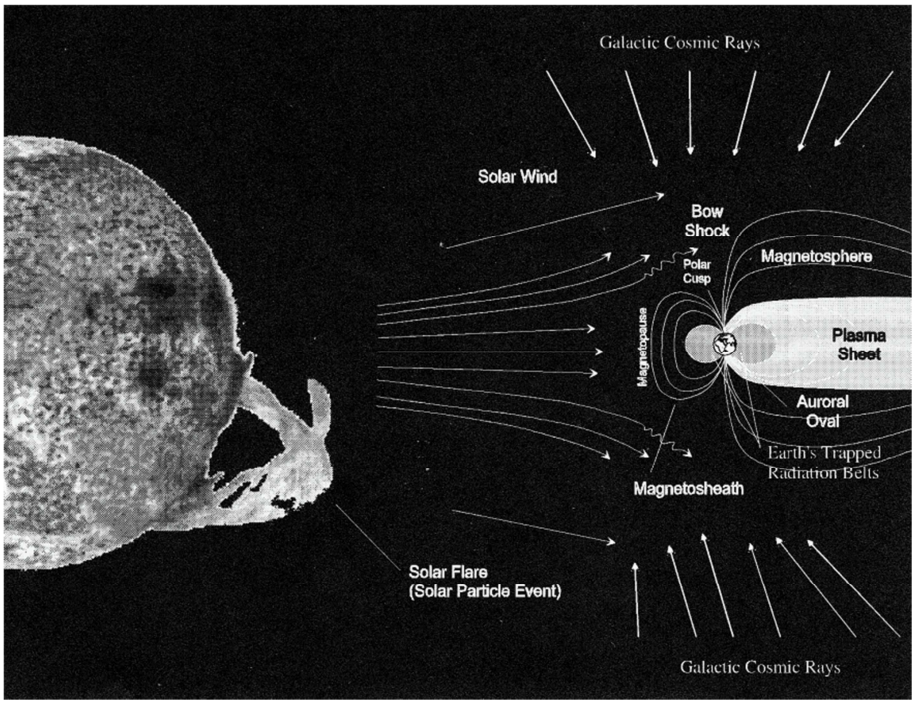

Figure 2-1: There are three principal sources of space radiation: galactic cosmic rays, trapped radiation in the Earth's radiation belts and solar particle events. All three sources are affected by the Earth's magnetic field. [3]

2.2.1 Galactic Cosmic Rays

Galactic cosmic rays are high-energy particles that enter our solar system from outside. The energy of these particles can be up to 10^{23}eV. [4] The flux of particles with highest energies is small (see Figure 2-2). The origin of this radiation is not entirely known. The different energies and the features in the energy spectrum suggest that miscellaneous stellar phenomena are responsible for the acceleration of galactic radiation. Basically, it is possible to define two models for cosmic-ray particles. The bottom-up model describe particles that start at low energies and increase their energy by acceleration. Representative origins for this acceleration could be events like the nuclear synthesis of stars, supernova explosions and pulses emitted by pulsars. Equivalently, the second scenario is the top-down model that describes particles that lose energy. A possible source is the decay of heavy particles in consequence of topological defects and relicts from phase transitions of the early universe. [5] In the bottom-up model, electromagnetic forces accelerate the particle. This acceleration can be direct, as a result of strong electromagnetic fields, or in a stochastic manner. The models for this stochastic acceleration are the first and the second order Fermi-acceleration. In the first model, a charged particle is scattered by magnetic fields and repeatedly traverses a shock front in the interstellar medium. Each time the particle crosses the field it absorbs energy. The second order Fermi-acceleration is less effective. A charged particle is scattered repeatedly at statistically

distributed magnetic clouds and gains energy in every cycle. The average energy gain ΔE is given as a function of the velocity of the particle v compared to the speed of light c by

First order Fermi acceleration : $$\frac{\Delta E}{E} \propto \beta \tag{2.1a}$$

Second order Fermi acceleration : $$\frac{\Delta E}{E} \propto \beta^2 \tag{2.1b}$$

$$\beta = \frac{v}{c} \tag{2.1c}$$

Magnetic fields of the Milky Way deflect charged particles of the galactic radiation. This model confines that cosmic rays with energies of less than 10^{18}eV are of galactic origin from the Milky Way and its halo. From the relative abundances of radioactive isotopes one can give an estimate of the elapsed time since nucleosynthesis or spallation. With this method, an estimate tends to result in an average age of cosmic radiation of about 10^7 years. [6] Further on, it allows to infer that cosmic rays have to traverse interstellar matter with an areal density of about 5.5 g/cm^2. [6] This leads to the supposition that cosmic rays stay mostly in the halo outside of the galactic disc.

Energy Spectrum

The galactic cosmic-ray flux reaches over several decades from several MeV to more than 10^{20}eV. The highest energies are much larger than any Earth-bound accelerator can currently provide, or in the near future. The galactic cosmic ray spectrum has its peak around 1 GeV. For high energies the spectra are represented by a power law:

$$\frac{dN}{dE} \sim E^{-\gamma} \tag{2.2}$$

$$\gamma \sim 2{,}5 \ldots\ldots E < 4.10^{15} eV$$

$$\gamma \sim 3 \ldots\ldots\ldots 4.10^{15} < E < 5.10^{18} eV$$

$$\gamma < 3 \ldots\ldots\ldots E > 5.10^{18} eV$$

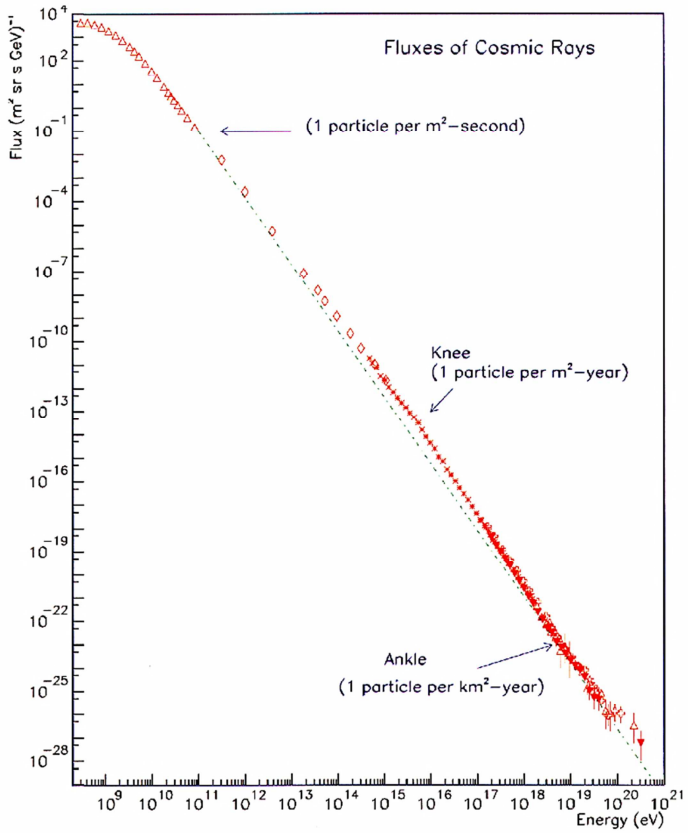

Figure 2-2: Spectrum of the galactic cosmic ray flux [7]

The change of the index γ at about 5.10^{15}eV, shown in Figure 2-2 is called the *knee*. The reasons for this effect are different acceleration and transportation through interstellar medium mechanisms for energies above and below the knee.

At energies above 10^{19}eV there is a flattening of the spectrum, the so-called *ankle*. It can be described by the *Greisen-Zatsepin-Kutz'min* cutoff. The cosmic microwave background reacts with high-energy photons above 5.10^{19}eV and causes the high-energy protons to loose energy by producing pions. [6]

$$\gamma + {}^{1}_{1}p \rightarrow {}_{+}\Delta \rightarrow {}^{1}_{1}p + {}_{0}\pi \qquad (2.3a)$$

$$\gamma + {}^{1}_{1}p \rightarrow {}_{+}\Delta \rightarrow {}^{1}_{0}n + {}_{+}\pi \qquad (2.3b)$$

This process affects all protons that are accelerated to higher speed and slows them down below the reaction threshold. Particles above the threshold energy are calculated to have a mean free path length of about $1.5 .10^{24}$m.

The incident direction of cosmic radiation is remarkably isotropic. Galactic magnetic fields deflect the cosmic rays and confine the particles in the galaxy and homogenize their incoming directions.

For example at energies up to 10^{15}eV, assuming an interplanetary field strength of 0.14 nT, the gyration radius of a cosmic ray is less than 3 $.10^{16}$ m, which corresponds to an anisotropy of less than 0.1%. [6] The influence of magnetic fields on galactic cosmic rays decreases with higher energies and its anisotropy increases simultaneously from around 1% at 10^{17}eV to a complete anisotropy of 100% above 10^{20}eV.

Elementary Composition

The elementary composition of galactic cosmic radiation comprises about 87% protons, 12% helium nuclei, 2% electrons and 1% heavier ions that have a nuclear charge between 3 and 92. Only a fraction of about 10^{-4} consists of photons and neutrinos. [6] The ions can be regarded as being distributed isotropically throughout interstellar space. The measured abundances of the elements relative to silicon compared with the solar system abundances are given in Figure 2-3.

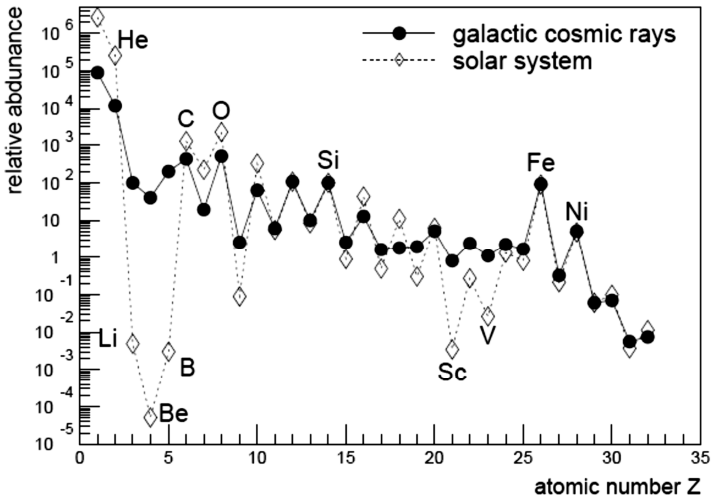

Figure 2-3: Nuclear abundances of the cosmic radiation with less than 2 GeV / nucleon compared to the composition of the solar system. Normalized to Si=100. [9]

The primary galactic rays interact with interstellar and interplanetary matter and with the interstellar and solar magnetic field. The spectrum depends on the modulation by the solar wind. Increasing solar activity causes a reinforcement of the interplanetary magnetic field that causes a stronger shielding of galactic cosmic rays. Hence, the intensity of cosmic radiation in proximity of the Earth is anti-correlated with solar activity. This effect affects mainly particles of energies below 10^{10}eV. [10] For higher energy particles these effects can be neglected.

2.2.2 Solar Cosmic Rays

Solar cosmic rays are continuously emitted by the sun and consist of electromagnetic radiation over virtually all wavelengths and a stream of charged particles, mainly protons and electrons as well as a few heavier nuclei. While the solar wind is a quasi-steady stream that varies on a timescale of days, there is another much more dramatic phenomenon, the solar particle events.

Solar Particle Events

Solar flares describe violent explosions in the sun's corona and chromosphere. These eruptions develop in minutes and have total energies up to 6. 10^{25} joules and emit up to 10^{10} particles per cm^2. [6] Flares occur usually in active regions around sunspots, where high magnetic fields emerge from the sun's surface into the corona. The flares consist of plasma with a temperature of several millions of Kelvin that accelerates charged particles up to energies of several GeV. The appearance of solar flares varies from several per day when there is high solar activity to a few per month when the solar activity is low. The solar activity varies with an eleven-year cycle, the so-called solar cycle (Figure 2-4). Large flares are significantly rare and occur typically about 1-3 times per cycle towards the end of a solar maximum. The main reason for the 11-year cycle of the sun is its dipole field. The intensity of the sun's dipole field oscillates in an 11-year-periode and changes direction every 22 years.

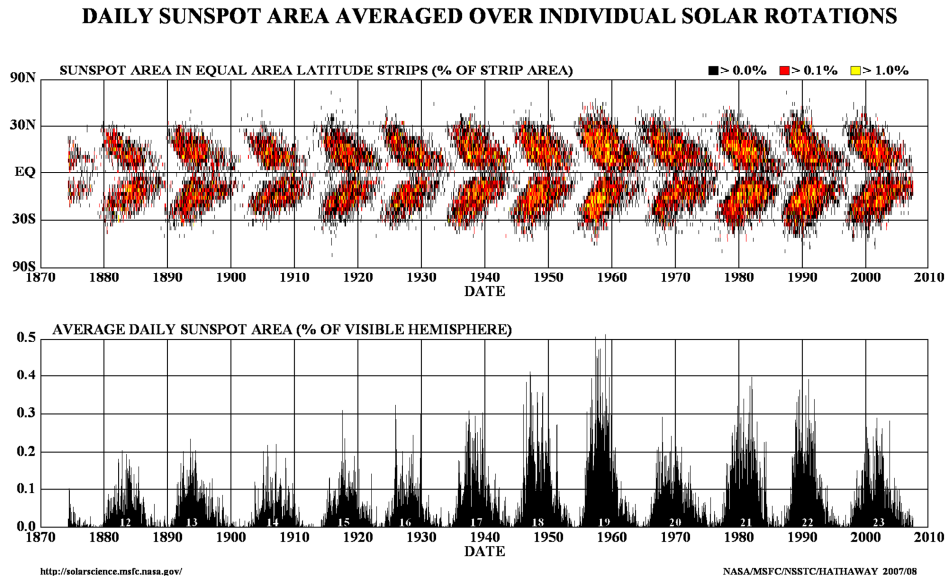

Figure 2-4: Sun spot number and solar activity in dependence on the 11- year solar cycle [12]

Solar Wind

The solar wind is a steady stream of charged particles that are emitted from the upper sun's atmosphere. This plasma consists mostly of electrons and protons with energies of about 1 keV. The solar wind streams off the sun in all directions at speeds of the order of 4. 10^5 m/s. The source of the solar wind is the sun's hot corona. The temperature of the corona is so high that the sun's gravity cannot hold onto it. Although we understand why this happens, we do not understand the details about how and where the coronal gases are accelerated to these high velocities. The solar wind is not constant, although it is generally directed away from the sun. Its speed is high (~ 8. 10^5 m/s) over coronal holes and low (~ 3. 10^5 m/s) over areas where high-speed wind catches up with slower wind and carries magnetic clouds and composition variations with it. These so-called streams interact with each other and pass the Earth alternately as the sun rotates. The interaction of the streams with the Earth's magnetic field causes storms in the Earth's magnetosphere.

2.2.3 Earth's Trapped Radiation Belts

The Earth's trapped radiation belts (ERBs)[1] consist of an inner and an outer torus surrounding it by intense regions of energetic charged particles. The Earth's geomagnetic field holds this plasma in place where it follows a complex motion. The inner belt extends 700 - 10,000 km above the Earth's surface is dominated by protons with energies > 10 MeV. A second zone is dominated by electrons and extends from about 15,000 - 65,000 km with maximum energies of around 7 MeV. The Van Allen belt radiation is obvious outside of the atmosphere and usually does not reach the Earth's surface, but due to the dipole-shape of the magnetic field particles of the ERBs can strike the upper atmosphere and fluoresce at Polar regions and are therefore closely related to the polar aurora.

2.3 Earth's Magnetic Field

The Earth's magnetic field is approximately a magnetic dipole. With an appropriate selection of its point of origin, this approximation can describe the field on the surface with an accuracy of 90%. The magnetic field (magnetic flux density/magnetic induction) *B* can be estimated by the dipole-formula in dependence on the distance (*R*) and the geomagnetic latitude (λ).

$$B(R,\lambda) = \frac{M}{R^3}\sqrt{1+3.\sin^2(\lambda)} \tag{2.4}$$

[1] The inner radiation belt was discovered by James A. Van Allen. Hence, the inner belt is also called Van Allen belt.

With an estimated magnetic dipole moment M = 7.812. 10^{24} nT.m³ [13] the magnetic field has a strength of about 30 µT at the equator and about 60 µT at the pole regions.

The Earth's magnetic field is not constant and it changes very slowly on a timescale of millennia in unsteady rates that can even lead to magnetic pole reversal. In 2008, the magnetic North Pole was located in North of Canada in a distance of 1800 km from the geographic North Pole. There is the same proximity between the magnetic and geographic South Pole. The magnetic axis is inclined by approximately 11.3° to the Earth's axis of rotation.

The origin of the magnetic field can be explained by the dynamo theory. The magnetic field is caused by the convection of molten iron within the outer liquid core, along with the Corriolis effect caused by the planetary rotation. Electric currents are induced, when conducting fluid flows across an existing magnetic field. These currents create another magnetic field that reinforces the original magnetic field. A dynamo is created, which sustains itself. Similar fields are seen on some other rotational celestial bodies that have properties of conductive matter. At the sun, conducting plasma causes the magnetic field that is on the surface about twice as strong as the Earth's field.

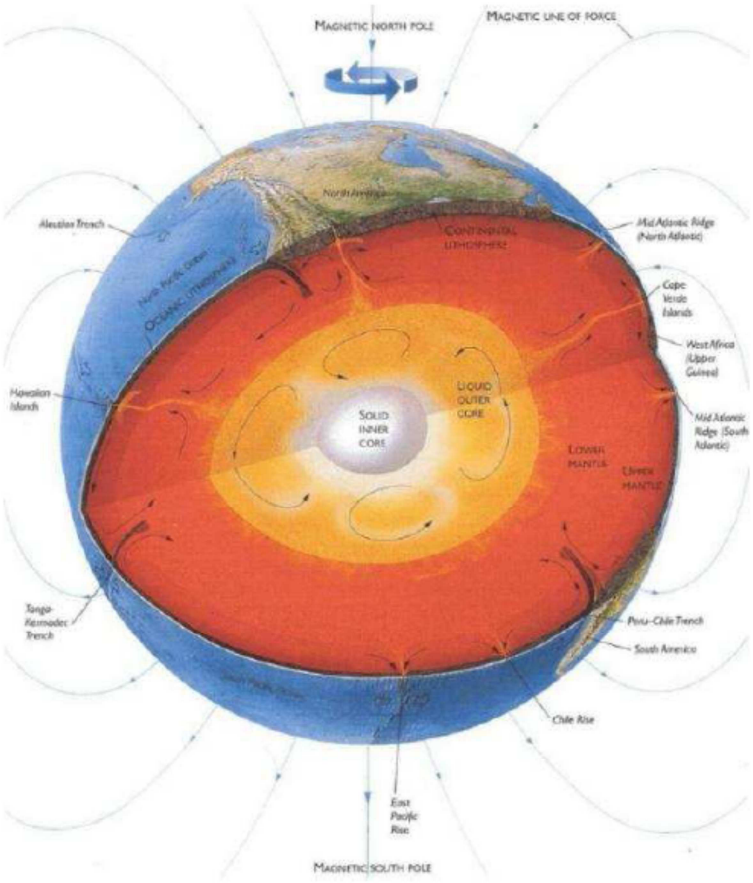

Figure 2-5: Architecture of the Earth and the Earth's magnetic field [14]

The magnetosphere of the Earth is defined as the region in space whose shape is determined by the extent of the Earth's magnetic field, the solar wind plasma, and the interplanetary magnetic field (see Figure 2-1). Magnetic fields extend infinitely, though they are weaker further from their source. The region where the Earth's magnetic field has an effective influence on charged particles extends several tens of thousands of kilometers into space. The magnetic field deflects the charged particles of the solar wind. Therefore, the field has a strong deformation at high altitudes. Magnetic storms caused by solar flares and the solar wind can temporarily change the field strength from several hundred to thousand Nano-Tesla in the Earth's ionosphere.

A cosmic ray has to penetrate the magnetic field to enter the atmosphere. The quantity of its penetrating ability is called the magnetic rigidity which is the cosmic ray's momentum divided by its charge. Due to the dipole shape of the field, the dose rate depends on the geomagnetic latitude. At the same altitude, the dose rate is higher in polar areas. Only high-energy charged particles are able to cross the magnetic barrier and can proceed into the atmosphere.

Geomagnetic Cutoff Rigidity

"Geomagnetic rigidity is the minimum energy a primary proton must have to create a cascade which can reach sea level at that location. The shielding effect of the Earth's magnetic field is usually described by the concept of cutoff rigidities since the magnetosphere imposes a lower limit on the energy of primary cosmic ray particles to enter the atmosphere. The unit of rigidity is volts or as in the figure, GV (giga-volts). The higher the rigidity, the lower the probability that primary particles will hit the atmosphere in order to produce secondary particles at a specific location." [17]

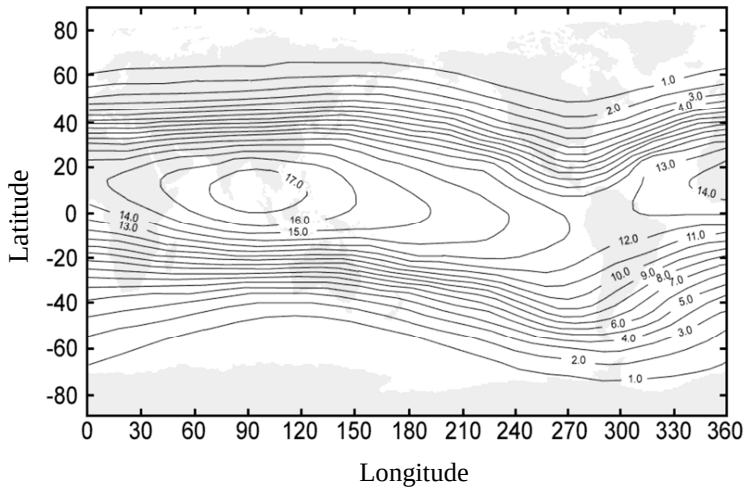

Figure 2-6: Global geomagnetic cutoff rigidity in GV (Epoch 2000) [18]

South Atlantic Anomaly

"The South Atlantic Anomaly (or SAA) is the region where the Earth's inner Van Allen radiation belt makes its closest approach to the planet's surface. Thus, for a given altitude, the radiation intensity is greater within this region than elsewhere. The Van Allen radiation belts are symmetric with the Earth's magnetic axis, which is tilted with respect to the Earth's rotational axis by an angle of ~11 degrees. Additionally, the magnetic axis is offset from the rotational axis by ~450 kilometres. Because of the tilt and offset, the inner Van Allen belt is closest to the Earth's surface over the South Atlantic Ocean and farthest from the Earth's surface over the North Pacific Ocean." [15]

2.4 Radiation Environment in the Earth's Atmosphere

The radiation environment in the stratosphere is the result of the interaction between charged particles of solar and galactic origin and the Earth's magneto- and atmosphere. The composition and the intensity change with geomagnetic latitude, solar activity and especially with altitude. With increasing penetration depth, the primary radiation is more absorbed and decreases while the secondary radiation increases. This complex situation results in a maximum of the dose rate at an altitude of approximately 12-20 km above main sea level, which is called the *Pfotzer Maximum*. [16] Figure 2-7 shows dose equivalent rates of secondary cosmic ray and its components as a function of altitude.

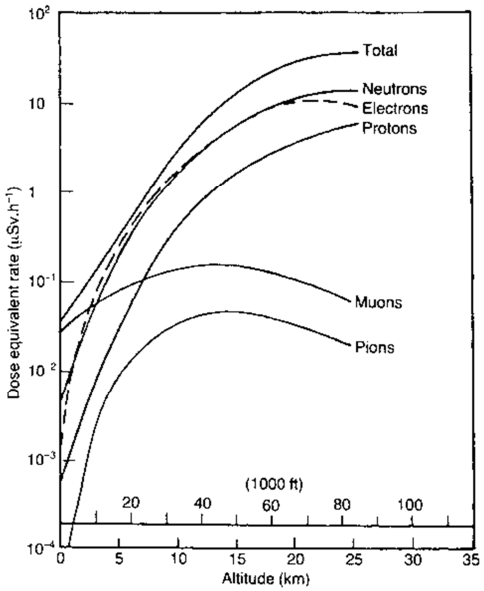

Figure 2-7: Secondary cosmic ray dose equivalent rates calculated as a function of altitude for different particles at 55° geomagnetic latitude during solar minimum conditions [19]

2.4.1 Interaction with the Atmosphere

When cosmic-ray particles enter the atmosphere, they collide with molecules to produce a cascade of secondary particles. The primary nuclei in the upper atmosphere lose most of their energy by ionization of the atmosphere's molecules and nuclear reactions that cause a shower of high-energy nuclei or fragments. At high energies, the main processes occur with oxygen and nitrogen, such as the typical collisions:

$$ {}^{1}_{1}p + {}^{16}_{8}O \rightarrow {}^{1}_{0}n + {}^{16}_{9}F + {}_{o}\pi \qquad (2.5a) $$

$$ {}^{1}_{0}n + {}^{14}_{7}N \rightarrow {}^{1}_{1}p + {}^{14}_{6}C \qquad (2.5b) $$

The heavier particles have a larger cross section in the atmosphere and at a penetration depth where the proton flux is half of the primary flux, the alpha particle flux has been reduced to a quarter and the heavy ion flux to less than 3% of its original strength. [6] Hence, at deep regions protons play the major role in production of secondary particles.

The target nuclei of the atmosphere are highly excited and release some additional nucleons to end up as either stable or radioactive nuclei. The total intensity is rather constant between 150,000 m and 50,000 m. Below this altitude the intensity increases further until it reaches its maximum at about 20,000 m, the so-called Pfotzer maximum.

A single proton with energy of about 10^{15}eV creates more than a million secondary particles with a single interaction of an atmospheric nucleus. [6] Only a small quantity of these secondary particles reaches the Earth's surface. All of the produced particles stay within a very small angle of the primary particle's path.

Generally, the particle production can be divided into three categories, the hadron, the muon and the electron-photon component (Figure 2-8). An additional component consists of neutrinos, uncharged leptons with extremely small interaction capability. They can be further ignored, because they do not produce secondary particles and pass through ordinary matter almost undisturbed. Therefore, they have effectively no impact on further considerations.

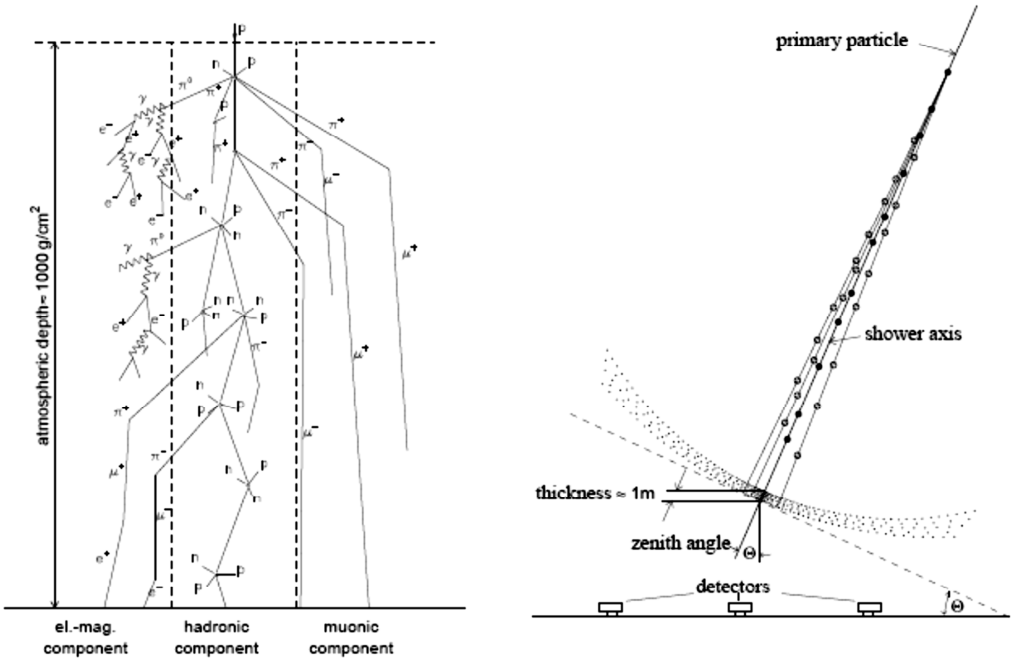

Figure 2-8: Schematic representation of the particle production in the atmosphere [20]

2.4.2 Hadronic Component

The hadronic component consists of strongly interacting particles. By spallation of nitrogen and oxygen atoms neutrons ${}^1_0n$, protons ${}^1_1p$, charged (${}_+\pi, {}_-\pi$) and neutral (${}_0\pi$) pions are generated. In these processes, pions are the most common kind of particles.

$${}^1_1p + {}^1_1p \rightarrow {}^1_1p + {}^1_0n + {}_+\pi \quad (2.6a)$$

$${}^1_1p + {}^1_0n \rightarrow {}^1_1p + {}^1_1p + {}_-\pi \quad (2.6b)$$

$${}^1_1p + {}^1_1p \rightarrow {}^1_1p + {}^1_0n + {}_+K \quad (2.6c)$$

The mean lifetime of a pion is 2.6033(5). 10^{-8} s [21] and it decays into electromagnetic and muonic components (see Chapter 2.4.3 and Chapter 2.4.4).

When the energy drops below the minimum energy to produce pions, protons lose energy through ionization until they decay. At energies above 100 GeV pions can interact before they decay and therefore contribute to the increase of secondary particles.

A typical example of follow-up interaction is the production of kaons ${}_+K$ (and hyperons Λ) by pion-neutron reactions.

$${}_+\pi + {}^1_0n \rightarrow {}_+K + \Lambda \quad (2.7)$$

2.4.3 Electron-Photon Component

The electron-photon component consists of electrons ${}_{-}e$, positrons ${}_{+}e$ and photons γ. The major fraction is generated by the fast decay of neutral pions (${}_{0}\pi$) after a mean lifetime of about 10^{-16} s. [21]

$${}_{0}\pi \rightarrow \gamma + \gamma \tag{2.8}$$

The cascade starts electrically neutral but by acceleration of atmospheric electrons through Compton recoil and electron-positron annihilation, it develops a negative charge excess. The highly energetic particles produce electromagnetic cascades in which pair production (2.9a), annihilation (2.9b) and bremsstrahlung (2.9c) occurs.

$$\gamma \xrightarrow{E_{\gamma}>2x511keV} {}_{-}e + {}_{+}e \tag{2.9a}$$

$${}_{-}e + {}_{+}e \rightarrow \gamma \tag{2.9b}$$

$$e(E + \Delta E) \rightarrow e(E) + \gamma(\Delta E = h.\nu) \tag{2.9c}$$

Once the energy of the electrons/positrons drops below the critical energy ($E_{crit,air}$ = 84.2 MeV) they lose, on average, more energy by ionisation than by bremsstrahlung. Then they do not produce new γ-quanta and the electromagnetic cascade dies out. [22]

2.4.4 Muonic Component

The muons (μ) in an air shower are mainly produced by the decay of charged pions (${}_{+}\pi$, ${}_{-}\pi$). Their mean lifetime is about 2.2µs. [21] Despite this short lifetime most muons reach the Earth's surface because the range of the muons is extended by relativistic time dilatation. At sea level the rate of high-energy cosmic muons is ~1 muon/cm^2 min. [23] The lateral distribution of the muons depends on the angular distribution.

Chapter 3

Radiation Dosimetry and Effects

3.1 Dose Quantities

For development of dosimetric concepts, a common standard of dose quantities has been established that allows a precise physical description of the radiation field and the energy deposition as well as a useful presentation of the involved risks for biological organisms. The ICRP (International Commission on Radiological Protection) and the ICRU (International Commission on Radiation Units and Measurements) have developed a hierarchy of quantities for radiation protection applications, which can be classified into *basic physical quantities*, *limiting quantities* (also termed *protection quantities*) and *operational quantities*.

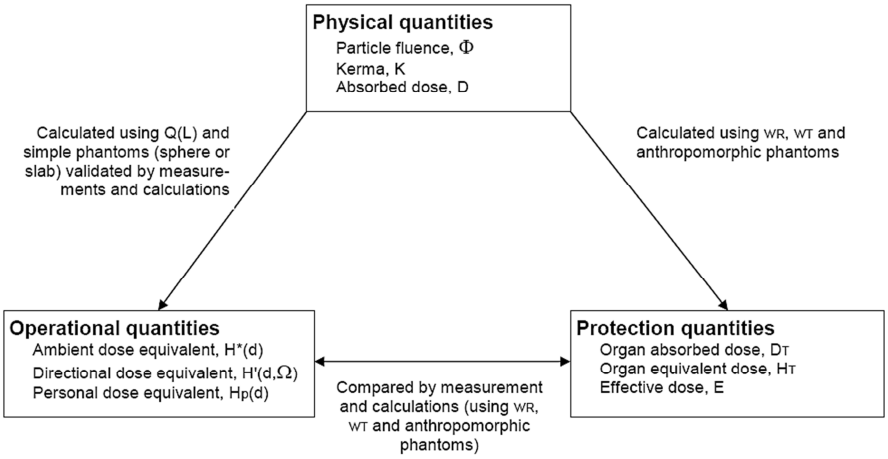

Figure 3-1: Relationship between the basic physical quantities, the operational quantities and the protection quantities [31]

3.1.1 Basic Physical Quantities

Particle Flux

The *(particle) flux*, $\dot{N}$ is the quotient of *dN* by *dt*, where *dN* is the particle number in the time interval *dt*.

$$\dot{N} = \frac{dN}{dt} \tag{3.1}$$

The particle flux is measured in s^{-1}.

Particle Fluence

The *(particle) fluence* Φ is the quotient of *dN* by *da*, where *dN* is the number of particles incident on a sphere of cross-sectional area *da*. [26]

$$\Phi = \frac{dN}{da} \tag{3.2}$$

The respective unit is m^{-2}.

Absorbed Dose

The basic physical quantity in dosimetry is the *absorbed dose D*. It is defined as the mean energy imparted by ionizing radiation to matter divided by its mass

$$D = \frac{d\bar{\varepsilon}}{dm} \tag{3.3}$$

where $d\bar{\varepsilon}$ is the mean energy imparted by ionizing radiation to matter of mass d*m*. [26]

The unit name of the absorbed dose is the *Gray [Gy]*, named after the British physicist Louis Harold Gray. One Gray is the absorption of one joule of radiation energy by one kilogram of matter. The outdated unit name *rad [rad]* is still prevalent as well.

$$1\ \ Gy = 1\ \ \frac{J}{kg} = 100\ \ \ rad \tag{3.4}$$

Dose Rate

The dose rate is the amount of ionizing radiation that an individual or material receives per unit time. Typical units are Gray or rad per hour or submultiples of these units.

$$\dot{D} = \frac{dD}{dt} \tag{3.5}$$

Kerma

Kerma is an abbreviation of *kinetic energy released per unit mass* or *kinetic energy released in matter*. The kerma is the quotient of dE_{tr} by dm, where dE_{tr} is the sum of the kinetic energies of all charged particles liberated by uncharged particles (indirectly ionizing particles) in a material of mass dm. [26]

$$K = \frac{dE_{tr}}{dm} \tag{3.6}$$

The unit of kerma is Gray (Gy) respectively Joule per kilogram.

In case of charged particle equilibrium (*CPE*), kerma is approximately equal to the absorbed dose at low energies (< 300 keV [32]). At higher energies, kerma is higher than absorbed dose, as some of the energy escapes (E_{esc}) from the absorbing volume in the form of bremsstrahlung, X-rays or fast moving electrons.

$$K = D - E_{esc} \Big|_{CPE} \tag{3.7}$$

Ionization Density and Linear Energy Transfer Factor

Charged particles ionize the matter along their track. Dependent on the energy and type of particle, the distribution of ionization events in the target matter is more or less closely spaced. This effect causes a different ionization density, which can be characterized by the *linear energy transfer (LET)*. It is the locally absorbed energy dE per unit distance dx.

$$L_{\infty} = \frac{dE}{dx} \tag{3.8}$$

The locally absorbed energy is defined by means of the energy distribution in the proximity of the projectile track. To define “local” area it is common to set an upper energy limit. Often this limit is set to an energy of 100 eV. If a limit is set, this cut-off is typically written as index in the formula.

$$L_{\Delta E} = \left(\frac{dE}{dx} \right)_{\Delta E} \tag{3.9}$$

The definition of the unrestricted LET is achieved by the limes $\Delta E \rightarrow \infty$.

It is significant that the biological effectiveness of radiation depends on the ionization density. At the same level of absorbed dose radiation with high LET, which describes dense ionization, has a higher biological effectiveness.

3.1.2 Limiting Quantities

“The basic idea of a *primary limiting quantity* is to relate the “risk” of exposure to ionizing radiation (by internal and external radiation sources) to a single (dose) quantity, which takes account of the

human as a receptor, the different radiation sensitivities of various organs and tissues and the different radiation qualities." [34] The radiation protection quantities published by the ICRP are often taken into account to establish compulsory limitation of radiation exposure. These units judge the risk due to radiation exposure but are not directly measurable.

Dose Equivalent and Quality Factor

The *dose equivalent H* is a measure of the biological damage to living tissue as a result of ionizing radiation. It is defined as the product of the *absorbed dose D* multiplied by a *quality factor Q* at a point in tissue.

$$H = D.Q \tag{3.10}$$

The *quality factor Q* accounts for the relative biological effectiveness of radiation. It is based on biological research and mainly depends on the ionization density of the radiation. The quality factor function *Q(L)* is given by the equation

$$Q(L) \begin{cases} = 1 & L < 10 keV/\mu m \\ = 0.32L - 22 & 10 \le L \le 100 keV/\mu m \\ = \dfrac{300}{\sqrt{L}} & L > 100 keV/\mu m \end{cases} \tag{3.11}$$

Tissue or Organ Absorbed Dose

The tissue or organ absorbed dose D_T is the quotient of the total energy imparted on a tissue or organ and the mass of that tissue or organ. [26]

Equivalent dose in an Organ or Tissue

Different kinds of radiation have different effects on biological tissue. The equivalent dose is a measure of the radiation dose with respect to the biological effects of different types of radiation. Hence, the dimensionless radiation weighting-factor w_R is defined, characterizing the biological effectiveness of a specific radiation *R* relative to photons (Table 3-1). In radiation fields that contain various energies and radiation types with different weighting-factors, these factors are additive.

$$H_T = \sum_R w_R D_{T,R} \tag{3.12}$$

Table 3-1: Values of radiation weighting factors, w_R [33][34]

Type and energy range		Radiation weighting factor, w_R	
		ICRP 60	ICRP 103
Photons, all energies		1	1
Electrons and muons, all energies		1	1
Neutrons, energy	< 10 keV	5	Proposed w_R function shown in Figure 3-2
	10 keV to 100 keV	10	
	> 100 keV to 2 MeV	20	
	> 2 MeV to 20 MeV	10	
	> 20 MeV	5	
Protons, other than recoil protons, energy > 2 MeV		5	2
Alpha particles, fission fragments, heavy nuclei		20	20

The w_R values for various types of radiation are specified in ICRP 60 [33] and in ICRP 103 [34]. For photons, electrons[2] and muons of all energies a value of one is fixed. The radiation weighting factor for neutrons depends on the neutron energy. Different w_R values are given by a step function (ICRP 60) or a continuous function (ICRP 103, Figure 3-2). In practice, neutron fields mostly contain neutrons with a broad energy distribution. The use of a continuous w_R-function for equivalent and effective dose estimation is much more appropriate.

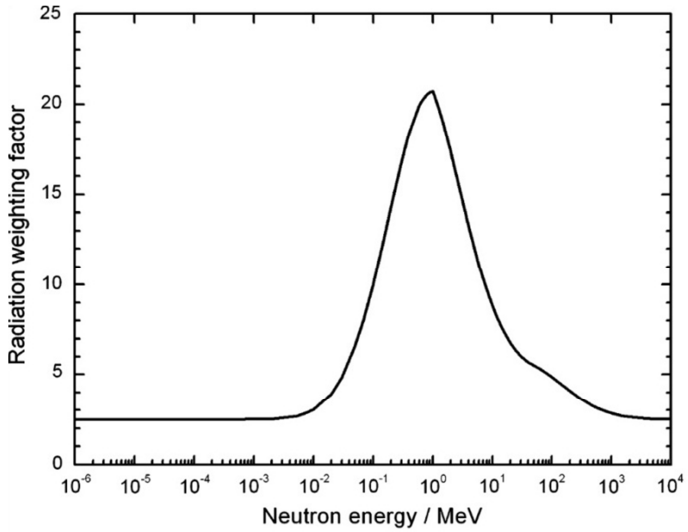

Figure 3-2: Radiation weighting factors w_R for neutron radiation. (ICRP 103) [34]

[2] with the exception of Auger electrons emitted from nuclei bound to DNA

The unit name of the equivalent dose, *Sievert [Sv]*, is named after the Swedish medical physicist *Rolf Maximilian Sievert*. Alternatively, the outdated unit name *rem [rem]*, is still frequently used.

$$1 \quad Sv = 1 \quad \frac{J}{kg} = 100 \quad rem \tag{3.13}$$

Effective Dose

To differentiate the miscellaneous sensitivities of organs and tissues the equivalent dose has to be multiplied by a tissue weighting factor w_T. This leads to the effective dose E. It is a relevant measure for the biological risk of radiation and provides a basis for the definition of whole-body dose limits.

$$E = \sum_T w_T H_T = \sum_T w_T \sum_R w_R D_{T,R} \tag{3.14a}$$

$$\sum_T w_T = 1 \tag{3.14b}$$

The effective dose is the weighted sum of organ equivalent doses.

The tissue weighting factors w_T characterize the relative sensitivity of the various tissue and organs with respect to cancer induction and mortality. Twelve (ICRP 60) respectively fourteen (ICRP 103) tissues and organs are specified with individual tissue weighting factors and supplemental tissue weighting factors are defined for the remainder.

Table 3-2: Values of tissue weighting factors, w_T [33][34]

Tissue or organ	Tissue weighting factors, w_T	
	ICRP60	ICRP103
Gonads	0.20	0.08
Bone marrow (red)	0.12	0.12
Colon	0.12	0.12
Lung	0.12	0.12
Stomach	0.12	0.12
Bladder	0.05	0.04
Breast	0.05	0.12
Liver	0.05	0.04
Oesophagus	0.05	0.04
Thyroid	0.05	0.04
Skin	0.01	0.01
Bone surface	0.01	0.01
Brain		0.01
Salivary glands		0.01
Remainder	0.05	0.12
Total human organism	**1.00**	**1.00**

3.1.3 Operational Quantities

Operational quantities are dose quantities defined for use in radiation protection measurements of external exposure (area or individual monitoring). They usually should provide an estimate of or an upper limit for the value of the limiting quantities due to an exposed, or potentially exposed person. Operational quantities are needed for monitoring external exposures because protection quantities generally are not measurable.

Concept of Operational Quantities

The present definitions are given in the ICRU Report 51. [29] The radiation incident on a human body is characterized as *penetrating radiation* or *low-penetrating radiation*, depending on the ratio of the skin dose to effective dose. Radiation is considered as low-penetrating, when the dose equivalent received by the skin (dose received at a depth of 0.07mm) in the case of normal incidence of an expanded radiation field is higher than ten times the effective dose – otherwise it is considered to be penetrating (dose received at a depth of 10 mm). Low penetrating radiations are α-particles, β-particles with energies below 2 MeV and photons with energies below 12 keV. Neutrons always are penetrating radiation. [30]

Ambient Dose Equivalent H*(d)

The operational quantity for area monitoring of ionizing radiation is the ambient dose equivalent H*(d). It describes the dose equivalent that would be produced by the corresponding aligned and expanded radiation field in the ICRU sphere of standard soft tissue (see below) at a depth *d*, on the radius opposing the direction of the aligned field. An oriented and expanded radiation field is an idealized radiation field which is expanded and in which the radiation is additionally oriented in one direction. The unit name of ambient dose equivalent is *Sievert (Sv).*

Radiation that is considered as penetrating radiation is usually estimated by H*(10) corresponding to the dose equivalent received at a depth of 10 mm, and for low-penetrating radiation it is recommended to use H*(0.07) equating to a dose received at a depth of 0.07 mm.

The ICRU Sphere

For all types of radiation the operational quantities for area monitoring are defined on the basis of a phantom, termed the ICRU sphere. The standard ICRU sphere has a 30 cm radius, a density of 1 g/cm^3 and it equates to a composition of a standardized soft tissue that contains 76.2wt% oxygen, 11.1wt% carbon, 10.1wt% hydrogen, 2.6 wt % nitrogen. [27][28] It adequately approximates the human body as regards the scattering and attenuation of the radiation fields under consideration.

Aligned and Expanded Radiation Field

An expanded field is a radiation field, in which the spectral and angular fluence have the same values in all points of a sufficiently large volume. It ensures that the whole ICRU sphere is exposed to a homogeneous radiation field with the same fluence, energy distribution and directional distribution as in the point of interest of the real radiation field. If all radiation is aligned in the expanded radiation field so that it is opposed to a radius vector specified for the ICRU sphere, the aligned and expanded radiation field is obtained (Figure 3-3). In that case, the value of the dose equivalent at any point in the ICRU sphere is independent on the directional distribution of the real radiation field. [29][30]

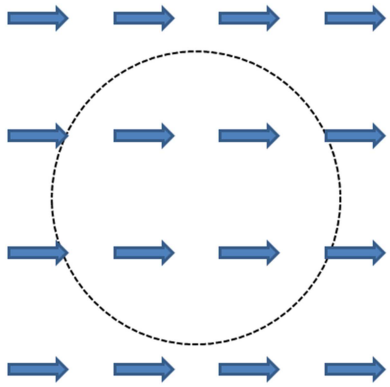

Figure 3-3: Schematic representation of an aligned and expanded radiation field.

Directional Dose Equivalent H'(d,Ω)

The directional dose equivalent H'(d,Ω) is the dose equivalent that would be produced by the expanded radiation, in the ICRU sphere at a depth d, on a radius in a specified direction Ω. [1] [26]

Operational Quantities for Individual Monitoring $H_p(d)$

"For individual monitoring the operational quantity is the personal dose equivalent, $H_p(d)$. The personal dose equivalent $H_p(d)$, is the dose equivalent in ICRU tissue at a depth d in a human body below the position where an individual dosemeter is worn. For monitoring of the skin dose d = 0.07 mm is recommended and for monitoring of the effective dose d = 10 mm, The operational quantities for individual monitoring meet several criteria. They are equally defined for all types of radiation, additive with respect to various directions of radiation incidence, take into account the backscattering from the body and can be approximately measured with a dosemeter on the body. The personal dose equivalent quantities, $H_p(10)$ and $H_p(0.07)$, are defined in the person, in the actually existing radiation field, and are measured directly on the person." [34]

Operational Dose Measurement in Aviation

The reliability of operational measurements varies for radiation with different energies and LET-values. The radiation field on board of an airplane in ~10 km differs from the radiation field on the Earth's surface. Measurements at civil aircraft show that the maximum of the dose equivalent does not occur at a depth of 10 mm but at a depth of 50 mm to 60 mm in a phantom-body of matter equivalent to human tissue (Figure 3-4). Hence, H*(10) provides a less accurate estimate of received radiation at high-energy radiation fields of the atmosphere at flight altitudes.

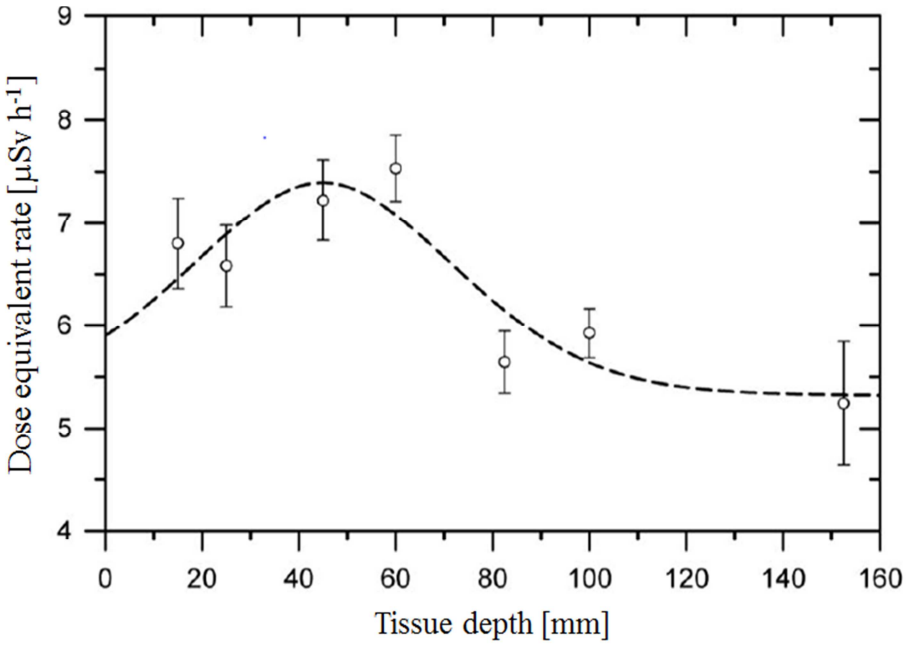

Figure 3-4: Dose equivalent rate in tissue due to cosmic radiation at flight altitudes [35]

Therefore, the *Regional Congress on Radiation Protection in Central Europe (IRPA)* passed a resolution in 2003 that recommends an adaptation of the current dosimetric quantities to the special situation of aircrew monitoring. The relation of the effective dose to the ambient dose equivalent may be calculated by the Monte Carlo code FLUKA [36] as function of altitude for different values of the vertical geomagnetic cut-off (Figure 3-5).

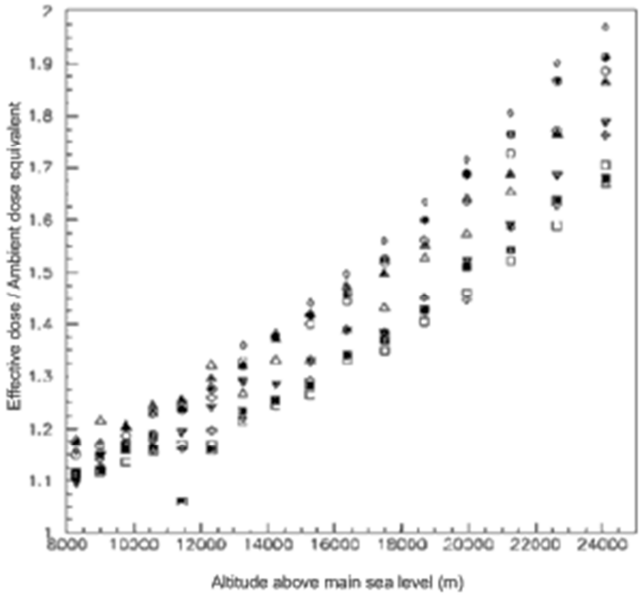

Figure 3-5: Relation of effective dose to ambient dose equivalent over altitude [37]

3.2 Biological Effects of Ionizing Radiation

The initial effect of ionizing radiation on a living organism begins with absorption of energy from radiation, which causes atoms and molecules to become ionized or excited. The excitations and ionizations of atoms and molecules can generate a cascade of effects that are able to change cell structures affecting the functioning of an organism. A qualitative description of the impact of ionizing radiation classifies a possible effect in three phases, the physical phase, where the radiation is absorbed, the chemical phase, where intra- and intermolecular energy transfer occurs, and the biological phase, where biochemical variances lead to damages of the organism. (Figure 3-6)

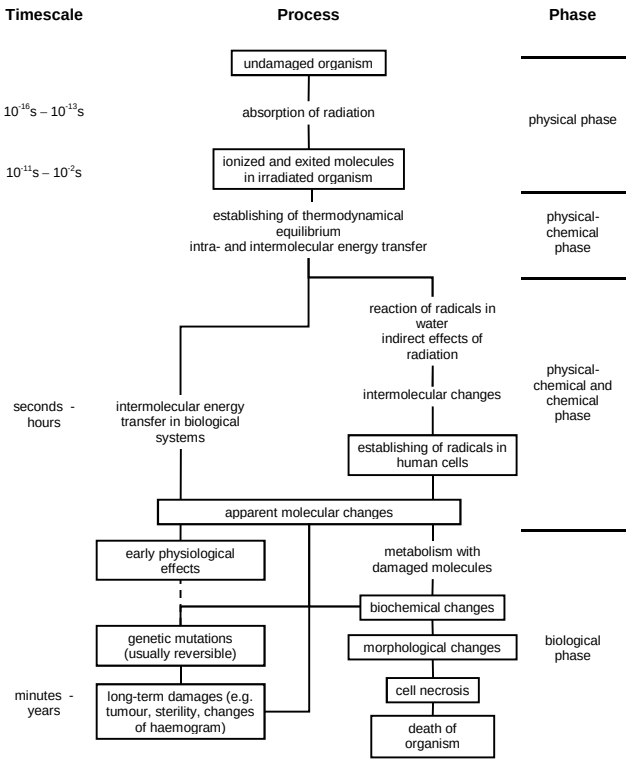

Figure 3-6: Time flow and possible impacts of ionizing radiation on human organisms [38]

Direct and Indirect Action of Ionizing Radiation

Cells exposed to ionizing radiation can receive radiochemical damage either by *direct action* or *indirect action*. Direct action means that the energy absorption and the damage happen in the same biological molecule. Indirect action means that the damage occurs in a different structure than the energy absorption. In the absorbing structure chemically reactive products are generated and diffuse to neighbouring molecules.

Molecular Effects of Radiation

The radiation effects mainly depend on the *radiation chemistry of water*, which has a major role for biological substances due to the high water concentration in biological material. [38] Basically, radiation can lead to a decomposition of water molecules and induce free electrons, free radicals and secondary radiation.

Further, the oxygen concentration in biological tissue has a large impact on radiation effects. The *oxygen effect* causes both, an increase (sensitisation) as well as a weakening (protective function) of the radiation effects. [38] The protective function happens mainly in aqueous solutions where

oxygen is a radical interceptor. In dry substances oxygen abundance creates additional free radicals and increases the damage to the target tissue. The quantitative sensitisation is described by the oxygen enrichment ratio (OER) that depends amongst others on the LET of the radiation.

The generated free radicals can cause various effects in the irradiated organism. Especially, the radicals[3], $H^{\bullet}$ and $OH^{\bullet}$, have a high chemical responsiveness and have therefore a high impact on biomolecules by changing their structure. The so produced biological radicals can subsequently react with further molecules and lead to irreversible damage by intermolecular rearrangement. These changes of the molecular structure and the accumulation of free radicals can further affect complex organic molecules that regulate vital cell processes, like deoxyribonucleic acid (DNA), ribonucleic acid (RNA), proteins and cell membranes.

The impact on the DNA is often seen as a basic process of radiation action. The change or breakdown of just one base within the DNA can have a biological effect, if it contains important unique information. DNA and RNA are mainly damaged by direct action, because they are shielded against indirect action by histones. These special proteins are very closely bound to the acids and protect them by their ability to catch free radicals. Damage of DNA can occur by a single stand break, a double strand break or a base change. Due to the double helix shape of the DNA, a double strand break happens only if both strands are destroyed within a few nucleotides[4]. The probability that this happens is significantly lower than the probability of a single strand break. For the splitting of one strand an energy of about 15 to 20 eV is necessary, while for a double strand break a minimum energy of about 100 eV to 200 eV is required. [38] This is of special importance due to the fact that a single strand break can be repaired with a significantly higher probability than a double strand break. [38]

Gene Mutation

If damage occurs in cells, it can lead to changes of protein synthesis and therefore a distortion of the cells' function. "A gene mutation is a permanent change in the DNA sequence that makes up a gene. Mutations range in size from a single DNA building block (DNA base) to a large segment of a chromosome." [40] Gene mutations are distinguished between hereditary mutations that can be inherited over generations or somatic mutations that are acquired during a person's lifetime. "Mutations that are passed from parent to child are called hereditary mutations or germline mutations. This type of mutation is present throughout a person's life in virtually every cell in the body." [40] "Somatic mutations can occur in any of the cells of the body except the germ cells

[3] A radical is marked with a point in the upper right corner (e.g. $R^{\bullet}$).

[4] Nucleotides are molecules that build the structural units of DNA and RNA.

(sperm and egg) and therefore are not passed on to children. These alterations can (but do not always) cause cancer or other diseases.” [41]

Cell Repair Mechanism

DNA damage is to a large extent caused by radicals that are created in the mitochondria of the cells. Some DNA damage can be repaired by the cell itself. Upon destruction of a base, the resulting gap in DNA is filled by copying the undamaged strands in order to reconstruct the correct genetic information. However, if during the repair process an additional damage occurs on the opposite strand (double-strand break), this damage can only be repaired with much lower probability. [38]

Some important effects that influence the cell repair mechanism are

- The LET of received radiation: The repair ability is higher for lower LET values
- The distribution of a specific dose: Generally, the exposure to several small doses has a considerably lower biological effect than the same total exposure applied at once.
- The phase of the life-cycle of a cell: Various phases have different sensitivities to radiation exposure. The cell is especially vulnerable during the mitosis (the phase of the cell division).

3.2.1 Deterministic and Stochastic Effects on Human Organisms

Cell destruction through radiation can lead to severe damage to human organisms. Especially broken enzymes can lead to biological deterioration because of their regulating effect for the metabolism. Essential for the degree of damage is the structure and composition of the involved proteins. Cell mutation can lead to evolutional physiological damage and to cancer, if the mutated cells are able to reproduce themselves by mitosis. The biological effects of radiation are generally divided into two categories, deterministic and stochastic effects.

Deterministic Radiation Effects

A deterministic radiation effect can be defined, as follows: “Effect of ionizing radiation leading to a functional loss of the irradiated organ or tissue, if sufficient cells are killed or prevented from reproducing or functioning due to radiation. The seriousness of this loss of tissue/organ function is directly proportional to the number of cells affected. Since the function of many organs and tissue is not impaired by a limited reduction in the number of functional cells, a threshold dose for deterministic radiation effects exists, which must be exceeded for an effect to occur. In the case of radiation doses above this threshold the degree of pathological severity increases rapidly [with dose (Figure 3-7)].” [42]

Typical examples for deterministic effects of ionizing radiation are skin reddening, opacity of the eye lens, permanent sterility and radiation sickness. The occurrence of deterministic effects depends on thresholds doses that must be exceeded. Based on the limiting quantities (see Chapter 3.1.2), annual and life-time dose limits can be defined, to prevent the occurrence of deterministic radiation effects. The values shown in Table 3-3 are based on a large number of experiments and researches, further supplemented by theoretical studies.

Table 3-3: Threshold for deterministic effects [39]

Threshold for deterministic effects			
	Effects	One single absorption [Gy]	Prolonged absorption [Gy/year]
Testis	Permanent infertility	3.5 - 6.0	2
Ovary	Permanent infertility	2.5 - 6.0	> 0.2
Lens of eye	Cataract	2.0 - 5.0	> 0.15
Bone marrow	Blood forming deficiency	0.5	> 0.4

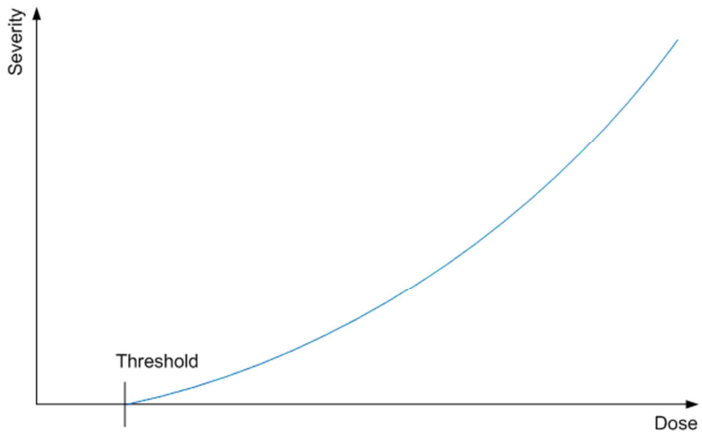

Figure 3-7: Deterministic effects and dose relationship

Radiation Sickness and Lethal Dose

Light radiation sickness occurs at doses of around 0.5 - 1 Gy, which may causes nausea, headache, higher infection risk and temporary infertility. With higher dose rates, the haemogram (blood picture) changes and the symptoms become stronger. The etiopatholgy (course of disease) begins with the development of the first symptoms a few hours after the exposure, followed by a recovery phase that lasts for one to two weeks, and a second phase, in which the symptoms reoccur. Higher doses intensify the etiopatholgy. The initial symptoms are much stronger and the second phase of the disease is accompanied by hair loss, exhaustion and possible internal and external bleedings. With an exposure between 2 and 6 Gy, lethality increases strongly. Characteristic effects at this

stage are cataract, erythema, and infertility. Above this exposure acute radiation syndrome (ARS) occurs. The etiopatholgy remains its two phase characteristic, but the symptoms become stronger and the mortality reaches 100%. The interphase is the so called “walking death phase”. During this phase many multiplying cells – especially in the bone marrow – are already destroyed but the surface effects do not appear due to remaining formerly build cells that are still working until used up. At higher doses the severity increases further and the disease has a shorter course. Above 50 Gy death occurs within a few moments through a complete breakdown of the nervous system.

The lethal doses (LD) due to ionizing radiation are dependent on the type of radiation and the physical condition of the individual. The most commonly-used lethality indicator is the LD50/30. It is the dose where half of the individuals die within 30 days after exposure without medical treatment. For humans the LD50/30 value is approximately 4 – 4.5 Gy and the LD100/30 value (100% mortality within 30 days) is above 6 Gy. [38]

Stochastic Radiation Effects

Stochastic effects are those that occur by chance and consist primarily of cancer and genetic effects. Stochastic effects usually show up years after exposure. Increased levels of exposure make these health effects more likely to occur, but do not influence the type or severity of the effect. In the dose range relevant for radiation protection purposes, inheritable damage, cancer and leukaemia belong to stochastic radiation damages. When cells of organisms are damaged, the protein synthesis can be changed or disturbed, which may lead to somatic mutation. The regeneration potential is limited, so that the somatic mutations are accumulated over lifetime. If damaged cells mutate in a way so that they can still divide, these mutations may lead to radiation-induced cancer. Similarly, for stochastic effects it is generally assumed that there is no threshold dose below which an adverse effect cannot occur. In addition, because stochastic effects can occur (at a much higher rate) in individuals that have not been exposed to radiation above background levels, it can never be determined for certain that an occurrence of cancer or genetic damage was due to a specific exposure. While it cannot be determined conclusively, it is often possible to estimate the probability that radiation exposure will cause a stochastic effect. The probability that stochastic radiation damage will occur differs widely for the irradiated individual organs or tissues. Especially with low dose rates the risk for human organisms is discussed controversial and is subject of numerous epidemiological studies.

3.2.2 Comparative Cohort Studies

To investigate the long-term health effects of airline crew members due to exposure to cosmic radiation epidemiological cohort studies were accomplished. In these studies, mortality and cancer incidents are compared between flight staff and expected numbers of respected national statistics. Special considerations were made for leukaemia and malignant melanoma, because of their strong association with radiation. [48]

Additionally, in studies of cabin crew members, close considerations were taken with regard to a possible risk of breast cancer. The size of an occupational group and the observation time are the main factors that influence the accuracy of studies expatiating stochastic effects. In the cohort studies the dose rates ranged on average between 2 and 5 mSv per year, with single maximum outliers between 0.5 and 9 mSv. Table 3-4 lists the cohort studies accounted for in this subchapter.

Table 3-4: Cohort studies of health effects of airline crew members due to exposure of cosmic radiation

Cohort studies			Participants
Cancer incidence studies			
[GUN1999]	Gundestrup et al. (1999)	Radiation-induced acute myeloid leukemia and other cancers in commercial jet cockpit crew: a populatation-based cohort study [49]	3877
[HAL2000]	Haldorsen et al. (2000)	Cancer incidence among Norwegian airline pilots [50]	3701
[HAL2001]	Haldorsen et al. (2001)	Cancer incidence among Norwegian cabin attendants [51]	3693
[LIN2003]	Linnersjö et al. (2003)	Cancer incidence in airline cabin crew: experience from Sweden). [52]	2956
[RAF2000]	Rafnsson et al. (2000)	Incidence of cancer among commercial airline pilots [53]	458
[RAF2003A]	Rafnsson et al. (2003)	Breast cancer risk in airline cabin attendants: a nested case-control study in Iceland [54]	1532
[BAN1996] [ɟ]	Band et al. (1996)	Cohort study of Air Canada pilots: mortality, cancer incidence, and leukemia risk [55]	2740
Cancer mortality studies			
[BLE2003]	Blettner et al. (2003)	Mortality from cancer and other causes among male airline cockpit crew in Europe [56]	28066
[LAN2003]	Langer et al. (2003)	Cosmic radiation and cancer mortality among airline pilots: results from a European cohort study (ESCAPE) [57]	19184
[ZEE2003]	Zeeb et al. (2003)	Mortality from cancer and other causes among airline cabin attendants in Europe: a collaborative cohort study in eight countries [58]	44142
[BAN1996] [ɟ]	Band et al. (1996)	Cohort study of Air Canada pilots: mortality, cancer incidence, and leukemia risk [55]	2740

[ɟ] … in the [BAN1996] study incidence and mortality occurrences were evaluated

Data Acquisition

Various data sources were used for the cohort studies, including airline personnel files, data from airline pilots associations, personal records, licence data of the national airline associations and medical files. Based on the annual flight hours[5] and the operated aircraft types, radiation exposure due to cosmic radiation was estimated. [57][58] If available, flight hours from periods prior to the employment period recorded at the respective airlines were included. Follow-up for the cause-specific incidences of each individual started at the first date of employment or licensing, at immigration, or the country-specific start of follow-up, whichever was latest and ended at date of death, date of loss to follow-up, emigration or at the end of the study period whichever was first. [57][58] Death and population registries were the most common sources as follow up methods for mortality studies. Medical files and cancer registries were used for studies concerning cancer incidences.

Analysis and Modelling

In mortality studies the association between occupational radiation exposure and mortality was initially analysed for the cause of death group “all causes”, and for the group “all cancers”. As the number of deaths of specific subgroups of cancer were too small to do more refined analyses, in the cohort studies all cancers known to be associated with ionizing radiation according to the UNSCEAR Report 2000 (Table 3-5) were combined into a group “radiation-related cancers” (RRC). Separate analyses were also performed for leukaemia – known to be strongly associated with radiation – and for malignant melanoma. Other cancers than RRC were grouped as “non-radiation-related cancers” (NRRC). For risk estimates due to radiation exposure, it was expected that RRC and NRRC could show different patterns.

[5] The typical measurement for flight hours in commercial aviation are the block hours, the time between the first movement of an aircraft (block off) and the time when the aircraft’s engines are shut down at the final parking position (block on). Hence, the block time is longer than the actual airborne time (between take-off and landing). Generally, the relative difference decreases as the flight time of a single flight increases.

Table 3-5: Grouped causes of death according to UNSCEAR report 2000 [48]

Group name (abbreviation)	Grouped causes
All causes	
All cancers	
Radiation related cancers (RRC)	Cancers of oesophagus, stomach, large intestine,bladder/other urinary tract, thyroid gland and other endocrine, multiple myeloma, all leukaemias
All leukaemias	
Leukaemias non-CLL	Leukaemias excluding chronic lymphatic leukaemia (CLL)
Cancers rarely or never related to radiation (NRRC)	Other cancers than RRC
Malignant melanomas	

In cohort studies that analyse cancer incidence the occurrences were categorized according to their association with ionizing radiation. Due to the even smaller cohorts in most studies a detailed categorization was usually not possible, because the number of incidence were too small to be significant. Only the significantly higher occurrence of malignant melanoma and other skin cancer were analysed separately in all cohort studies.
In studies about cabin attendants ([RAF2003A][54] and [ZEE2003][58]) the risk of female breast cancer was investigated. Lung cancer was excluded from analysis, because in no cohort information on smoking behaviour among the participants was available.

Abbreviations and Definitions

The *standardized mortality ratio (SMR)* in epidemiology is the ratio of observed deaths (*O*) to expected deaths (*E*) according to a specific health outcome in a population and serves as an indirect means of adjusting a rate. The figure for observed deaths is usually obtained for a particular sample of a population. The figure for expected deaths reflects the number of deaths for the larger population, from which the study sample has been taken, e.g. national level of mortality attributed to a particular health outcome. [62]

The *standardized incidence ratio (SIR)* is an estimate of the occurrence of cancer in a population relative to what might be expected if the population had the same cancer experience as some larger comparative population designated as “normal” or average. Usually, the country as a whole is selected to be the comparative population. [62]

The *significance level* or critical *p-value* describes the amount of evidence required to accept that an event is unlikely to have arisen by chance. The *p-value* is the probability of obtaining by chance a

result at least as extreme as that observed, even when the null hypothesis H_0 (there is no significant difference) is true and no real difference exists. [64] At lower p-values the result is statistically more significant. Usually it is assumed, that the sample results are deemed statistically significant if $p \leq 0.05$.

A *confidence interval (CI)* allows interpreting the reliability of an estimate within a specific range. How frequently the observed interval contains the parameter is determined by the *confidence level*. As a general convention, epidemiologists usually work at a *confidence level* of 95% (CI95).

The *relative risk* (*RR*) in statistics and mathematical epidemiology, is the risk of an event (or of developing a disease) relative to exposure. [63] Relative risk is a ratio of the probability of the event occurring in the exposed group versus a non-exposed group. RR < 1 means the event is less likely to occur in the experimental group than in the control group and RR > 1 means the event is more likely to occur in the experimental group than in the control group.

The *coefficient of determination*, R^2, is used in the context of statistical models whose main purpose is the prediction of future outcomes on the basis of other related information. It is the proportion of variability in a data set that is accounted for by the statistical model. [62] It provides a measure of how well future outcomes are likely to be predicted by the model.

There are several different definitions of R^2, which are only sometimes equivalent. One class of such cases includes that of linear regression. In this case, R^2 is simply the square of the sample correlation coefficient between the outcomes and their predicted values, or in the case of simple linear regression, between the outcome and the values being used for prediction. In such cases, the values vary from 0 to 1. [62]

Cancer Incidence Studies

Cancer incidence studies have the advantage that the direct risk of cancer incidence is presented regardless of its medical therapy result. A major difficulty is the acquisition and the follow-up of the medical data. Detailed information of the incident must be available and correct indication of the medical diagnosis is required. This requirement has also to be obtained in the follow-up, which causes a higher documentation effort. Hence, published incidence studies used smaller cohorts than mortality studies. The SIR of the compared incident studies are summarized in Table 3-6.

Table 3-6: Standardized incidence ratio (SIR) of cancer in incidence cohort studies

Standardized incidence ratio					
	Participants	All cancer (CI95)	Malignant melanoma (CI95)	Other skin cancer† (CI95)	Breast cancer ♀ (CI95)
[GUN1999]	3877	1.1(0.94-1.28)	5.1(1.03-14.91)	3.0(2.12-4.23)	
[HAL2000]	3701	1.06(0.92-1.22)	1.8(1.1-2.7)	2.4(1.3-4.0)	
[HAL2001]♀	3105	1.1(0.9-1.3)			1.1(0.8-1.5)
[HAL2001] ♂	588	1.7(1.3-2.2)			
[LIN2003] ♀	2324	1.01(0.78-1.24)	2.18(1.09 – 3.90)		1.30(0.85-1.74)
[LIN2003] ♂	632	1.16(0.76-1.55)	3.66(1.34 – 7.97)		
[RAF2000]	458	0.97(0.62-1.46)	10.20(3.29-23.81)		
[RAF2003]	1532				5.24(1.58-17.38)
[BAN1996]	2740	0.71 CI90:(0.61-0.82)	4.72 CI90:(2.05-9.31)		

† …skin cancer excluding malignant melanoma

In the compared studies no significant general cancer risk was found. However, the occurrence of malignant melanoma and skin cancer was noticeably higher. The especially high number of malignant melanoma in [RAF2000] [53] study will be discussed separately in this chapter. At cohort studies that examine female breast cancer also an increased number of occurrences was observed.

Mortality Studies

The largest published cohort studies are cancer mortality studies. Expected values based on national population mortality rates were calculated and the data were compared to the respective national population and death registries. Table 3-7 summarizes the SMR of the compared incident studies.

Table 3-7: Standardized mortality ratio (SMR) in mortality cohort studies

Standardized mortality ratio						
	Participants	All causes of death (CI95)	All cancer (CI95)	Malignant melanoma (CI95)	Leukaemia (CI95)	Breast cancer (female) (CI95)
[BLE2003]	28066	0.64 (0.61-0.64)	0.68 (0.63-0.74)	1.78 (1.15 – 2.67)	1.05 (0.69-1.50)	
[LAN2003]	19184	0.70 (0.67-0.74)	0.72 (0.64-0.82)	1.57 (0.51-4.90)[M]	1.0 (0.32-3.06)[M]	
[ZEE2003] ♀	33063	0.80 (0.73-0.88)	0.80 (0.73-0.88)		0.99 (0.46-2.08)	1.11 (0.82-1.48)
[ZEE2003] ♂	11079		1.09 (1.00-1.18)	1.93 (0.70-4.44)		
[BAN1996]	2740	0.63 CI90: (0.56-0.70)	0.61 CI90: (0.48-0.76)	1.32 CI90: (0.23-4.15)	0.86 CI 90: (023-2.22)	

[M]… in [LAN2003] the SMR was published for several subchorts. The given values in this table represent the highest SMR of the subcohorts (for more details see Table 3-8)

The analysis of cancer mortality studies shows a generally low mortality compared to the general population during the observed periods. Also, the cancer mortality risk was below average. Concerning various cancer types, malignant melanoma and other skin cancer showed a higher SMR. Also, a slightly higher number of breast cancer mortality was observed (not significant).

ESCAPE Study

The ESCAPE study [57] is a large collaborative European cohort study published in 2003. In this study classification according to the cumulative block hours[6] of pilots was made. Therefore, the result of this study are presented in detail to demonstrate possible trends of cancer risk in connection to the respective cumulative dose due to cosmic radiation during flight. Mean annual doses were in the range of 2-5 mSv and cumulative lifetime doses did not exceed 80 mSv. [57] Table 3-8 shows the results of different cancers with respect to the cumulative dose of the ESCAPE study.

Table 3-8: Relative risks (RR) for cumulative radiation dose adjusted for age, ESCAPE study, 1960–1997. Goodness of fit of the used Poisson model is documented by the scaling factor and R^2-measure [57]

Causes of death (ICD-9 code)	Cumulative dose (mSv)	Number of deaths	RR	95% CI	Scaling factor	R2	*P*-value (trend test)
All causes[b]	0–4.99	493	1.0	–	1.01	0.90	<0.0001
	5.0–14.99	298	0.68	0.58–0.78			
	15.0–24.99	287	0.71	0.61–0.83			
	25.0+	156	0.54	0.45–0.66			
All cancers	0–4.99	105	1.0		1.14	0.93	0.101
	5.0–14.99	74	0.75	0.53–1.05			
	15.0–24.99	93	0.79	0.58–1.09			
	25.0+	66	0.74	0.51–1.06			
Radiation-related cancers (RRC)	0–4.99	27	1.0		1.04	0.80	0.645
	5.0–14.99	21	0.81	0.44–1.47			
	15.0–24.99	28	0.95	0.54–1.65			
	25.0+	18	0.82	0.43–1.55			
All leukaemias	0–4.99	5	1.0		0.97	0.36	0.624
	5.0–14.99	7	1.52	0.49–4.68			
	15.0–24.99	4	0.83	0.23–3.06			
	25.0+	3	0.81	0.19–3.43			
Leukaemias non-CLL[a]	0–4.99	4	1.0		0.88	0.36	0.567
	5.0–14.99	5	1.56	0.48–5.04			
	15.0–24.99	2	0.75	0.16–3.51			
	25.0+	3	2.00	0.49–8.08			
Cancers rarely or never related to radiation (NRRC)	0–4.99	78	1.0		1.04	0.91	0.067
	5.0–14.99	53	0.72	0.50–1.04			
	15.0–24.99	65	0.74	0.531.05			
	25.0+	48	0.71	0.48–1.04			
Malignant melanomas	0–4.99	5	1.0		0.78	0.25	0.481
	5.0–14.99	3	0.71	0.23–2.18			
	15.0–24.99	5	1.26	0.45–3.50			
	25.0+	1	0.33	0.06–1.85			

[a] Germany excluded because no subtype of leukaemia available.
[b] Also adjusted for calendar period.

[6] The typical time that is recorded in the pilot logbook is the block time, which is the time between *block off* – when an aircraft starts to move or be moved – and *block on* – when an aircraft stops at its final parking position.

The standard mortality ratio (SMR) and relative risk (RR) analysis did not show any clear pattern with radiation dose. In the ESCAPE study, one finds even a decreasing risk with increasing dose for total mortality. This effect may be interpreted partly by the “healthy worker effect” due to relatively high health standards that are required to become an aircrew member. Another trend that is difficult to separate is that overall mortality has decreased during the past decades, while the cumulative lifetime dose is increasing with time. It varies slightly between the different cancer groups without clear tendencies or significance.

In the ESCAPE study the mean total block hours at the end of the observation period has been 7,031 for all pilots of the cohort (retired pilots 7,218). The mean total lifetime radiation dose was 15.3 mSv (maximum 78.5 mSv). The retired pilots showed lower values; mean 13.3 mSv. This can be explained by the fact that during the past decades an almost continuous increase of the 10-year moving averages of dose per block hour was found. [57]

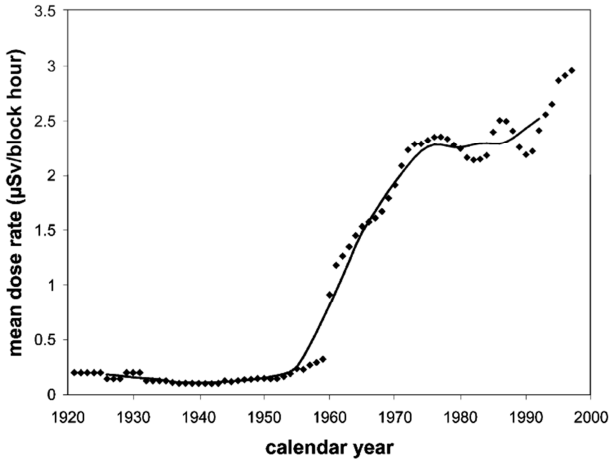

Figure 3-8: Radiation exposure of cockpit crew expressed as calendar year mean (full diamonds) and 10-year moving averages (solid line) for dose per block hour. [57]

With the beginning of the jet era around 1960, a steep increase was noted. An increase of the 10-year means still seemed to be present. Hence, it is expected that the lifetime radiation dose will increase in the next decades.

Radiation-related Cancers

In general, the occurrence of radiation-related cancer (RRC) - regardless of its subtype - did not show any significant deviation between the aircrew personal and the general population. Concerning trends at increasing radiation dose, neither for the RRC-class, all leukaemia, nor for the subclass, leukaemia excluding chronic lymphoid leukaemia (CLL), a clear pattern of mortality risks was

observed. Female cabin attendants showed an increase of breast cancer but there were only few single cases, so that these individual cases deliver no general information for a statistically higher risk factor. In studies that considered the cumulative dose till the incidence, no direct relation to the cumulative dose could be determined.

Malignant Melanoma

In cancer incidence cohort studies [49][50][52][53][54] as well as in other cohort studies [57][58], there was a tendency for increased occurrence of malignant melanoma among pilots. In mortality studies, the relative risk of melanoma appeared considerably lower but still significantly above 1.0. The risk of melanoma is difficult to investigate within mortality studies, because of the high survival rate for this disease. In these studies an increased risk for malignant melanoma of the skin has been a relatively consistent finding which, however, was mainly attributed to UV-radiation and the link between malignant melanoma and ionizing radiation remains unclear. [65] Occupational UV-exposure for pilots is unlikely since the cockpit windows provide sufficient protection. [66]

The [RAF2000][53] cancer incidence cohort study among commercial airline pilots showed an exceptionally high number of malignant melanoma incidences. At closer consideration the relative risk was especially high for flight crews operating on international routes. This lead to discussion what role exposure of cosmic radiation, number of block hours, or lifestyle factors – such as possible excessive sunbathing – play in the aetiology of cancer among pilots. Especially pilots with Nordic skin types were known for the increase risk of sunburn and the risk involved.

Therefore, the same authors published a cross sectional study in Iceland, [RAF2003b][60]. In this study 239 male pilots and 856 female cabin attendants were compared with 454 males and 1464 females of the same age, drawn randomly from the general population. The investigated difference in constitutional and behavioural risk factors for malignant melanoma between the aircrews and the population sample was found only small and not substantial. The aircrews had more often used sunscreen and had taken more sunny vacations than the other men and women. The predictive values for use of sunscreen were 0.88 for pilots and 0.85 for cabin attendants and the predictive values for sunny vacation were 1.36 and 1.34, respectively. Thus, it is unlikely that the increased incidence of malignant melanoma found in previous studies of pilots and cabin attendants can be solely explained by excessive sun exposure. [60]

Though this study did not show any major difference in UV-exposure between aircrew and the general population, intensive sun exposure during leisure time has been postulated as a potential cause for melanoma among aircrews. Evidence is, however, restricted as the behaviour might have changed in time and in general population an increase of incidence of malignant melanoma is

observed over the last decades. [60] Furthermore, due to cultural differences between the European countries the results may not be representative generally.

Healthy Workers Effect

Generally, aircrew personal has better state of health than the overall population, due the necessity to meet the mental and physical requirements for their job. Every airline has special assessments for recruitment that evaluate the medical status of a candidate. Furthermore, annual routine medical checks are mandatory by law. To hold an active airline transportation pilots licence (ATPL) a *medical certificate class I*[7] must be obtained. This is the highest medical certificate class for aviation and must be renewed at least every year.

In [LAN2003][57] and [ZEE2003][58] it was investigated, whether the healthy workers effect disappears over time. There was no indication that the low mortality observed for all causes and cardiovascular causes changed with increasing time since first exposure. [58]

This can partly be explained because frequent medical checks lead to earlier diagnosis and hence to better chances for a successful therapeutic treatment.

Work-related Risk Factors

Airline crew members have several work-related risk factors besides the exposure to cosmic radiation. Some of the most common factors have been published by the German Radiation Protection Commission (*Strahlenschutzkommission*) [67]:

- noisiness
- secondary smoking (only valid for the years before a general ban of smoking was established on board)
- long work schedules
- disturbance of the circadian rhythm (irregular work schedules, irregular mealtime)
- time shifts due to flights through many different time zones
- frequent and strong climate changes
- uncommon and exotic meals
- UV-radiation
- special life-style (especially: vacation and leisure time in sunny areas)

[7] in accordance with ICAO (International Civil Aviation Organization) standards (Annex1) (e.g. implemented in JAR-FCL (Joint Aviation Authorities – Flight Crew Licensing) for European flight licences)

The work-related risk factors and the strong healthy workers effect make any comparison with an occupational group that has the same requirements difficult. The occurrences of individual cancer types in cohort studies were sporadically and therefore of low statistical significance. Generally, it is expected that the cumulative lifetime dose will increase in the next decades due to increased flight-time in higher altitudes and more total flight hours in average airline-careers. Hence, a monitoring of relative risk is essential, preferably in very large cohort studies.

Chapter 4

Thermoluminescence Dosimetry

4.1 Introduction

Thermoluminescence is a special form of luminescence. It is the thermally stimulated emission of light, following the previous absorption of energy from ionizing radiation[8]. For the production of thermoluminescence a material must have specific properties. “Firstly, the material must be an insulator or a semiconductor[9] – metals do not exhibit luminescence properties. Secondly, the material must have at some time absorbed energy during exposure to radiation. Thirdly, the luminescence emission is triggered by heating the material.” [69] Typical thermoluminescence dosemeters are crystalline materials – e.g. lithium fluoride or calcium fluoride phosphors used in this study. These phosphors are able to store energy at meta-stable states. By heating, the previously absorbed energy in the crystals is re-emitted as light, the so-called thermoluminescence. The measurement of thermoluminescence intensity allows for an analysis of the accumulated radiation dose. Thermoluminescence dosimetry has several advantages for aviation radiation measurements. It is a completely passive system that neither needs power supply nor emits electromagnetic radiation and therefore no air-worthiness certification is required. The crystals are – compared with other dosimetry systems – cheap in production, small in size, and can be reused.

[8] This is not to be confused with thermal radiation or black body radiation.

[9] Thermoluminescence in semiconductors is irrelevant for practical applications due to their small band gap.

4.2 Luminescence

Luminescence is light emission defined as follows: "When [ionizing] radiation[10] is incident on a material some of its energy may be absorbed and re-emitted as light of a longer wavelength (Stoke's Law)." [69] The absorbed energy is stored as potential energy, which further, partially or completely is emitted as luminescence light. "In general, luminescence emission is explained by the transfer of energy from radiation to the electrons of the solid, thus exciting the electrons from a ground state *g* to an excited state *e*. The emission of a luminescence photon takes place when an excited electron returns to its ground state." [69] Luminescence does not follow the Planck's black-body law, and instead it manifests itself as additional emission in excess of the black-body radiation of a specimen at a particular temperature.

The emission of luminescence radiation takes place a characteristic time τ_c after the absorption. "The value of $\tau_c < 10^{-8}$ provides a definition for the essential spontaneous process of fluorescence." [69] The spontaneous fluorescence emission is depicted as taking place simultaneously with the energy absorption and this process is temperature independent.

A further class of luminescence is phosphorescence. Phosphorescence is characterized by a delay between the energy absorption and the time t_{max} to reach full intensity and continues for some time after the excitation has been removed. For phosphorescence, the presence of a metastable level m in the "forbidden" energy gap between *e* and *g* is necessary. (Figure 4-1) "An electron excited from *g* to *e* can now become trapped at *m* where it will remain until it is given enough energy *E* to return to *e* where it can undergo a normal transition to *g*, with the subsequent emission of light." [69]

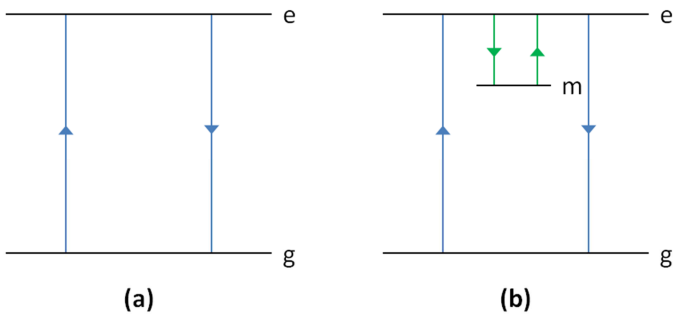

Figure 4-1: Energy transitions involved in the production of (a) fluorescence and (b) phosphorescence [69]

[10] In addition to excitation by radiation, luminescence can also be generated by chemical reactions, electrical energy, mechanical stress, etc. [69]

The delay between the energy absorption and the phosphorescence corresponds to the time the electron stays in the electron trap. From thermodynamic arguments, it can be shown that the mean time spent in the trap τ at temperature T is given by

$$\tau = s^{-1} \exp(E / kT) \tag{4.1}$$

E is the trap depth (the energy difference between the conduction band and the trap level), s is the attempt-to-escape frequency and k the Boltzmann's constant. [69]

This equation shows that the mean lifetime is exponentially dependent upon temperature. If the trap is deep enough at a given temperature T_0

$$E >> k\,T_0 \tag{4.2}$$

τ becomes very large.

This means that electrons will remain trapped in level m (practically) infinitely and the release rate of electrons dn/dt is negligibly small.

$$\frac{dn}{dt} = -\frac{n}{\tau} \xrightarrow[T_0]{} 0 \tag{4.3}$$

However, luminescence can be induced by heating. Raising the temperature T results in an exponential decrease of τ. The electrons are released from the trap and recombination takes place. This class of thermally induced luminescence is called thermoluminescence.

4.3 Thermoluminescence

Thermoluminescence phenomena were for the first time described in the 17th century. Although qualitative and quantitative characteristics of thermoluminescence have been analysed since the end of the 19th century, there still is no generally accepted theoretical model to explain the dosimetric characteristics in every detail. The theoretical explanation of thermoluminescence use models based on the energy band theory. Only insulators that have energy levels in the forbidden band have thermoluminescence capability. It is necessary to store the excitation energy in these metastable energy levels. These "trap-levels" can be induced to an insulator by lattice defects or impurities. Typical materials used are lithium fluoride or calcium fluoride doped with various elements like titanium, magnesium or thulium. The material must have at some time absorbed energy during exposure to radiation. The thermoluminescence emission is triggered by heating the material. For analysis, the dosimetry material usually is heated at a constant rate dT/dt. The measured emission is plotted over temperature to yield the characteristic *glow curve*. Several models have been developed, which permit a calculation of glow curve parameters.

4.4 Thermoluminescence Models

Kinematic theories about thermoluminescence are based on the energy band model of solids. In this model, in the energy-gap of an insulating crystal discrete activator terms above the valence band (energy level E_v) and discrete traps beneath the conduction band (energy level E_c) are assumed. In the ground state, all activator terms are occupied with electrons and all traps are empty. Upon absorption of radiation energy, electrons from the valence band are excited into the conduction band. To raise an electron from the valence to the conduction band, the energy of the absorbed radiation has to be greater than the band-gap[11] (E_g).

$$(h\nu)_a > E_c - E_v = E_g \tag{4.4}$$

The free charge carriers in the conduction band may transit to the valence band, where they recombine, or alternatively transit to the discrete traps because a transit from these levels to the valence band is forbidden by the Pauli exclusion principle. By sufficient energy input – e.g. heating – the carriers in the trap levels can be released to the conduction band and further recombine by emission of thermoluminescence. By recording the intensity of the emitted thermoluminescence light, it is possible to calculate the previously absorbed energy of the dosemeter crystal.

The normal way of displaying thermoluminescence data is to plot the luminescence intensity as a function of temperature – known as a “glow-curve”. The temperature at which the peak maximum appears is related to the trap depth and the area under each peak or the peak height is related to the amount of radiation initially imparted to the specimen. [69]

4.4.1 Two-level Model

In the simplest model, there are just two localized levels in the energy band scheme. One is situated beneath the valence band and acts as an electron trap, and the other one is above the conduction band and acts as recombination centre or activator. The equilibrium Fermi level is located between the two levels and, therefore, the higher level is empty at the equilibrium state and acts as an electron trap, while the lower level acts as a hole trap. Furthermore, this model assumes that transition between the discrete levels and the valence band is forbidden. Possible electronic transitions in an electrical insulator are shown in Figure 4-2.

The explanations in this model can be specified equivalently for electrons and holes. For descriptive reasons, only electrons will be considered in the following.

[11] Typically band gap energies E_g of insulators are greater than 3 eV.

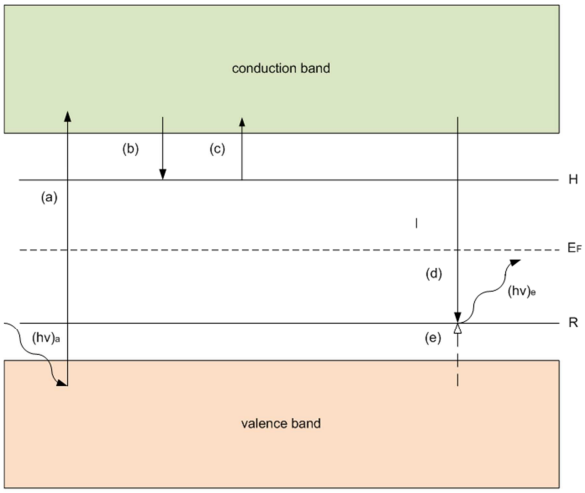

(a) ionization (c) thermal release E_F Fermi level R recombination centre
(b) and (e) trapping (d) radiative recombination H electron trap

Figure 4-2: Two-level model for thermoluminescence

The following formalism is based on N. Riehl, 1971 [68].

Table 4-1: List of used symbols [68]

Symbols	
A	Transition coefficient for electron release
B	Transition coefficient for electron re-trapping
Γ	Transition coefficient for recombination /
α_0	Attempt to escape frequency
E	Gab energy between valence and conduction band
e_0	Elementary charge (1.602176487(40). 10-19 C)
F	Concentration of free charge carriers in the recombination centres
f_0	Excess of free charge carriers in the recombination centres (activators)
H	Density of electron traps centres
H	Concentration of trapped electrons
h_0	Concentration of trapped electrons h at temperature T0
I	Intensity of thermoluminescence light
k	Boltzmann's constant (1.380 6504(24). 10^{-23} J K^{-1} / 8.617 343(15). 10^{-5} eV K^{-1})
μ	Mobility of conduction electrons
n	Concentration of conduction electrons
q	Heating rate
σ	Conductivity of electrons
T	Temperature
T_0	Initial temperature at the beginning of the glow experiment
T_{max}	Temperature at the glow-maximum
T	Time
τ	Mean time electrons spend in the trap

The rate of thermally released electrons per unit time $A_{release}$ is proportional to the *concentration of the electrons in the traps h*.

$$A_{release} = \alpha\, h \tag{4.5a}$$

$$\alpha = \alpha_0\, e^{-\frac{E}{kT}} \tag{4.5b}$$

The re-trapping rate depends on the *density of available traps H*, the *concentration of trapped electrons h* and the *concentration of free charge carriers in the conduction band n*.

$$A_{re-trapping} = \beta\, n\,(H - h) \tag{4.6}$$

The parameters α and β are *transition coefficients*.

The thermoluminescence intensity is given by the number of radiative transitions per unit time and volume element of the crystal. It is proportional to the *concentration of free charge carriers in the recombination centres f* and the *recombination rate n*.

$$I(T) \sim \gamma\, n\, f \tag{4.7}$$

The *proportionality factor* γ is set to unity in further considerations, because for thermoluminescence measurements only the relative intensity with respect to a reference measurement is important.

The trap filling process can be described by differential equations, which describe the transitions of charge carriers between conduction and valence band, traps and recombination centres. The change in the electron concentration in the conduction band per unit time is given by

$$\frac{dn}{dt} = \alpha\, h - \beta\, n\,(H - h) - \gamma\, n\, f \tag{4.8}$$

and the change in the concentration of trapped electrons

$$\frac{dh}{dt} = -\alpha\, h + \beta\, n\,(H - h) \tag{4.9}$$

The overall charge neutrality must be considered by

$$f = n + h \tag{4.10}$$

To calculate the glow curve it is necessary to solve these differential equations. In general, this system of equations cannot be solved analytically. It is common to make some simplifying assumptions. The lifetime of the conduction-band electrons is short compared to the lifetime of the trapped electrons. So a low quasi-stationary electron concentration can be assumed at the conduction band.

$$n << h \tag{4.11a}$$

$$dn << dh \tag{4.11b}$$

The temperature gradient is assumed to be linear due to the constant heating rate used in thermoluminescence measurements.

$$dT = q\ dt \tag{4.12}$$

Considering these restrictions, equations 4.5 and 4.6 can be solved analytically for the special case of a re-trapping factor R=0, described by the *Randall and Wilkins* model, and R=1 as explained by *Garlick and Gibson*.

Randall and Wilkins Model

Randall and Wilkins calculated the thermoluminescence intensity for the simple two-level model under the assumption that no re-trapping occurs. With β=0, equations 4.5 and 4.6 become

$$q\frac{dn}{dT} = \alpha\, h - \gamma\, n\ f \tag{4.13a}$$

$$q\frac{dh}{dT} = -\alpha\, h \tag{4.13b}$$

The second equation shows that the gradient of concentration of trapped electrons over temperature is directly proportional to the concentration of electrons in the traps, which describes a first-order reaction and, therefore, monomolecular kinetics. To calculate the thermoluminescence intensity from these equations, it is important to consider the general condition *dn*<<*dh*. Under these considerations the *concentration of electrons in the traps h* can be expressed as a function of temperature *T* by solving the Equation 4.13b.

$$h(T) = h_0 \exp\left(-\frac{\alpha_0}{q} \int_{T_0}^{T} e^{-\frac{E}{kT}} dT \right) \tag{4.14}$$

Further on, summing up (4.13a) and (4.13b) leads to

$$q\frac{dh}{dT} = -\gamma\, n\ f\ . \tag{4.15}$$

This equation relates the intensity with the concentration of electrons in the traps by

$$I = \gamma\ n\ f \tag{4.16a}$$

$$I = \alpha\, h\,. \tag{4.16b}$$

Thus, the intensity *I(T)* of the thermoluminescence emission can be written as

$$I(T) = \alpha_0\ h_0\ e^{-\frac{E}{kT}} \exp\left(-\frac{\alpha_0}{q} \int_{T_0}^{T} e^{-\frac{E}{kT}} dT \right) \tag{4.17}$$

In this equation, the first exponential function explains the rise, the second exponential function the descend of the glow curve. If reasonable values are assumed for α_0 (~10^{10}s^{-1}) and *E*, the glow curves

of the Randall-Wilkins model have a typical asymmetrical shape. An increase follows a steep descend. The major problem of this model is the predicted conductivity. The electrical conductivity σ is proportional to the concentration of conduction-band electrons.

$$\sigma = n\, e_0\, \mu \tag{4.18}$$

With n<<h and f~h, Equation 4.15 can be written as

$$q\frac{dh}{dT} = -\gamma\, n\, h \tag{4.19}$$

With regard to (4.13b) the concentration of conduction-band electrons is given-by

$$n = \frac{\alpha}{\gamma} = \frac{\alpha_0}{\gamma} e^{-\frac{E}{kT}} \tag{4.20}$$

This result is physically not reasonable, because the exponential ascend of the conduction-band electrons is not followed by a descend, and with increasing temperature, the conductivity would rise infinitely. High values of T lead to $n>>h$, which conflicts with the assumption (4.11) at the beginning.

An approach to solve this problem would be the assumption of an excess of *free charge carriers in the recombination centres (*activators) f_0.

$$f = f_0 + n + h \approx f_0 \tag{4.21}$$

An excess of free activators causes the lifetime of electrons in the conduction band to be adequately small and the assumption n<<h stays plausible. This modification of the model would solve the particular problem of infinitely rising conductivity as it establishes a maximum, but further assumptions have to be made in order to adapt this model to actual experimental behavior.

Garlick and Gibson Model

The physicists *Garlick and Gibson* developed another analytical solution of the two-level model for the special case $\beta = \gamma$ *(*$R = \beta/\gamma = 1$*).* This approach considers that released electrons have a certain probability to be re-trapped. It assumes that if there is the same concentration of carriers in the recombination centre and the trap level, the probability of a recombination or re-trapping is equal.

In the *Garlick-Gibson model,* the gradient of *concentration of electrons in the traps h* over temperature is proportional to the square of the *concentration of electrons in the traps* h^2, and therefore a second-order reaction.

$$\frac{dh}{dT} = h^2 \tag{4.22}$$

Contrary to the *Randall-Wilkins model,* the approximation f~h (concentration of free recombination centres equals approximately the concentration of trapped electrons) and n<<h (the concentration of

the conduction-band electrons is small compared to the concentration of trapped electrons) is permissible, because the re-trapping transition causes the lifetime of free electrons in the conduction band to be sufficiently small.

4.4.2 Further Considerations of Thermoluminescence Models

The described theories contain various assumptions to simplify the calculation. Therefore, it must be considered that these simple models have strong limitations in their significance for actual glow curves. All described theories are based on a two-level model with only one trapping and one recombination centre, while all real thermoluminescence phosphors have far more complex structures. Further, the analytical models of *Garlick-Gibson* and *Randall-Wilkins*, are limited to a re-trapping factor of R=0 or R=1, respectively. Numerical methods can be used to calculate glow curves for various re-trapping factors by interpolation. Based on experimental measurements, the re-trapping factor has been evaluated to range between 0 to 10^4, dependent on the characteristics of the particular thermoluminescence substance (Figure 4-3). [69]

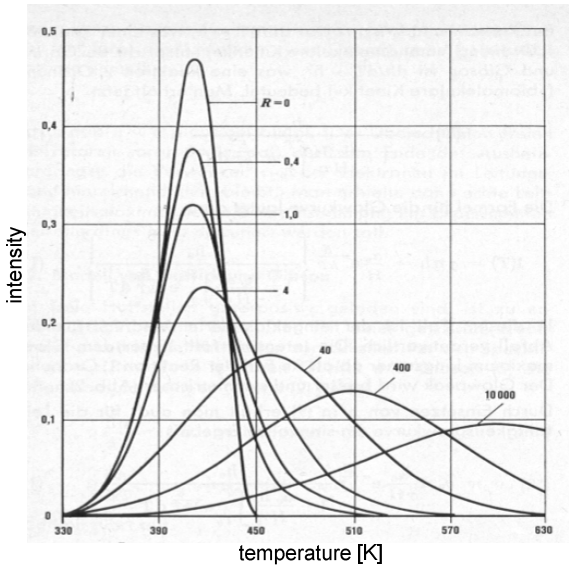

Figure 4-3: Thermoluminescence glow curves with different re-trapping factors R [68]

Generally, these numerical models show that for greater re-trapping factors R the width of the peaks increases and the maxima are shifted to higher temperatures. For detailed calculations, it is required to assess the model parameters (the *trap depth E* and the *attempt-to-escape frequency* α_0 of specific trap levels) by fitting them to the actual glow experiments. [68]

4.5 Thermoluminescence Dosemeters

Thermoluminescence dosemeters (TLD) used for radiation dosimetry should have specific characteristics. Beside the required thermoluminescence property, the material must be sufficiently sensitive to radiation with respect to the intended application and there should be no significant – or at least well known – fading effects at ambient (measurement) temperatures.

At the beginning of the development of TLDs, the phosphor lithium fluoride (LiF) was found to be a particularly good material because of its high thermoluminescence response and the small dimensions of the dosemeters. However, “natural” LiF has unpredictable TL properties and it is difficult to estimate the received dose. The presence of impurities within a crystal enhances the thermoluminescence response and the development of lithium fluoride phosphors with carefully controlled dopant concentrations lead to commercial application of thermoluminescence dosimetry. Nowadays, many thermoluminescence phosphors are known, which fulfill the requirements for various dosimetry applications.

TLD-600 / TLD-700

The most commonly used TLDs are lithium fluoride detectors doped with magnesium and titanium (LiF:Mg,Ti). The detectors are usually referred to their trade names. TLD-100 refers to LiF:Mg,Ti, with natural abundance of lithium isotopes, produced by Thermo Fisher Scientific (former Harshaw). TLD-600 and TLD-700 are enriched in ^{6}Li (TLD-600) and ^{7}Li (TLD-700), respectively. They are extruded chips, the materials is pounded to powder and thereafter pressed to homogenous chips. Other companies and institutes produce dosemeter crystals of comparable chemical composition under different trade names. Measurement properties are shown in Table 4-2. The main advantage of these crystals is the low effective atomic number of 8.3. This characteristic causes a nearly tissue-equivalent absorption of high-energy photons (> 6MeV) and, therefore, lithium fluoride is one of the most frequently used crystals in thermoluminescence dosimetry.

Beside the measurement of the absorbed dose, advanced experimental techniques were used in this assessment to obtain more detailed information about the measured radiation. The high-temperature ratio (HTR) and the extended pair (EP) methods enable the assessment of the biologically relevant dose equivalent and the neutron contribution. [71]

Table 4-2: Characteristics of thermoluminescence dosemeters [68]

	CaF2	LiF		
	TLD-300	TLD-100	TLD-600	TLD-700
Lower limit of linear response	10 µGy	1 mGy	1 mGy	1 mGy
Upper limit of linear response	1000 Gy	1000 Gy	1000 Gy	1000 Gy
γ -energy sensitivity†	8	1.3	1.3	1.3
Neutron sensitivity ├	0.02	0.025	320	2.5
Effective atomic number	16.3	8.3	8.3	8.3

†ratio to the maximum of ^{60}Co-γ-reference radiation
├ratio of equivalent thermal neutron to ^{60}CO gamma ray doses

TLD-300

For the experimental assessment of cosmic radiation in this thesis TLD-300 calcium fluoride dosemeters doped with thulium (CaF_2:Tm), produced by Thermo Fisher Scientific were used additionally to the TLD-600/700 dosemeters. In contrast to the TLD-600/700, TLD-300 dosemeter are single crystals. Measurement properties are shown in Table 4-2. The TLD-300 measurements were compared to the results from TLD-600/700 to evaluate the differences and applicability of the different dosemeter types. While TLD-300 have negligible fading of peak 5, it must be considered that there is a notable fading effect of peak 3 at ambient temperature. Further, the calcium fluoride dosemeters have a generally higher sensitivity than LiF:Mg,Ti and they have a significantly higher response at lower energies in the typical X-ray range. This energy dependence is shown in Figure 4-4. Therefore, it is expected that the X-ray exposure during security scans might bias considerably the TL signal from cosmic radiation.

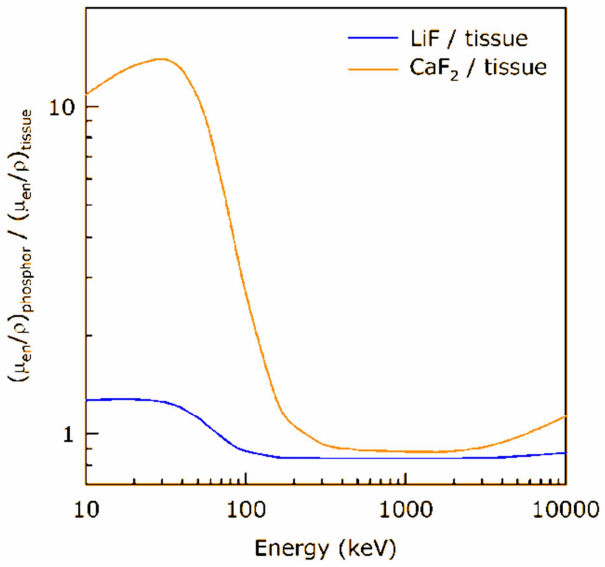

Figure 4-4: Different energy dependence of LiF and CaF_2 with respect to tissue

Glow Curve

The detectors are evaluated by measurement of the intensity of thermoluminescence light as a function of temperature, which yields the so-called glow curve. Typically, this glow curve has several peaks that correspond to different trap levels. The maximum of the TL peaks is used to calculate the previously received absorbed dose of a TLD. The measurements are compared to calibration measurements in a well-known radiation field. Within a specific range, the intensity of the thermoluminescence light of a glow-peak and the absorbed dose show a linear proportionality that is utilized for measurement.

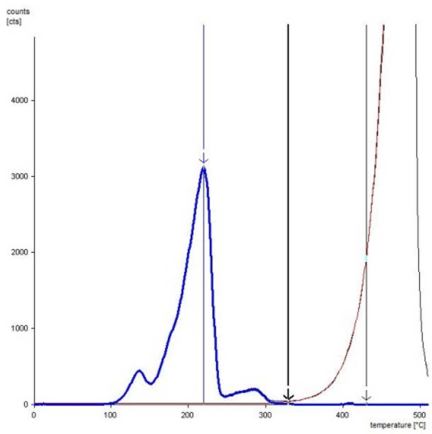

Figure 4-5: Sample Glow Curve from TLD-700

Black curve - Measured glow curve
Blue curve - Net glow curve
Red curve - Residual background

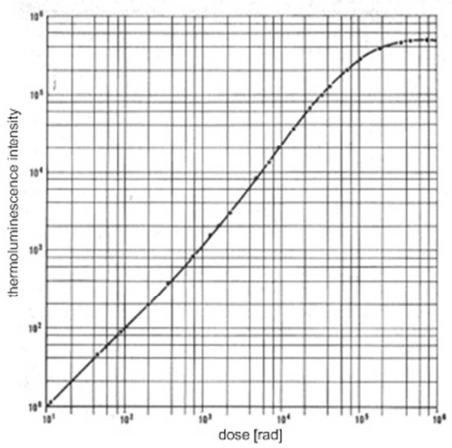

Figure 4-6: Thermoluminescence dose response of LiF:Mg,Ti [68]

Fading

For the applicability of a specific TL dosemeter the fading characteristics of the dosemeter material must be considered. The spontaneous release of electrons from their traps must be sufficiently small at ambient (measurement) temperature within the measurement and storage period to obtain reasonable results. The mean lifetime of electrons in the trap is strongly dependent on the trap depth (see equation 4.1), so that a lower trap depth leads to an exponentially increasing fading effect.

Extended Pair Method

The lithium fluoride detectors TLD-600 and TLD-700 differ only in the used lithium isotope enrichment ^{6}Li (TLD-600) and ^{7}Li (TLD-700). The phosphors have very similar detection characteristics except for their neutron sensitivity (see Table 4-2). Simultaneous measurement with the neutron sensitive TLD-600 and the almost neutron-intensive TLD-700 can be used to determine

the neutron contribution of the radiation. The difference in the peak 5 readings can be used to determine the neutron dose that was accumulated. The different neutron sensitivities of TLD-600 and TLD-700 are commonly applied to detect neutrons for energies < 200 keV. For aviation measurements the dosemeters were calibrated in the CERN-EU High-Energy Reference Field (CERF) [77], which simulates the cosmic-ray-induced neutron spectrum in good detail. [71][73] This enables the dose assessment of neutrons with energies up to several GeV with reasonable accuracy.

Chapter 5

Experimental Assessment

5.1 Measurement Setup

The thermoluminescence dosimetry system DOSFLIP was used for data assessment. This system was developed at the *Institute of Atomic and Subatomic Physics* of the *Vienna University of Technology*. The DOSFLIP packages contain TLD-700, TLD-600 and TLD-300 thermoluminescence dosemeters. Forty pilots of *Tyrolean Airways Tiroler Luftfahrt GmbH* participated in this experimental study. The dosemeters were carried on three different aircraft types operating on short- and mid-range flight routes; *Fokker 70/100*, *Bombardier Canadair Regional Jet (CRJ)-100/200* and *Bombardier Dash 8-Q300/400*. The data assessment was accomplished over three exposure periods; February 2007, April/May 2007 and July/August/September 2007. After each period, the dosemeters were analysed and thereafter prepared for the next measurement circle. Including the calibration of the detectors, more than 1600 individual thermoluminescence measurements were performed. The measurement results were compared to doses, calculated with CARI 6 (see Chapter 6). The entire assessment period was at the end of the 23rd solar-cycle. Measurement data of the proton-telescope on board of the *Geostationary Operational Environmental Satellite 11* (GOES 11) showed no significant solar particle event within the whole assessment period, which corresponds to the count rate of terrestrial neutron monitors. Hence, an effect on the accumulated doses through solar events can be disregarded.

5.2 Dosemeter Preparation and Readout

The dosemeter preparation and readout was performed according to well-established procedures at the *Institute of Atomic and Subatomic Physics* of the *Vienna University of Technology*. [75] Before each exposure, the LiF:Mg,Ti (TLD-600/700) extruded chips of size 6.4 x 6.4 x 0.89 mm^3 obtained from a single TLD-600 batch and a single TLD-700 batch, were annealed according to a well-defined protocol at 400 °C for 1 h in air, followed by slow cooling to room temperature ~24 h in the oven. The CaF_2:Tm (TLD-300) single crystals of size 3.2 x 3.2 x 0.89 mm^3 – also obtained from one single batch – were annealed at 400 °C for 1.5 h in air, followed by the same cooling procedure. [75] Glow curves were readout by contact heating on a *Nikrothal 80* austenitic alloy planchet from room temperature to a maximum temperature of 400 °C at a linear heating rate $\beta = 5\ °C\ s^{-1}$. To minimize spurious chemiluminescence and triboluminescence, the measurement chamber was first evacuated and during readout flooded with ultra-poor (5.0) dry N_2 gas. The in-house developed reader employed the photon counting technique using a *Thorn EMI 9635 QB photomultiplier* (thorn EMI Gencom, Inc., Fairfield. NJ, USA) with a bialkali photocathode [74]). [75] For TLD-600/700 readouts an infrared filter was attached between the photomultiplier and the dosemeters to reduce black body radiation from incandescence. TLD-300 dosemeters have a relevant TL signal at the infrared range, and therefore, no infrared filter was used for them. General background subtraction was achieved by an exponential fit with constant offset. This method proved to be superior to manual analysis in which the background would be estimated by a consecutive second readout. [75]

5.3 Data Acquisition

The experimental data acquisition was accomplished with forty DOSFLIP dosemeter packages (Figure 5-1). Each contained three to four TLD-600, three to four TLD-700 dosemeters and two to four TLD-300 dosemeters. Pilots of Tyrolean Airways carried these DOSFLIP packages during their normal work-schedule. In order to estimate the background doses, it was necessary to specify the exact time between initial annealing and readout of each dosemeter. The data from flight logbooks were used to improve the background subtraction due to precise determination of airborne-time. The typical time that is recorded in the pilot logbook is the block time, which is the time between *block off* – when an aircraft starts to move or be moved – and *block on* – when an aircraft stops at its final parking position. The block time includes net flight time and taxi time. Pilots were asked to report the actual flight time, to improve the accuracy of airborne-time. For flights without documentation of the actual flight time, a total taxi time – incoming and outgoing – of 20 minutes was assumed for all international flights and 12 minutes for domestic flights. These

numbers are based on experience and a generally used for flight scheduling. Actual ground time is heavily dependent on several circumstances, such as the actual traffic situation at an airport, the distance to the active runway from the parking position and the weather situation.

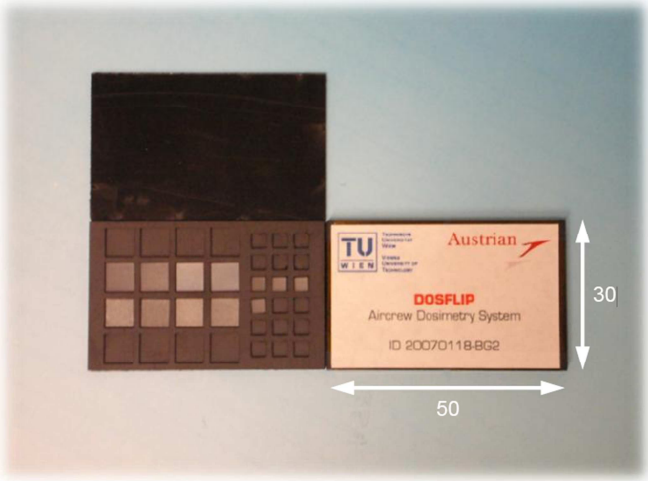

Figure 5-1: Thermoluminescence dosemeter system DOSFLIP (dimensions in [mm])

5.4 Calibration

For thermoluminescence (TL) measurements of the absorbed doses, it is necessary to calibrate the dosemeter crystals in a well-known radiation field. The initial calibration of the detectors was performed in a Cs-137 gamma radiation field (Table 5-1). The aim of such a calibration process is to calculate the *calibration factor* as a reference for subsequent measurements. This calibration factor is the quotient of a known calibration dose and its TL intensity at a particular temperature – or temperature interval – of a peak of the TL glow curve. For the calibration (and measurement) of the LiF dosemeters TLD-600 and TLD-700, the temperature interval [210°C - 230°C] (Figure 5-3 and Figure 5-2) containing the dominant peak 5 was chosen. The CaF_2 dosemeters were evaluated at peak 5 in an interval of [235°C - 255°C] (Figure 5-4) as well as at peak 3 in an interval of [160°C - 168°C] (Figure 5-5). To achieve maximum accuracy each dosemeter was calibrated individually and all phosphors were obtained from the same batch of the same manufacturer (Thermo Fisher Scientific). To minimise further statistical variations, the dosemeters were arranged according to their calibration factors so that each DOSFLIP package contained crystals with nearly equal calibration factors. The dosemeters were annealed/heated at the beginning of the measurement period to ensure that all electrons were released prior to the radiation exposure.

Table 5-1: Reference radiation fields used for calibrations

Dosmeter	Calibration source	Calibration dose	Infrared filter
TLD-600	Cs-137	11.66 mGy	Yes
TLD-700	Cs-137	9.76 mGy	Yes
TLD-300	Cs-137	2.59 mGy	No

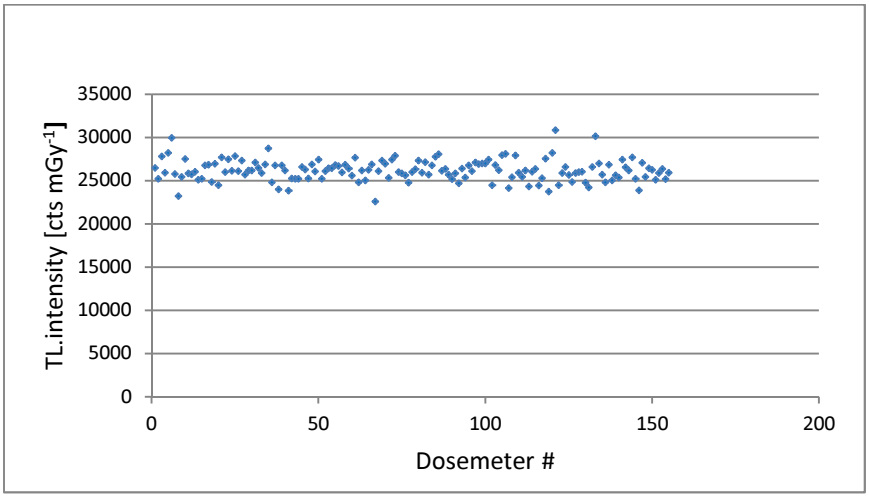

Figure 5-2: Calibration factors for TLD-600 dosemeters at peak 5 [210°C, 230°C]

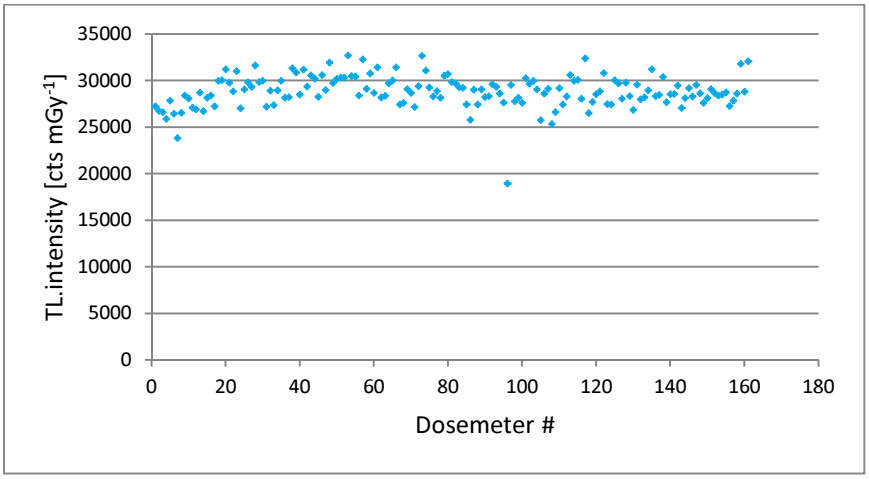

Figure 5-3: Calibration factor of TLD-700 dosemeters at peak 5 [210°C, 230°C]

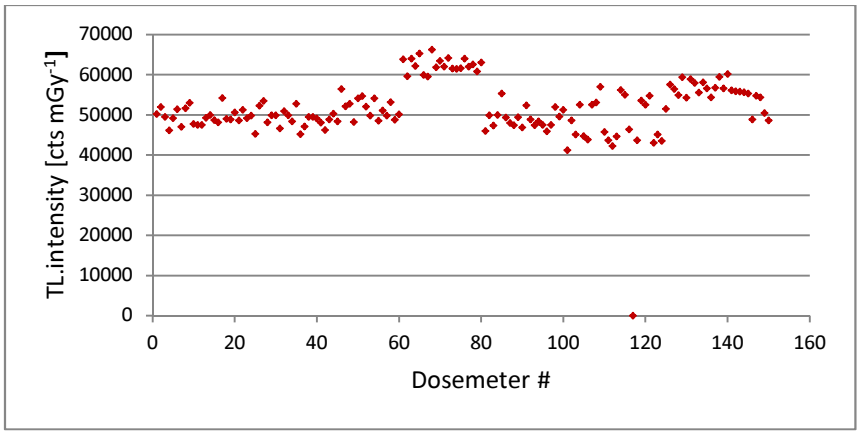

Figure 5-4: Calibration factor for TLD-300 dosemeters at peak 5 [235°C, 255°C]

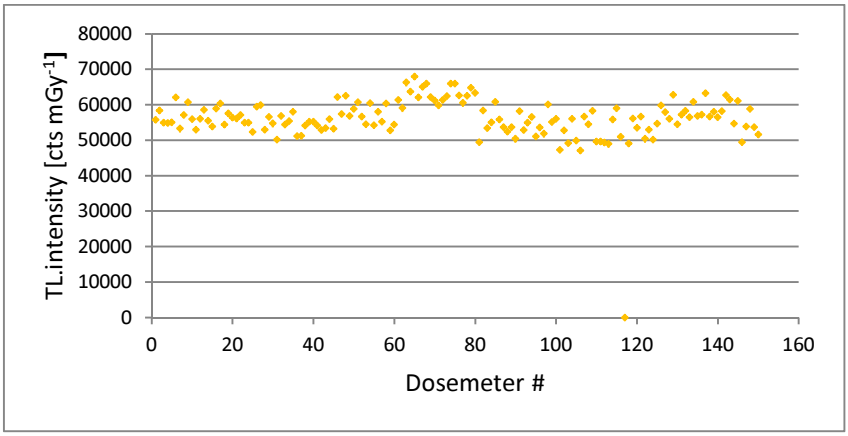

Figure 5-5: Calibration factors for TLD-300 dosemeters at peak 3 [160°C, 168°C]

5.5 Glow Curve Analysis

The glow curves have been analysed by computer program developed at the *Institute of Atomic and Subatomic Physics of the Vienna University of Technology*. Each glow curve was analysed separately. The glow curves have been smoothened by a 21-channel interpolation. The X-axis individual glow curves were shifted in such a way that the maximum of the analysed glow peak was always at the same position. The background-subtraction was performed by an exponential fit for black-body radiation with a constant offset for the electronic noise level of the environment. The absorbed dose was evaluated by thermoluminescence emission at peak 5 (and additionally at peak 3 for TLD-300 dosemeters). The measurement accuracy was improved by integrating the TL intensity in a certain integration interval around the peak maximum. Table 5-2 shows the position of the peak-maxima and the used integration intervals.

Table 5-2: Peak position and integration intervals of the analysed thermoluminescence glow curves

	Peak 5 [℃]	Integration interval [℃]	Peak 3 [℃]	Integration interval [℃]
TLD-600	220	[210, 230]		
TLD-700	220	[210, 230]		
TLD-300	245	[235, 255]	164	[160, 168]

5.6 Analysis and Calculation

5.6.1 Sparsely Ionizing Radiation

The non-neutron component was independently measured by both neutron-insensitive dosemeter types; TLD-700 and TLD-300. The ambient dose equivalent of the non-neutron component can be estimated in good approximation by multiplication of the measured dose with the appropriate radiation weighting factor as described in Chapter 3.1.2 . Hence, appropriate determination of the radiation weighting factor is essential. Under consideration of the intrinsic detector sensitivity for different particle types the fraction of neutron and neutron-equivalent high-energy protons can be estimated to 5 - 10% of the total TLD-700 signal. About 20% of the proton dose, this is 5 - 6% of the non-neutron dose, is caused by secondary particles of neutron-equivalent interactions. This contribution is also measured by the – separately determined – neutron dose. In order to determine the non-neutron dose $D_{non\text{-}neutron}$ without double-registration the measured absorbed dose D of the TLD-700 dosemeters has to multiplied by a correction factor of 0.92. [79]

$$D_{non-neutron} = 0.92 \cdot D \tag{5.1}$$

The effective dose $E_{non\text{-}neuron}$ of the non-neutron component can be calculated by application of radiation weighting factors. Protons with energies of more than 5 MeV have a radiation weighting factor of 5 (see Table 3-1), which leads to the following equation.

$$E_{non-neutron} = 0.92 \cdot D \cdot \left(\left(1 - f_p\right) + 5 f_p\right) \tag{5.2}$$

f_p is the contribution of protons with energies > 5 MeV within the total non-neutron component. For cosmic radiation at cruise flight altitudes a proton contribution of 18% was determined and published by Bilski et al., 2004 [78]. Considering the 20% fraction of neutron-equivalent high-energy protons, the factor of high-energy protons f_p and the effective dose of the non-neutron component $E_{non\text{-}neutron}$ can be calculated.

$$f_{proton} = 0.18 - \left(0.18 \cdot 0.2\right) = 0.144 \tag{5.3}$$

$$E_{non-neutron} = 0.92 \cdot D \cdot \left(\left(1 - 0.144\right) + 5 \cdot 0.144\right) \approx 1.45 \cdot D \tag{5.4}$$

5.6.2 Neutrons

The dose from the indirectly ionization neutron component was determined separately by means of the extended pair method (Chapter 4.5). Therefore, the different sensitivities to thermal neutrons of the lithium fluoride phosphors TLD-600 and TLD-700 are exploited. To provide appropriate calibration conditions for flight dosimetry, the calibration was performed in the CERN-EU High-Energy Reference Field (CERF) in terms of ambient dose equivalent H*(10). [76] This reference field was established from the *European Organization for Nuclear Research (CERN)*, and is characterized as follows: “A reference facility for the calibration and intercomparison of active and passive detectors in broad neutron fields has been available at CERN since 1992. A positively charged hadron beam (a mixture of protons and pions) with momentum of 120 GeV/c hits a copper target, 50 cm thick and 7 cm in diameter. The secondary particles produced in the interaction traverse a shield, at 90° with respect to the direction of the incoming beam, made of either 80 to 160 cm of concrete or 40 cm of iron. Behind the iron shield, the resulting neutron spectrum has a maximum at about 1 MeV, with an additional high-energy component. Behind the 80 cm concrete shield, the neutron spectrum has a second pronounced maximum at about 70 MeV and resembles the high-energy component of the radiation field created by cosmic rays at commercial flight altitudes.” [77]

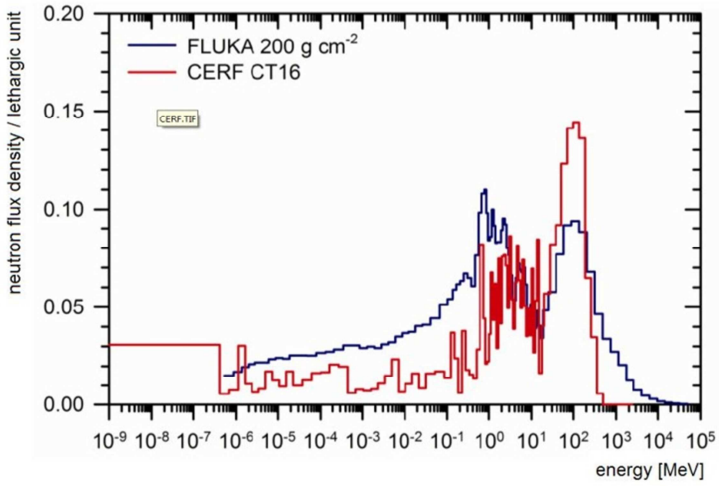

Figure 5-6: Neutron spectrum of the CERN reference field behind the concrete shield compared to a calculation of the atmospheric neutron spectrum in 11.9 km height by the Monte Carlo simulation FLUKA [86]

This $H^*(10)_{neutron}$ *ambient equivalent dose* comprises not only the neutron dose but also a fraction of high-energy protons with energies > 5 GeV. These protons interact with nuclei equivalent to neutrons and therefore cannot be distinguished from them. To calculate the *effective neutron dose* $E_{neutron}$ conversion factors for the neutron spectrum at cruising flight level have to established. In this thesis, the following conversion-factors (published from Bilski et al., 2004 [78]) were used:

$$H^*(10)_{neutron} / \Phi = 242\ pSv\,cm^{-2} \tag{5.5}$$

$$E_{neutron} / \Phi = 207\ pSv\,cm^{-2} \tag{5.6}$$

Hence, the ratio between H*(10) and the effective dose from neutrons is:

$$H^*(10)_{neutron} / E_{neutron} = 1.17 \tag{5.7}$$

5.6.3 X-ray Scans

The DOSFLIP dosemeters were carried either on the pilot or in the pilot's briefcase. In the second case the dosemeters have been exposed to the X-rays at airport security stations. Pilots could choose were they carried the dosemeters as long as they documented how many times they sent the detectors through the X-ray scan. The effect of the X-ray scans at the airport security stations was evaluated by dedicated reference measurements. Therefore, two DOSFLIP dosemeter packages, each containing four TLD-700 dosemeters were used to determine the radiation effect of X-ray scans. Both packages were sent through the X-ray device, one of them was put into a briefcase to simulate the usual condition of dosemeters being kept in a pilot's case. This procedure was repeated thirty times in succession at a security station of the Vienna airport. A summary of the measurement results is given in Table 5-3. The higher doses measured by unpacked dosemeters showed an absorbed dose of 8.3(1) µGy per scan cycle, while the dosemeters located in a briefcase had an absorbed dose of 4.5(2) µGy per scan.

Table 5-3: Measurement of 30 X-ray scans with TLD-700 dosemeters

TLD-700	Absorbed dose (σ) [µGy]	σ [%]	Absorbed dose per scan [µGy]
DOSFLIP	252(3)	1.34	8.3(1)
DOSFLIP in briefcase	137(7)	5.28	4.5(2)

5.6.4 Error Estimation

To minimize the error of measurement and to ensure a homogeneous detector characteristics all dosemeters of a specific type (e.g. TLD-600) have been obtained from a single batch. Furthermore,

dosemeters were sorted after the initial calibration according to their relative sensitivities. The uncertainty of the measurement is given by the standard deviation:

$$\sigma = \sqrt{s^2} = \sqrt{\frac{1}{n}\sum_{i=1}^{n}(x_i - \bar{x})^2} = \sqrt{\frac{1}{n}\left(\sum_{i=1}^{n} x_i^2\right) - \bar{x}^2} \tag{5.8}$$

Continuing evaluations accounted for further factors, like the environmental radiation and the dose through X-rays scans. To estimate the overall uncertainty of all these factors and the standard deviation is calculated by the error propagation. For example, the standard deviation of a function *u* containing the variables *x*, *y* is defined as follows:

$$\sigma_u = \sqrt{\sigma_x^2\left(\frac{\partial u}{\partial x}\right)^2 + \sigma_y^2\left(\frac{\partial u}{\partial y}\right)^2} \tag{5.9}$$

5.7 Exemplary Evaluation

For data assessment of a DOSFLIP package, each individual crystal was readout and analysed separately. Table 5-4 shows an exemplary evaluation of a DOSFLIP package containing four TLD-600 and four TLD-700 phosphors.

Table 5-4: Exemplary evaluation of a DOSFLIP package containing four TLD-600 and four TLD-700 dosemeters.

Data sheet DOSFLIP ID 20070118-02					
TLD-600 ID 20070118-02					
Chip #	Peak 5 [cts]	Peak 5 Cal [cts]	Dose Cal [mGy]	Cal Factor [cts/mGy]	Dose [µGy]
38	5825	279580	11.7	23978	243
92	6124	287886	11.7	24690	248
113	5930	283518	11.7	24315	244
18	6399	289415	11.7	24821	258
Mean Value	6070	285100	11.7	24451	248
σ	218	3852	0	330(1.4%)	5.8(2.4%)
TLD-700 ID 20070118-02					
Chip #	Peak 5 [cts]	Peak 5 Cal [cts]	Dose Cal [mGy]	Cal Factor [cts/mGy]	Dose [µGy]
12	4686	262645	9.8	26910	174
6	4321	257945	9.8	26429	163
3	4560	259459	9.8	26584	172
118	4092	58508	9.8	6487	154
Mean Value	4415	259639	9.8	26602	166
σ	228	1818	0	186 (0.7%)	7.7 (4.6%)

Data sheet DOSFLIP ID 20070118-02			
Additional Input Data			
Annealing	18.01.2007	BG dose	72 µGy
Readout	12.03.2007	X-ray scans	0
Flight Time	89.5 h	Dose/scan	4.47 µGy
Results			
Dose		Standard Deviation	
BG	85.14 µGy	σ(BG)	4.26 Gy
D	80.77 µGy	σ(D)	8.77 µGy
Etot	209.24 µSv	σ(Etot)	18.93 µSv
H*(10)neutron	78.73 µSv	σ(H*(10)neutron)	11.99 µSv

The mean values of the absorbed doses of the TLD-600($D_{TLD\text{-}600}$) and TLD-700($D_{TLD\text{-}700}$) measurements are the basis for further calculations; the absorbed energy dose, the ambient dose equivalent, total effective dose and their respective standard deviations.

The dose of *the environmental background radiation BG* was calculated by multiplying the time on ground with the estimated *environmental background dose rate* BG_{ground}. The time on ground is defined as the he exact time between *annealing (ANN)* and *readout (ROUT)* minus *flight time (FT).* The average environmental dose rate was estimated with 0.05 µGy/h[12], with an assumed error of 5 %. Additionally the doses of possible security X-ray scans were added. The contribution of X-ray doses was determined according to the X-ray reference dose measurements (see Chapter 5.6.3). Hence, the equation for the environmental background radiation dose is:

$$BG = \left(\left(ANN - ROUT\right) - FT\right) * BG_{ground} + Xray_{scan} \tag{5.10}$$

The *absorbed energy doses due to cosmic radiation* D_{CR} is the *mean value of (the four) TLD-700 measurements* $D_{TLD\text{-}700}$ without the environmental background dose *BG*.

$$D_{CR} = \overline{D}_{TLD-700} - BG \tag{5.11}$$

The *neutron component of the measurement signal* $\Lambda_{neutron}$ is calculated by comparison of *the TLD-600 signal* $\Lambda_{TLD\text{-}600}$ and the *TLD-700 signal* $\Lambda_{TLD\text{-}700}$ in dependence on their respective calibration factors $\kappa_{TLD\text{-}700}$ and $\kappa_{TLD\text{-}600}$.

$$\Lambda_{neutron} = \Lambda_{TLD-600} - \frac{\kappa_{TLD-700}}{\kappa_{TLD-600}} \Lambda_{TLD-700}$$

To provide appropriate calibration conditions for flight dosimetry, the calibration was performed in the CERN-EU High-Energy Reference Field (CERF) in terms of ambient dose equivalent H*(10). The differences between the measurement and calibrations conditions were considered by applying

[12] Corresponding to the mean value of the environmental dose rate for the towns Schwechat, Fischamend and Vienna published in the Austrian radiation atlas.

an additional factor, as described by Hajek 2002. [76] In this study, a factor of 1.3474 [cts/µSv] allows a direct calculation of the *ambient dose equivalent of the neutron component H*(10)$_{neutron}$* using the means absorbed doses of TLD-600/700, their respective calibration factors κ and two additional filter factors (19.0904 and 19.1534) considering the used NG3 optical natural glass filter.

$$H^*(10)_{neutron} = \frac{\overline{D}_{TLD-600}}{19.0904} - \frac{\overline{D}_{TLD-700}/19.1534}{\kappa_{TLD-700}/\kappa_{TLD-600}} \quad (5.12)$$

The *total effective dose* E_{tot} can be calculated by applying equations (5.4) and (5.7).

$$E_{tot} = E_{neutron} + E_{non.neutron} \quad (5.13)$$

The standard deviations of the calculated doses were calculated by error propagation of the respective measurement values.

The TLD-300 crystals were analysed in the same way as the lithium fluoride crystals. The calcium fluoride crystals were evaluated at peak 3 and peak 5. Peak 3 has a higher intensity but is affected by stronger fading. Due to the low neutron-sensitivity of TLD-300 (Table 4-2) the measured absorbed dose $D_{non\text{-}neutron}$ is directly comparable with the neutron-insensitive TLD-700 measurements. A differentiated analysis of the neutron and non-neutron share of the absorbed doses was not possible because of the fact that neutron sensitive reference dosemeters were not available for TLD-300.

Table 5-5: Exemplary evaluation of four TLD-300 dosemeters of a DOSFLIP package

Data sheet DOSFLIP TLD-300 ID 20070118-02					
TLD-300 ID 20070118-02					
Chip #	Peak 5 [cts]	Peak 5 Cal [cts]	Dose Cal [mGy]	Cal Factor [cts/mGy]	Dose [µGy]
106	8453	113891	2.6	43973	192
103	8304	116585	2.6	45014	184
124	8267	116001	2.6	44788	185
113	8695	116937	2.6	45149	193
Mean Value	8430	115854	2.6	44731	188
σ	168	1181	0	456 (1.0%)	3.9(2.1%)
TLD-300 ID 20070118-02					
Chip #	Peak 3 [cts]	Peak 3 Cal [cts]	Dose Cal [mGy]	Cal Factor [cts/mGy]	Dose [µGy]
106	8691	122060	2.6	47127	184
103	8708	127435	2.6	49203	177
124	9426	130168	2.6	50258	188
113	9054	127024	2.6	49044	185
Mean Value	8970	126672	2.6	48908	183
σ	301	2924	0	1129 (2.3%)	3.9 (2.1%)

Data sheet DOSFLIP TLD-300 ID 20070118-02			
Additional Input Data			
Annealing	18.01.2007	BG dose	72 µGy
Readout	12.03.2007	X-ray scans	0
Flight Time	89.5 h	Dose/scan	n/a
Results			
Dose		Standard Deviation	
BG	85.14 µGy	σ(BG)	4.26 µGy
D(Peak5)	102.76 µGy	σ(D(Peak5)	4.93 µGy
D(Peak5)	97.46 µGy	σ(D(Peak3)	4.81 µGy

5.8 Measurement Results

The dosemeters were used in three long-term measurement campaigns. The first measurement period was in February 2007, the second from to May 2007, and the third during the summer months July, August, and September 2007. Although the first DOSFLIP packages were assigned to the pilots simultaneously, the different measurement periods of individual dosemeter packages differ due to individual duty schedules leading to different returns dates of the dosemeters. Therefore, the exact time between annealing and readout was considered separately for each DOSFLIP package to determine the accurate background radiation within the evaluation period.

5.8.1 TLD-600 / TLD-700

The evaluation shows that the neutron component has a high share of the total absorbed energy dose, which was expected due to the high neutron contribution in the cosmic radiation at cruising flight altitude. Due to lower flight altitudes of the turboprop-driven aircraft *Bombardier Dash 8-Q300/400* the average absorbed doses from cosmic radiation were significantly lower than on flights with jet-driven aircraft. Therefore, the environmental background dose had more influence on the total measured dose. For reliable data discrimination, the cosmic-ray induced signal has to be three higher than the standard deviation of the accumulated background dose.

Table 5-6: Results of the TLD-600/700 measurements in February 2007

Dosemeter	Fleet	Flight time [h]	Dnon-neutron [µGy]	H*(10)neutron [µSv]	Etot [µSv]
3	CRJ	72.3	51.3(88)	59.6(85)	132.4(161)
5	CRJ	39.2	18.8(73)	37.8(114)	71.9(171)
6	CRJ	64.1	62.5(63)	44.6(93)	142.9(142)
7	CRJ	39.9	25.2(51)	38.3(19)	81.3(77)
14	CRJ	71.2	83.2(195)	69.7(94)	190.4(442)
16	CRJ	27.5	16.7(67)	26.8(70)	55.6(127)

Dosemeter	Fleet	Flight time [h]	Dnon-neutron [µGy]	H*(10)neutron [µSv]	Etot [µSv]
18	CRJ	67.8	48.4(545)	49.0(68)	127.6(794)
19	CRJ	27.2	27.8(232)	37.3(52)	83.9(341)
20	CRJ	67.8	76.4(304)	58.1(34)	178.9(442)
21	CRJ	152.4	184.2(251)	112.6(154)	398.8(406)
22	CRJ	37.8	29.2(48)	22.1(43)	68.2(85)
23	CRJ	62.0	52.0(203)	66.4(49)	153.2(300)
25	CRJ	61.9	71.8(74)	60.8(92)	175.2(151)
28	CRJ	55.0	58.2(59)	56.2(70)	150.2(118)
29	CRJ	28.9	17.3(61)	36.4(77)	67.7(126)
34	CRJ	64.2	44.0(52)	69.1(74)	144.6(115)
36	CRJ	63.1	57.8(64)	51.6(65)	144.2(120)
37	CRJ	41.8	23.6(245)	45.2(32)	87.1(357)
1	F70/100	87.7	168.4(184)	54.3(184)	307.6(343)
2	F70/100	89.5	80.8(88)	78.7(120)	209.2(189)
4	F70/100	41.6	44.5(78)	42.9(135)	114.8(193)
9	F70/100	44.3	68.3(236)	64.3(128)	174.3(343)
10	F70/100	45.9	20.8(48)	49.9(51)	76.8(92)
12	F70/100	67.8	149.6(169)	119.8(226)	330.9(360)
13	F70/100	60.5	53.3(50)	55.6(66)	142.4(106)
15	F70/100	47.1	34.1(51)	38.6(29)	94.7(81)
26	F70/100	59.7	63.5(63)	52.9(72)	154.0(125)
27	F70/100	75.4	56.8(256)	64.1(116)	157.4(395)
30	F70/100	130.4	155.8(83)	63.9(135)	300.7(299)
31	F70/100	85.1	69.2(120)	79.1(187)	192.8(279)
32	F70/100	80.2	91.4(68)	44.9(55)	185.2(118)
33	F70/100	69.8	71.8(293)	27.4(65)	136.1(431)
35	F70/100	110.3	107.9(186)	93.8(203)	266.1(360)
38	F70/100	58.9	54.7(87)	89.6(87)	184.1(162)
8	D8	60.2	14.2(67)	20.3(84)	44.4(138)
11	D8	37.7	33.7(224)	40.3(133)	95.9(360)
17	D8	37.7	12.4(261)	26.5(56)	48.9(385)
39	D8	17.3	16.4(100)	27.9(132)	56.5(212)
40	D8	41.6	17.2(180)	12.1(68)	39.1(273)

Table 5-7: Results of the TLD-600/700 measurements in April/May 2007

Dosemeter	Fleet	Flight time [h]	Dnon-neutron [µGy]	H*(10)neutron [µSv]	Etot [µSv]
3	CRJ	78.4	72.1(77)	75.0(71)	192.3(139)
5	CRJ	64.0	52.5(106)	53.0(75)	139.2(171)
6	CRJ	95.7	13.7(97)	85.7(141)	292.7(217)
7	CRJ	48.8	59.4(79)	55.1(65)	150.6(138)
14	CRJ	97.9	104.6(291)	89.0(113)	255.9(442)
16	CRJ	109.4	116.1(155)	118.6(202)	307.0(327)
18	CRJ	44.5	49.8(211)	48.8(134)	129.3(344)
19	CRJ	83.5	75.3(205)	77.7(177)	200.0(363)
20	CRJ	80.5	101.7(439)	70.2(140)	229.5(657)
23	CRJ	46.1	41.7(178)	53.2(113)	122.7(291)
25	CRJ	134.3	185.4(72)	182.3(96)	482.1(153)
28	CRJ	64.2	114.6(103)	75.5(145)	254.5(225)
29	CRJ	90.9	79.2(101)	94.8(152)	225.9(230)
34	CRJ	98.2	87.0(120)	127.8(217)	275.6(308)
36	CRJ	96.3	133.7(249)	111.7(260)	324.6(472)
37	CRJ	78.1	180.3(160)	75.3(102)	359.5(260)
2	F70/100	94.5	113.5(91)	133.3(660)	320.6(784)
4	F70/100	34.6	34.6(81)	41.8(122)	99.0(185)
9	F70/100	112.0	169.6(507)	109.8(139)	374.3(752)
12	F70/100	75.5	138.3(136)	102.3(233)	320.2(341)
13	F70/100	95.0	167.0(92)	176.6(91)	343.6(130)
22	F70/100	88.4	70.5(346)	100.5(133)	219.9(516)
26	F70/100	140.9	252.1(166)	164.9(233)	558.5(363)
27	F70/100	56.6	63.0(135)	71.0(106)	174.4(232)
30	F70/100	61.8	89.2(232)	77.3(149)	219.8(380)
32	F70/100	42.5	91.1(174)	47.5(74)	187.7(267)
33	F70/100	95.3	165.0(203)	88.4(79)	342.6(309)
38	F70/100	95.7	66.4(98)	120.2(116)	236.9(197)
8	D8	60.9	37.8(71)	51.4(83)	115.0(142)
11	D8	99.8	77.0(434)	58.6(230)	180.2(684)
17	D8	109.2	152.3(347)	103.2(245)	341.6(578)
39	D8	67.0	22.5(71)	59.4(91)	102.2(148)
40	D8	94.2	41.9(98)	48.5(110)	117.5(192)

Table 5-8: Results of the TLD-600/700 measurements in July/August/September

Dosemeter	Fleet	Flight time [h]	Dnon-neutron [µGy]	H*(10)neutron [µSv]	Etot [µSv]
3	CRJ	82.1	98.4(167)	76.8(165)	232.5(309)
5	CRJ	53.3	27.5(117)	60.1(122)	100.0(209)
6	CRJ	40.2	35.9(122)	44.4(115)	104.0(222)
7	CRJ	140.6	154.6(162)	147.7(140)	397.0(287)
14	CRJ	140.2	124.0(533)	103.7(308)	301.1(853)
16	CRJ	107.2	103.2(181)	102.9(245)	270.1(389)
18	CRJ	128.3	125.0(969)	106.5(159)	305.8(1417)
20	CRJ	40.0	80.2(149)	40.6(98)	156.8(237)
23	CRJ	22.1	20.9(85)	31.1(95)	61.4(155)
25	CRJ	42.8	64.7(86)	60.5(74)	154.3(145)
28	CRJ	78.9	101.8(462)	83.7(250)	245.5(731)
29	CRJ	55.7	39.2(118)	68.4(148)	136.9(243)
34	CRJ	93.4	73.9(131)	99.3(230)	223.4(329)
1	F70/100	139.0	78.4(324)	79.9(175)	207.2(512)
4	F70/100	66.8	76.9(146)	80.3(162)	205.5(284)
9	F70/100	112.5	150.1(607)	150.2(220)	393.3(916)
13	F70/100	89.1	109.4(326)	122.0(283)	231.4(432)
30	F70/100	87.9	116.7(243)	87.0(173)	256.3(392)
32	F70/100	75.8	146.6(439)	109.4(155)	340.5(663)
38	F70/100	75.8	67.4(134)	97.3(142)	211.6(256)
8	D8	124.9	23.7(151)	66.4(207)	112.0(326)
40	D8	76.1	75.7(521)	36.8(121)	152.8(769)

The statistical accuracy of the measurements is indirectly proportional to the accumulated dose, which is shown in Figure 5-7. The average standard deviation of the effective doses measured by dosemeters within the same DOSFLIP package is approximately 16%.

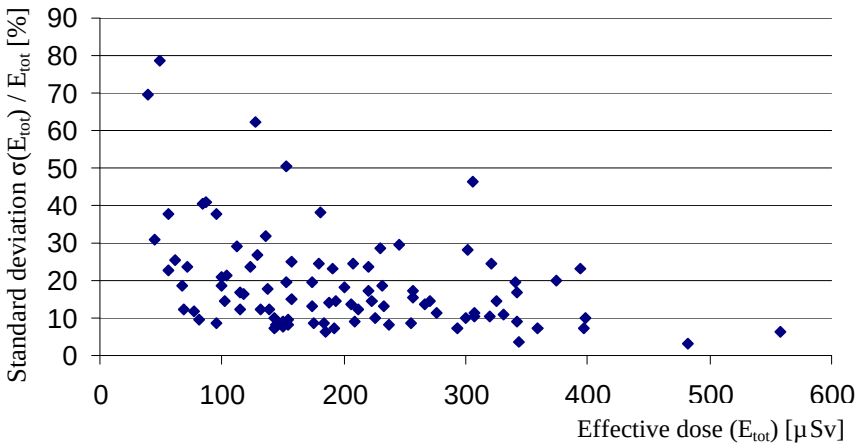

Figure 5-7: Standard deviation of the effective dose (measured by TLD600/700 dosemeters) of each DOSFLIP package as a function of its accumulated effective dose

5.8.2 TLD-300

The data from the calcium fluoride TLD-300 dosemeters were assessed for the first (Table 5-9) and the third (Table 5-10) evaluation period. They were carried in the DOSFLIP dosemeter packages in addition to the TLD-600/700 dosemeters. Peak 3 and peak 5 of the thermoluminescence spectrum were used for data analysis. A clear difference of the peak 3 and peak 5 measurements could was observed, which was expected due to the already mentioned fading of peak 3. This effect was particularly noticeable for dosemeters that were returned with a significant delay. In the first –on average one month lasting –period, the evaluation of peak 3 showed on average a 8.5 % lower measurement dose than the evaluation of peak 5. In the later – on average three month lasting – period, the evaluation of peak 3 showed on average a 13.5 % lower measurement dose than the evaluation of peak 5. Due to the high X-ray sensitivity of TLD-300 (see Figure 4-4), X-ray radiation of security scans could generated signals higher than the measured cosmic radiation. Therefore, the dosemeters sent through the X-ray scans were evaluated separately. Pilots could choose to carry the dosemeter package either on the person (e.g. in a shirt pocket) or in their pilot's suitcase. Only DOSFLIP packages carried in the pilot's suitcase were sent through X-ray security scanners. The lack of X-ray reference measurements with TLD-300 dosemeters and the overresponse of TLD-300 dosemeters at X-ray energies with respect to Cs-137 made it impossible to evaluate these dosemeters in a statistically relevant manner.

Table 5-9: TLD-300 measurements in February 2007 compared to TLD-700 measurements

Dosemeter #	Fleet	X-ray	FT [h]	DTLD-700(σ) [µGy]	DTLD-300(P5)(σ) [µGy]	DTLD-300(P3)(σ) [µGy]
3	CRJ	N	72.3	143.4(70)	163.1(23)	157.1(21)
6	CRJ	N	64.1	151.2(44)	204.8(48)	177.9(33)
7	CRJ	N	39.9	117.6(18)	148.9(37)	132.0(34)
16	CRJ	N	27.5	109.8(48)	123.2(81)	107.2(46)
22	CRJ	N	37.8	121.5(11)	155.1(30)	139.0(54)
29	CRJ	N	28.9	112.0(38)	115.6(25)	111.4(33)
34	CRJ	N	64.2	136.1(25)	143.7(24)	135.0(7)
37	CRJ	N	41.8	160.9(126)	161.0(44)	148.0(45)
2	F70/100	N	89.5	165.9(77)	188.5(39)	183.4(39)
4	F70/100	N	41.6	134.8(63)	164.1(117)	153.9(69)
10	F70/100	N	45.9	110.8(18)	125.6(36)	116.7(31)
12	F70/100	N	67.8	290.2(151)	330.8(88)	299.2(140)
13	F70/100	N	60.5	144.0(22)	150.3(49)	141.7(55)
15	F70/100	N	47.1	125.8(23)	125.6(26)	119.4(35)
31	F70/100	N	85.1	222.4(92)	238.1(37)	216.3(18)
38	F70/100	N	58.9	147.2(73)	175.0(307)	149.3(84)
8	D8	N	60.2	103.2(50)	114.5(19)	106.8(21)
39	D8	N	17.3	172.4(63)	194.1(32)	167.9(15)
5	CRJ	Y	39.2	116.8(13)	206.0(13)	175.8(18)
14	CRJ	Y	71.2	216.2(60)	543.5(259)	415.5(177)
19	CRJ	Y	27.2	150.9(29)	373.6(57)	281.2(56)
20	CRJ	Y	67.8	206.6(16)	431.1(967)	384.3(162)
23	CRJ	Y	62.0	168.6(35)	335.0(267)	272.8(131)
36	CRJ	Y	63.1	185.5(6)	413.3(54)	331.3(75)
9	F70/100	Y	44.3	186.4(97)	308.0(110)	254.2(55)
27	F70/100	Y	75.6	236.9(96)	417.2(41)	339.3(46)
30	F70/100	Y	130.4	305.5(37)	717.6(138)	538.6(164)
33	F70/100	Y	69.8	236.1(19)	383.8(87)	321.7(30)
17	D8	Y	37.7	138.7(34)	315.4(39)	251.4(52)

Table 5-10: TLD-300 measurements in July/August/September 2007 compared to TLD700 measurements

Dosemeter #	Fleet	X-ray	FT [h]	DTLD-700(σ) [µGy]	DTLD-300(P5)(σ) [µGy]	DTLD-300(P3)(σ) [µGy]
3	CRJ	N	82.1	292.9(135)	380.8(72)	337.3(60)
6	CRJ	N	40.2	229.2(74)	335.7(50)	288.8(104)
7	CRJ	N	140.6	346.7(131)	491.1(223)	399.1(153)
16	CRJ	N	107.2	297.7(153)	326.6(179)	294.5(173)
25	CRJ	N	42.8	196.4(56)	212.9(52)	193.6(40)
29	CRJ	N	55.7	249.4(53)	271.6(135)	244.0(95)
34	CRJ	N	93.4	289.5(69)	381.9(93)	317.1(104)
4	F70/100	N	66.8	272.6(109)	317.6(44)	280.4(26)
12	F70/100	N	40.0	157.0(26)	221.9(66)	188.9(44)
38	F70/100	N	75.8	276.2(85)	295.8(158)	253.7(94)
8	D8	N	124.9	216.9(116)	264.5(123)	225.7(88)
5	CRJ	Y	53.3	228.6(59)	442.7(70)	355.3(49)
14	CRJ	Y	140.2	410.1(233)	781.7(1296)	618.0(363)
18	CRJ	Y	128.3	458.0(80)	988.0(387)	894.7(239)
20	CRJ	Y	40.0	238.1(29)	528.2(229)	396.4(129)
23	CRJ	Y	22.1	164.1(14)	237.1(66)	199.1(45)
28	CRJ	Y	78.9	370.4(10)	749.0(116)	561.9(97)
1	F70/100	Y	139.0	307.9(101)	722.6(148)	567.1(77)
9	F70/100	Y	112.5	422.2(127)	1006.1(348)	728.2(282)
13	F70/100	Y	89.1	365.1(82)	811.2(306)	597.8(190)
30	F70/100	Y	87.9	291.2(42)	629.8(419)	470.7(264)
32	F70/100	Y	75.8	411.4(76)	795.3(206)	589.1(161)

The differences of TLD-300 measurements that included X-ray scans and TLD-300 measurements that excluded X-ray scans and TLD-700 measurements are shown in Table 5-11, Table 5-12. The absorbed doses from TLD-300 measurements including X-ray scans were expected high due to their high response for typical X-ray radiation. The signal had also a very high deviation, which can be explained by the unsteady course of the TLD-300 sensitivity at typical X-ray energies. Hence, for further data treatment, only TLD-300 crystals that were never subject of security scans are considered.

Table 5-11: Average TLD-300/TLD-700 ratio in the first measurement period

TLD-300(Peak5)/TLD700		σ
Without X-ray scans	1.134	0.095
Including X-ray scans	1.487	0.497

TLD-300(Peak3)/TLD700		σ
Without X-ray scans	1.038	0.074
Including X-ray scans	1.275	0.333

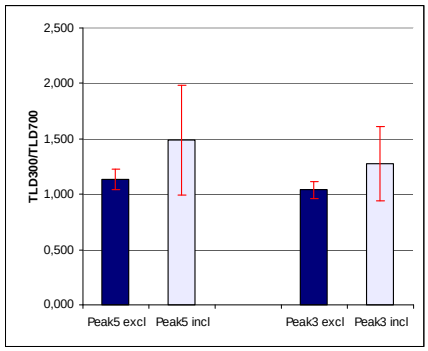

Table 5-12: Average TLD-300/TLD-700 ratio in the third measurement period

TLD-300(Peak5)/TLD700		σ
Without X-ray scans	1.240	0.143
Including X-ray scans	1.629	0.440

TLD-300(Peak3)/TLD700		σ
Without X-ray scans	1.073	0.102
Including X-ray scans	1.308	0.289

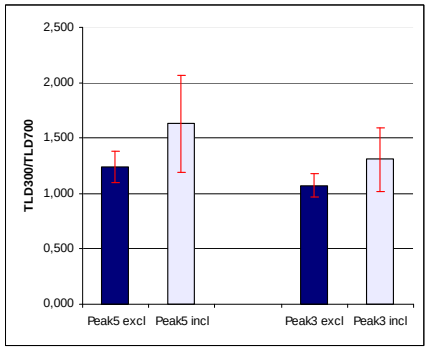

5.9 Comparison of TLD-300 and TLD-700

TLD-300 and TLD-700 dosemeters can be compared directly, because of their similar very low neutron sensitivity and similar TL measurement characteristics for cosmic radiation. Both dosemeter types have an energy independent response at energies between 300 keV and 3000 keV (see Figure 4-6). The most useful comparison is the direct comparison of TLD-700 measurements to TLD-300 measurements using peak 5, where the dosemeters have negligible fading. An accurate comparison to the TLD-300 peak 3 signal would require a quantitatively analysis of the peak 3 fading. In the first measurement period the total dose measured with TLD-300 was higher than the TLD-700 dose by a factor 1.13(95). In the third measurement period the TLD-300 measurement was higher by a factor 1.240(143). The higher dose response of TLD-300 dosemeters in comparison to TLD-700 dosemeters can be explained by their higher TL efficiency for protons, and hence a higher measurement signal due to the relative high proton share of the radiation field at flight altitudes (see Figure 2-7). Another possible reason could be that dosemeters that were not usually carried in a pilot's case could have been sent through security X-ray scans occasionally by accident.

A disadvantage of TLD-300 measurements is the lack of another calcium fluoride dosemeter, with comparable thermoluminescence properties but higher neutron sensitivity. Therefore, the extended pair method is not applicable and only the total absorbed dose can be assessed.

In general, TLD-300 dosemeters have good measurement accuracies and their high sensitivity is an advantage for measurements of lower radiation doses and shorter measurement periods. Hence, calcium fluoride dosemeters would be ideal for further aviation dosimetry measurements – especially for short range operation. It is highly recommended to ensure that TLD-300 dosemeters are never sent through X-ray scans in future assessments.

Chapter 6

Computational Methods

6.1 CARI 6

For computational assessment of the received doses the computer program *CARI 6* was used. CARI 6 was developed at the *FAA's Civil Aerospace Medical Institute* to calculate the effective dose from cosmic radiation received by an individual on-board an aircraft flying the shortest – geodesic – route between two airports. In addition, it can also calculate the effective dose rate from cosmic radiation at any specific location in the atmosphere for altitudes up to 60,000 feet. The program uses Monte Carlo codes to calculate the effective doses from cosmic radiation to an individual (based on an anthropomorphic phantom). The program takes into account the geographic coordinates of the departure and the arrival airports as well as the time of different flight phases, and changes in altitude during flight. These data have to be entered by the user to calculate the effective dose on a geodesic route (which is usually a good estimate of the actual flight route). Based on the date of the flight, appropriate databases are used to account for effects of changes in the Earth's magnetic field and solar activity on galactic radiation levels in the atmosphere by considering the heliocentric potential in the appropriate time period. LUIN99 and LUIN2000[13] are the transports codes used to generate the databases referenced by CARI 6, calculating the dose rate at individual locations that are further used for the route doses. These two codes are computationally similar but the calculation of the neutron dose. Especially the simulation of the neutron component is very difficult and affected by considerable errors. The estimation of the error of the simulation is rather

[13] LUIN99 / LUIN2000: LUIN is a high-energy transport code based on the Greens-function type solution. [84]

difficult. Different programs like CARI 6 or SIEVERT[14] can show a difference of up to 20% in effective dose, especially on flights at high geomagnetic latitude. Another source of uncertainty is that the accuracy strongly depends on the records and notations of the pilots. Direct assembly with flight data monitoring systems could improve the data assessment.

CARI 6 is one of the worldwide most used computer programs for assessment of radiation exposure of crew and has been certified by many national authorities as an appropriate tool for legal aircrew dosimetry requirements. Although the program is also certified for many nations of the European Union, Austria has not accredited this computer program by national law as a source for aircrew dosimetry.

6.2 Acquisition and Input

To calculate the dose on a particular flight the primary parameters are the geographic coordinates of the departure and the arrival airport, the flight altitude, the flight time including the time of the different flight phases – climb, cruise and descend –, the date of the flight and the value of the heliocentric potential in the particular month. Therefore, a major factor concerning the accuracy of the computed dose is the inherent dependence on the input flight data that are based on the records of participating flight crew members. Basically the records and copies of the flight logbooks were assumed to be correct and complete. More problematic was the documentation of additional data. Especially information like the net flight time, or the number of X-ray scans might not be exact. Additionally, it is very common for pilots to fly as “dead head crew”[15], on “stand by”[16] or on private flights. These flights are not regularly recorded in the flight logs, and all participating pilots were asked to log them separately. Although the majority of pilots did so, a certain amount of flights were identified as missing; e.g. a flight did not end at the same international destination where the next recorded flight started. Not all these flights could be identified, because for domestic re-positioning it was not always evident whether a change of location was dose by flight or ground transportation. CARI 6 has a database of the coordinates of world’s international airports. Smaller, regional airports

[14] The French Aviation Authorities have developed a system called SIEVERT, using calculation codes to monitor effective radiation doses. [87]

[15] A "dead head" is a crew member who is assigned to fly as a passenger on a specific flight (not an active flight crew member) so they can get to another city to work where they will pick up their assigned trip sequence.

[16] Flying on “standby” does not guarantee a seat on a particular flight. It is a cheap possibility for private travel on flights with free seat-capacities.

have been added in the database manually. The position of an airport and its altitude is defined by an airport (or aerodrome) reference point (ARP), the notional centre point of an airport.
Flight crew members were asked to log the actual flight time beside the block time. In a few cases, only the block time was available and it was therefore necessary to estimate the taxi-time[17]. In this cases, the taxi-time was assumed with a total duration of 20 minutes for incoming and outgoing taxi. Exceptions are made on very short flights – which are assumed as all domestic flights in Austria, and flights to *St.Gallen/Altenrhein*, *Belgrade* and *Zagreb*. These airports are significantly less occupied and therefore a shorter taxi time is likely. In some rare cases, the altitude was not documented. In these cases, the planned altitude (filed in the repetitive flight plan) was used in the program. For climb and descend generally 20 minutes were assumed, which could be confirmed to be a rather accurate estimation by notes of several participants. Exceptions were made for very short flights. Flights to *Graz* and *Linz* were calculated with an climb and a descend time of less than 10 Minutes and 15 minutes for flights to *Klagenfurt*, *Innsbruck*, *St.Gallen/Altenrhein*, *Belgrade* and *Zagreb*. These amendments are justifiable due to the lower flight levels that are used on this short flights. Generally, several circumstances can lead to significant deviation from planned vertical flight profiles. The most frequent reasons leading to variation of flight altitudes are the actual weather situation, air traffic requirements or prolonged flight in holding patterns.

6.3 Heliocentric Potential

CARI 6 can account changes in galactic radiation levels that occur with changes in solar activity. Therefore it is necessary to enter the appropriate heliocentric potential which provides an accurate model for solar activity. The heliocentric potential is the result of a steady-state solution of the diffusion equation of cosmic rays through the solar wind. The counting rate of any high-latitude, ground-level neutron monitor can be used to determine this potential, which will affect secondary return cosmic ray spectra in the atmosphere. These spectra are routinely used to determine the radiation dose rate to which aircrews are exposed. Flight doses for specific flight profiles normally change very little in a couple of months, so that it is sufficient to determine the potential on a monthly base. For the computational simulation of route doses in this study, data of the *Federal Aviation Administration (FAA)* for 2007 (Table 6-1, Figure 6-1) are used, that are published on the FAA website:

[17] “taxi-time“ is a time an aircraft spends on ground, beginning from its first movement from the initial parking position to the beginning of the takeoff-roll, as well as the time, from the end of the landing to the final parking position.

Table 6-1: Heliocentric potential 2007 [88]

Flights in the Month	Heliocentric Potential [MV]
January 2007 (01/2007)	374
February 2007 (02/2007)	379
March 2007 (03/2007)	340
April 2007 (04/2007)	314
May 2007 (05/2007)	305
June 2007 (06/2007)	300
July 2007 (07/2007)	319
August 2007 (08/2007)	312
September 2007 (09/2007)	300
October 2007 (10/2007)	291
November 2007 (11/2007)	307
December 2007 (12/2007)	287
2007	316

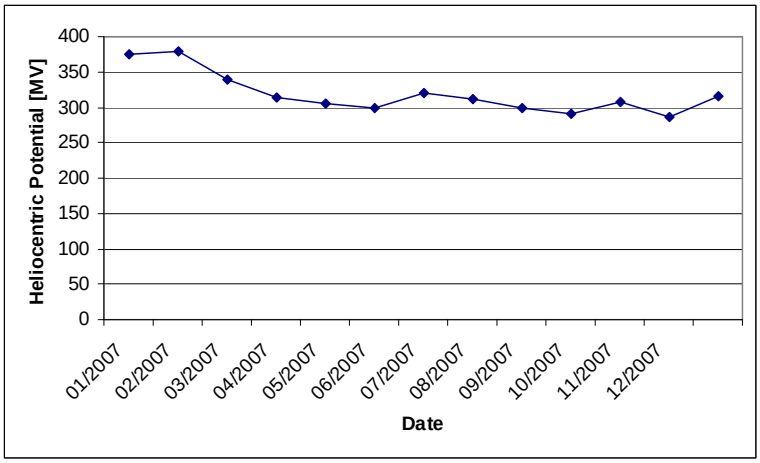

Figure 6-1: Course of the heliocentric potential 2007

6.4 Comparison with Experimental Measurements

The calculated doses of each flight of a crew member were summarised in the corresponding time period. The results were compared with the total effective dose measured with TLD-600/700 dosemeters. The results and their standard deviations are shown in Table 6-2 and Table 6-4.

Table 6-2: Comparison of calculated and measured dose in February 2007

#	Fleet	Flight time [h]	ECARI 6 [µSv]	Etot [µSv]	ECARI 6/Etot
3	CRJ	72.3	141	132(16)	1.07
5	CRJ	39.2	80	72(17)	1.11
6	CRJ	64.1	133	143(14)	0.93
7	CRJ	39.9	81	81(8)	1.00
14	CRJ	71.2	155	190(44)	0.82
16	CRJ	27.5	43	56(13)	0.77
18	CRJ	67.8	120	128(79)	0.94
19	CRJ	27.2	88	84(34)	1.05
20	CRJ	67.8	157	179(44)	0.88
22	CRJ	37.8	104	68(9)	1.53
23	CRJ	62.0	146	153(30)	0.95
25	CRJ	61.9	179	175(15)	1.02
28	CRJ	55.0	130	150(12)	0.87
29	CRJ	28.9	66	68(13)	0.97
34	CRJ	64.2	126	145(11)	0.87
37	CRJ	41.8	79	87(36)	0.91
2	F70/100	89.5	197	209(19)	0.94
4	F70/100	41.6	121	115(19)	1.05
9	F70/100	44.3	84	174(34)	0.48
10	F70/100	45.9	86	77(9)	1.12
13	F70/100	60.5	157	142(11)	1.11
15	F70/100	47.1	141	95(8)	1.48
26	F70/100	59.7	144	154(12)	0.94
27	F70/100	75.4	161	157(39)	1.03
33	F70/100	69.8	141	136(43)	1.04
38	F70/100	58.9	196	184(16)	1.07
8	D8	60.2	40	44(14)	0.91
11	D8	37.7	31	96(36)	0.32
17	D8	37.7	25	49(8)	0.51
40	D8	41.6	36	39(27)	0.92

Table 6-3: Comparison of calculated and measured dose in April/May 2007

#	Fleet	Flight time [h]	ECARI 6 [µSv]	Etot [µSv]	ECARI 6/Etot
3	CRJ	78.4	204	192(14)	1.06
5	CRJ	64.0	146	138(18)	1.06
6	CRJ	95.7	227	293(22)	0.78
7	CRJ	48.8	100	151(14)	0.66
14	CRJ	97.9	262	256(44)	1.02
16	CRJ	109.4	310	307(33)	1.01
18	CRJ	44.5	116	129(34)	0.90
19	CRJ	83.5	176	200(36)	0.88
20	CRJ	80.5	213	229(66)	0.93
23	CRJ	46.1	117	123(29)	0.95
28	CRJ	64.2	157	254(23)	0.62
29	CRJ	90.9	221	226(23)	0.98
34	CRJ	98.2	264	276(31)	0.96
2	F70/100	94.5	307	321(78)	0.96
4	F70/100	34.6	97	99(19)	0.98
9	F70/100	112.0	359	374(75)	0.96
12	F70/100	75.5	230	320(34)	0.72
26	F70/100	140.9	431	558(36)	0.77
30	F70/100	61.8	195	220(38)	0.89
32	F70/100	42.5	129	188(27)	0.69
33	F70/100	95.3	274	343(31)	0.80
38	F70/100	95.7	280	237(20)	1.18
39	D8	67.0	62	102(15)	0.61
40	D8	94.2	70	117(19)	0.60

Table 6-4: Comparison of calculated and measured dose in July/August/September 2007

#	Fleet	Flight time [h]	ECARI 6 [µSv]	Etot [µSv]	ECARI 6/Etot
3	CRJ	82.1	196	233(31)	0.84
5	CRJ	53.3	126	100(21)	1.26
14	CRJ	140.2	350	301(85)	1.16
16	CRJ	107.2	270	270(39)	1.00
18	CRJ	128.3	318	306(142)	1.04
20	CRJ	40.0	97	157(24)	0.62
23	CRJ	22.1	45	61(16)	0.74
25	CRJ	42.8	108	154(15)	0.70
28	CRJ	78.9	182	246(73)	0.74
29	CRJ	55.7	129	137(24)	0.94
34	CRJ	93.4	225	223(33)	1.01
1	F70/100	139.0	265	207(51)	1.28
4	F70/100	66.8	169	205(28)	0.82
13	F70/100	89.1	191	231(43)	0.83
30	F70/100	87.9	260	256(39)	1.02
32	F70/100	75.8	214	340(66)	0.63
38	F70/100	75.8	192	212(26)	0.91
8	D8	124.9	109	112(33)	0.97
40	D8	76.1	61	153(77)	0.40

6.5 Results and Accuracy

First heat (February 2007)

In the first evaluation period, the effective doses calculated by CARI 6 were on average 95.3% of the effective doses measured by TLD-600/700 dosemeters. (Table 6-5) The correlation was even better for the jet fleets; on average 99.7%. The calculations for the turboprop flights were on average only 66.6% of the measured effective doses. The standard deviation of the ratio between the calculated and measured effective doses was 23.4% for all fleets, 19.6% for jet fleets and 25.8% for the turboprop fleet. Five out of 30 dosemeters revealed a difference of more than 30%. Three of these outliers were from jet measurements. Of these, two had a significantly higher and one a lower calculated effective dose compared with the measurement. The further two outliers from the turboprop measurements, were both lower than the measured effective doses. The results of the individual assessments are presented in Figure 6-2.

Table 6-5: Average relation of calculation and measurement and its standard deviation in the 1st period

Fleets	$E_{CARI\ 6}/E_{tot}$ [%]	$\sigma(E_{CARI\ 6}/E_{tot})$ [%]
all fleets	95.30	23.43
Jet-fleets	99.71	19.61
Dash 8 fleet	66.63	25.84

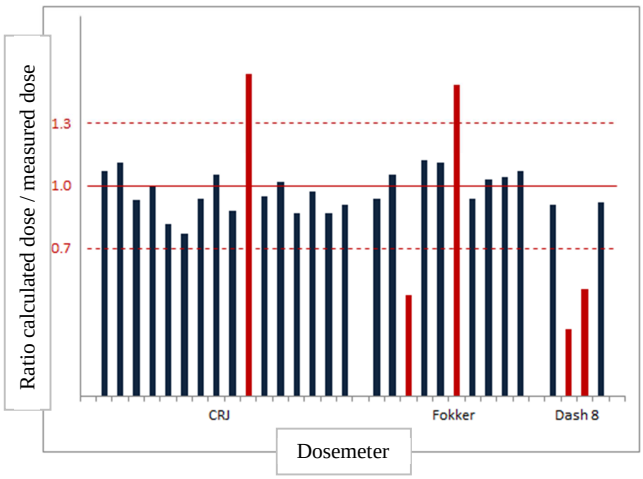

Figure 6-2: Relation between calculated and measured effective dose in the first period

Second heat (April/May 2007)

In the second evaluation period, the effective doses calculated by CARI 6 were on average 87.3% of the effective doses measured by TLD-600/700 dosemeters (Table 6-6). The correlation was even better for the jet fleets; on average 89.7%. The calculations for the turboprop flights were on average only 60.3% of the measured effective doses. The standard deviation of the ratio between the calculated and measured effective doses was 15.8% for all fleets, 14.2% for jet fleets and 0.5% for the turboprop fleet. The low standard deviation of the turboprop fleet assessment can be explained by the low sample size. Four out of 24 dosemeters revealed difference of more than 30%. Two of these outliers were from jet measurements with lower calculated effective dose compared with the measurement. The further two outliers were from the turboprop measurements and showed also lower measured effective doses. The results of the individual assessments are presented in Figure 6-3.

Table 6-6: Average relation of calculation and measurement and its standard deviation in the 2nd period

Fleets	$E_{CARI\ 6}/E_{tot}$ [%]	$\sigma(E_{CARI\ 6}/E_{tot})$ [%]
all fleets	87.29	15.81
Jet-fleets	89.74	14.16
Dash 8 fleet	60.3	0.50

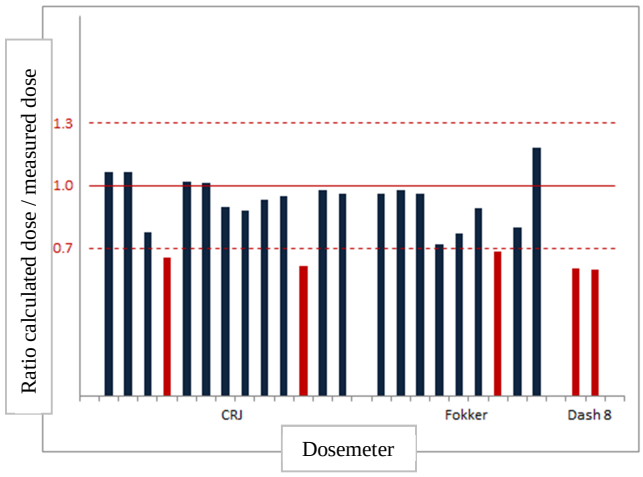

Figure 6-3: Relation between calculated and measured effective dose in the second period

Third heat (July/August/September 2007)

In the third evaluation period, the effective doses calculated by CARI 6 were on average 89.0% of the effective doses measured by TLD-600/700 dosemeters. (Table 6-7) The correlation was even better for the jet fleets; on average 91.4%. The calculations for the turboprop flights were on average only 68.7% of the measured effective doses. The standard deviation of the ratio between the calculated and the measured effective doses was 22.0% for all fleets, 19.7% for jet fleets and 28.8% for the turboprop fleet. Three out of 19 dosemeters revealed difference of more than 30%. Two of these outliers were from jet measurements with lower calculated effective doses compared with the measurement. The outlier from the turboprop measurements also had lower calculated dose. The results of the individual assessments are presented in Figure 6-4.

Table 6-7: Average relation of calculation and measurement and its standard deviation in the 3rd period

Fleets	$E_{CARI\ 6}/E_{tot}$ [%]	$\sigma(E_{CARI\ 6}/E_{tot})$ [%]
all fleets	89.03	21.97
Jet-fleets	91.42	19.69
Dash 8 fleet	68.65	28.75

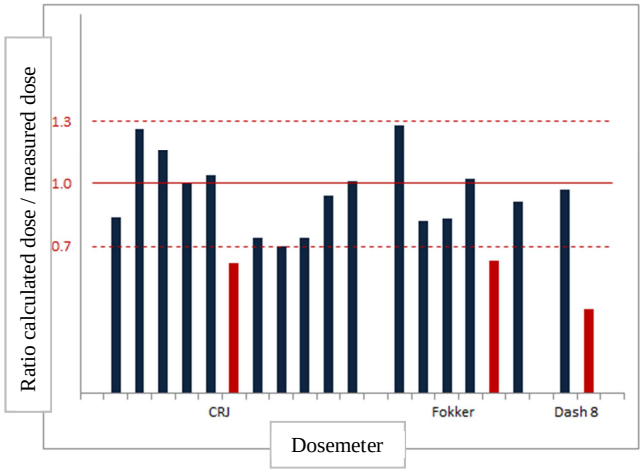

Figure 6-4: Relation between calculated and measured effective dose in the third period

6.6 Summary

The results within this thesis are satisfying with regard to the fact that the statistical uncertainty is indirectly proportional to the accumulated dose and therefore higher for short range operations. On average the accuracy of the calculated compared to the measured effective dose for all fleets was below 24% and, therefore the computational method, CARI 6, complies with legal requirements. The agreement between measurement and simulation was even better for the Canada Regional Jet and the Fokker 70/100 fleet. Both jet fleets operate on similar routes and have the same standard cruising altitudes of 33,000 to 35,000 feet above main sea level.

The agreement between measurement and simulation for the turboprop Dash 8 is worse due to the shorter routes and lower flight altitude of 25,000 feet. Hence, the measured signal from cosmic radiation was close to the measurement signal from the environmental background radiation and the radiation of X-ray scans which complicates reliable measurements. Further, regular positioning flights of crew members could lead to a significantly higher dose than expected for the number of actively flown flights.

On short range flights, especially on the ultra-short Dash 8 operation, the actual flight-route differs significantly from the geodesic route and it is possible that a departure and/or arrival routes is longer

than the remaining flight route. Further, the time spent in low altitudes is underestimated by the computational assessment because arrival transitions of congested airports are often flown in lower altitudes. The computational assessment does not consider that a significant part of the flight could be below the standard flight profile. These effects could lead to an overestimated calculated flight dose, because the exact time of the cruise flight phase was documented only occasionally. A more precise data assessment can be achieved by coupling the measurement with – implemented – flight data monitoring systems. Such systems were not available for this thesis.

To assess the dose rate per flight hour the effective doses from the CARI 6 calculation and thermoluminescence measurement were divided by the actual flight hours of the respective aircrew member. The estimated maximum, minimum and the mean dose rate in this study for a given fleet in a particular measurement period is shown in Table 6-8.

Table 6-8: Calculated and measured effective dose rate per flight hour [µSv/h]

Fleet		1st assessment period		2nd assessment period		3rd assessment period	
		CARI 6 [µSv/h]	Measurement [µSv/h]	CARI 6 [µSv/h]	Measurement [µSv/h]	CARI 6 [µSv/h]	Measurement [µSv/h]
CRJ	Max	3.24	3.09	2.83	3.96	2.52	3.93
	Min	1.56	1.80	2.05	2.16	2.04	1.88
	Mean	2.23	2.30	2.48	2.79	2.39	2.73
Fokker	Max	3.33	3.93	3.25	4.42	3.25	4.42
	Min	1.87	1.68	2.80	2.48	2.05	2.16
	Mean	2.44	2.48	3.04	3.54	2.68	3.16
Dash 8	Max	0.87	2.55	0.93	1.52	0.87	2.01
	Min	0.66	0.73	0.74	1.24	0.80	0.90
	Mean	0.75	1.38	0.83	1.38	0.84	1.45

The distributions of the calculated and measured effective dose rates are demonstrated in Figure 6-5 and Figure 6-6. The calculated as well as measured effective dose rate of the jet pilots are between 2 and 3.3 $\mu Sv h^{-1}$. Under the assumption of about 750 flight hours per anno an average yearly effective dose of about 1.5 to 2.5 mSv can be estimated. Another relative maximum is shown at a range of about 0.8 µSv for pilots on the turboprop fleet (Dash 8). This yields to an extrapolated annual dose between 0.5 and 0.9 mSv on this fleet. The thermoluminescence assessments show additional higher measurements up to 4.4 $\mu Sv h^{-1}$. A possible explanation could be that these DOSFLIP packages were carried by pilots shuttling to their home base by air travel or had regularly positioning flights. It would be also conceivably that these participants took their dosemeters on (long-range) flights during vacations. In any case, these participants did not document these contingently private flights, so that the additional dose did not appear in the CARI 6 assessment. Including these high outliers, the upper limit of the measured dose rate is 4.42 µSv/h. Even, with the

maximum allowed flight hours per year of 900 hours an upper bound of an annual effective dose at 4.0 mSv can be assured. Hence, the flight crew members of *Tyrolean Airways* can be classified as "category B – occupationally exposed personnel", according to "Allgemeine Strahlenschutzverordnung, BGBl. II Nr. 191/2006".

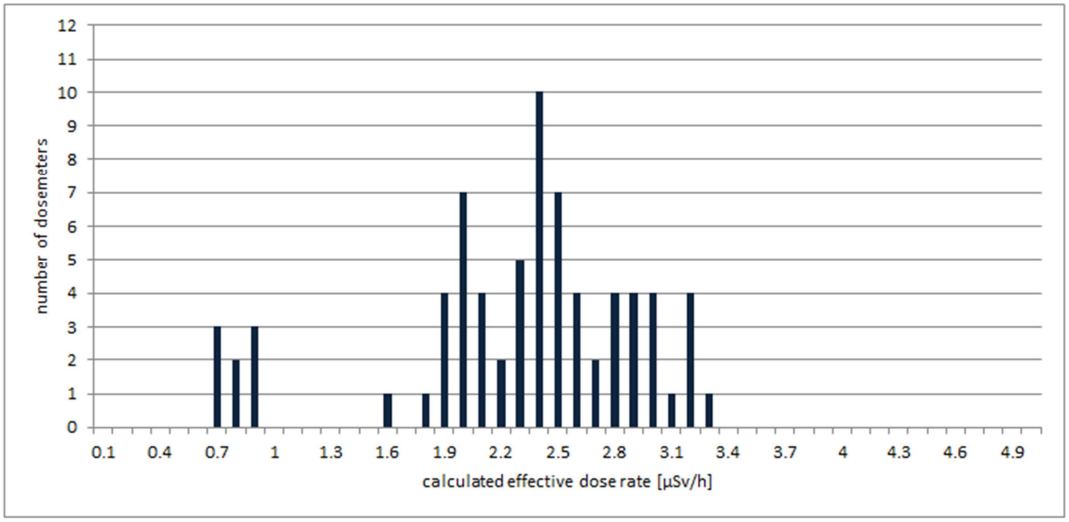

Figure 6-5: Histogram of the radiation exposure of flight crew members according to CARI 6 calculations

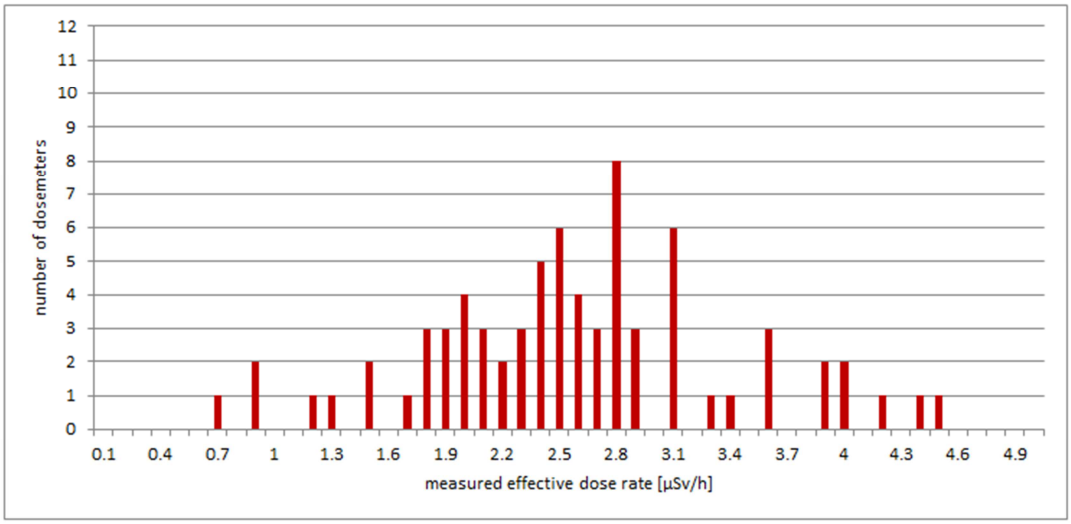

Figure 6-6: Histogram of the measured radiation exposure of flight crew members

Chapter 7

Discussion

In this study the radiation exposure of aircrew members on short- to mid-range flight operation was evaluated. The data acquisition was accomplished by pilots of Tyrolean Airways operating the jet-fleets Fokker 70/100, Canadair Regional Jet CRJ-100/200 and the turboprop fleet Bombardier Dash 8-Q300/400. The experimental and the computational methods used in this six months lasting assessment have proofed to be accurate for measuring radiation exposure of flight crew members. The thermoluminescence dosemeter system DOSFLIP is an excellent tool for radiation measurements. It allows technical measurements of high precision, with an average inherent accuracy (standard deviation) between 2 and 8%. The extended pair method with the lithium fluoride dosemeters TLD-600/700 allows distinguishing between the neutron and non-neutron share of the received dose. The results within this thesis clearly show the expected high neutron share of the measured cosmic radiation at flight altitudes. The assessment with the calcium fluoride dosemeters TLD-300 shows a slightly higher measured absorbed dose than the lithium fluoride dosemeters, which can be explained by their higher thermoluminescence efficiency, especially for protons. The inherent accuracy is comparable to TLD-700. A separate determination of the neutron share of radiation is not possible, due to the lack of a reference calcium fluoride dosemeter, with comparable thermoluminescence properties but other neutron sensitivity. The higher sensitivity is an advantage for measurement of lower radiation doses and shorter time intervals. TLD-300 dosemeters would be ideal for further aviation dosimetry measurements– especially in short range operation, as long as X-ray exposure from artificial sources can be avoided.

The experimental measurement assessment showed the expected results and corresponds with comparable studies. The average effective dose rate of the participants lies in the range of 2 - 3.5 µSv/h. Assuming pilots have 600 to 750 flight hours a year, an annual effective dose

between 1.5 and 2.6 mSv is expected. The radiation exposure of the ultra-short range turboprop operation of the Dash 8 fleet is at the lower end of that range due to lower flight altitudes and shorter flight routes. The computational assessment with CARI 6 showed good accordance with the measurement results. Especially the agreement on the jet-fleets was very accurate. Generally, the computational assessment underestimates the effective dose slightly for jet-flights and considerable for turboprop flights. The differences could be explained, due to the lateral and vertical deviations from the assumed flight routes, as well as additional undocumented (positioning) flights. The average agreement of the computational assessment with CARI 6 and the experimental results was within the limits required by law according to “Strahlenschutzverordnung fliegendes Personal, BGBl. II Nr. 235/2006a”. The agreement was better than the required 30% (on average within 16-25% including some outliers). With regard to the fact that the statistical uncertainty is indirectly proportional to the accumulated dose, and therefore higher on short range operations, the results are rather satisfying. It can be assumed that with a more precise documentation of flight data, the assessment of exact flight routes and a consequent prevention of X-ray scans of dosemeter packages, the accuracy of the assessment methods could be even higher.

Bibliography

[1] EUROPEAN COMMISSION, *Council Directive 96/29/EURATOM of 13 May 1996*, <Official Journal of the European Communities>, (1996).

[2] V.F. HESS, *Über Beobachtungen der durchdringenden Strahlung bei sieben Freiballonfahrten*, <Physikalische Zeitschrift> ‖**13**‖, 1084 (1912).

[3] E.R BENTON, E.V. BENTON, *Space radiation dosimetry in low-Earth orbit and beyond*, <Nuclear Instruments and Methods in Physics Research Section B: Beam Interactions with Materials and Atoms> ‖**184(1-2)**‖, 255 (2001).

[4] J. W. CRONIN, T. K. GAISSER, S. P. SWORDY, *Cosmic Rays* at the *Energy Frontier*, <Scientific American> ‖**276**‖, 44 (1997).

[5] H. J. DE VEGA, N. SANCHEZ, *Extreme Energy Cosmic Rays: Buttom-up vs. Top-down scenarii*, <arXiv:astro-ph/0301039v2>, (2003).

[6] G. REITZ, *Radiation Environment in the Stratosphere*, <Radiation Protection Dosimetry> ‖**48(1)**‖, 5 (1993).

[7] S. P. SWORDY, *The Energy Spectra and Anisotropies of Cosmic Rays*, <Space Science Reviews> ‖**99(1)**‖, 85 (2001).

[8] A. HORNEFFER, *Measuring Radio Emission from Cosmic Ray Air Showers with a Digital Radio Telescope*, Rheinischen Friedrich-Willhelms-Universität Bonn, Dissertation, (2006).

[9] J. P. WEFEL, R. SILBERBERG, M. M. SHAPIRO, *Cosmic Rays, Supernovae and the interstellar Medium*, <NATO ASI series: Mathematical and physical sciences>, Springer, 58 (1991).

[10] J.A. SIMPSON, *Introduction to the Galactic Cosmic Radiation*, <NATO ASIC Proceedings 107: Composition and Origin of Cosmic Rays> ‖**107**‖, 1 (1983).

[11] G. KOPP, G. LAWRENCE, G. ROTTMAN, *The Total Irradiance Monitor (TIM): Science Results*, <Solar Physics> ‖**230(1-2)**‖, 129 (2005).

[12] NATIONAL AERONAUTICS AND SPACE ADMINISTRATION (NASA), http://solarscience.msfc.nasa.gov/SunspotCycle.shtml, (downloaded 19.11.2010).

[13] R. LANZA, A. MELONI, *The Earth's Magnetism*, Springer, (2006).

[14] S. LAMB, D. SINGTON, *Earth Story: The Forces That Have Shaped Our Planet*, Princeton University Press, (2003).

[15] E.G. STASSINOPOULOS, C.A. STAFFER, *Forty-Year Drift and Change of the SAA*, NASA Goddard Spaceflight Center, (2007).

[16] P. LANTOS, The *Sun and its Effects on the Terrestrial Environment,* <Radiation Protection Dosimetry> ‖**48(1)**‖, 27 (1993).

[17] J. F. ZIEGLER, *Terrestrial cosmic ray intensities,* <IBM Journal of Research and Development> ‖**42(1)**‖, 117 (1998).

[18] M.A. SHEA, D.F. SMART, *Geomagnetic cutoff rigidities and geomagnetic coordinates appropriate for the Carrington flare Epoch,* <Advances in Space Research> ‖**38(2)**‖, 209 (2006).

[19] P.E. BAILY, *Neutron Radiation Dosimetry in High Altitude Flight Personnel,* <Aviation, Space, and Environmental Medicine> ‖**53(8)**‖, 808 (1982).

[20] O. C. ALKHOFER, *Introduction to Cosmic Radiation,* Verlag Karl Thieming, (1975).

[21] W-M. YAO ET AL, *Review of Particle Physics,* <Journal of Physics G: Nuclear and Particle Physics> ‖**33(1)**‖, (2006).

[22] C. GEICH-GIMBEL, *Particle Production at Collider Energies,* <International Journal of Modern Physics A> ‖**4(7)**‖, 1527 (1989).

[23] S.H. NEDDERMEYER AND C.D. ANDERSON, *Note on the Nature of Cosmic-Ray Particles,* <Physical Review> ‖**51(10)**‖, 884 (1937).

[24] M. V. S. RAO, B. V. SREEKANTAN, *Extensive Air Showers,* World Scientific, (1998).

[25] R.M. BARNETT ET AL, *Review of particle properties,* <Physical Review D> ‖**54(1)**‖, (1996).

[26] INTERNATIONAL COMMISSION ON RADIATION UNITS AND MEASUREMENTS (ICRU), *IRCU Report 33: Quantities and Units for Use in Radiation Protection,* <Journal of the ICRU>, (1980).

[27] INTERNATIONAL COMMISSION ON RADIATION UNITS AND MEASUREMENTS (ICRU), *IRCU Report 39: Determination of Dose Equivalents Resulting from External Radiation Sources,* <Journal of the ICRU>, (1985).

[28] INTERNATIONAL COMMISSION ON RADIATION UNITS AND MEASUREMENTS (ICRU), *ICRU Report 43: Measurement of Dose Equivalents from External Radiation Sources, Part 2,* <Journal of the ICRU>, (1988).

[29] INTERNATIONAL COMMISSION ON RADIATION UNITS AND MEASUREMENTS (ICRU), *ICRU Report 51: Quantities and Units in Radiation Protection Dosimetry,* <Journal of the ICRU>, (1993).

[30] C. WERNLI, *External Dosimetry: Operational Quantities and their Measurement,* <Proceedings: 11th International Congress of the International Radiation Protection Association (IRPA)>, (2004).

[31] INTERNATIONAL ATOMIC ENERGY AGENCY (IAEA), *Calibration of Radiation Protection Monitoring Instruments,* <IAEA Safety Report Series No 16>, (2000).

[32] R. CARRIER, D. CORMACK: *Historical Overview*, <Physics in Canada> ‖**51(4)**‖, (1995).

[33] ICRP 60, *The 1990 Recommendations of the International Commission on Radiological Protection, Publication 60,* <Annals of the ICRP> ‖**21(1-3)**‖, (1991).

[34] ICRP 103, *The 2007 Recommendations of the International Commission on Radiological Protection, Publication 103,* <Annals of the ICRP> ‖**37(2-4)**‖, (2007).

[35] M. HAJEK, N. VANA, *Applicability of Ambient Dose Equivalent H*(d) in Mixed Radiation Fields - A Critical Discussion*, Proceedings: 11th International Congress of the International Radiation Protection Association (IRPA), (2004).

[36] A. FERRARI, A.FASSÒ, J. RANFT, P.R. SALA, *FLUKA, a multi-particle transport code*, <CERN: INFN/TC 05/11,SLAC-R-773>, (2005).

[37] A. FERRARI, M. PELLICCIONI, T. RANCATI, *Calculation of the radiation environment caused by galactic cosmic rays for determining air crew exposure*, <Radiation Protection Dosimetry> ‖**93(2)**‖, 101 (2001).

[38] G. BADUREK, *Biologische und Medizinische Anwendungen der Kernphysik*, script of lecture: Biological and Medical Applications of Nuclear Physics I)

[39] HONG KONG OBSERVATORY, *Threshold for deterministic effects*, http://www.hko.gov.hk/education/dbcp/rad_health/eng/r4_1.htm, (downloaded 19.11.2010).

[40] LISTER HILL NATIONAL CENTER FOR BIOMEDICAL COMMUNICATIONS, *Mutations and Health*, http://ghr.nlm.nih.gov/handbook/mutationsanddisorders/genemutation, (downloaded 19.11.2010).

[41] NATIONAL CANCER INSTITUTE (U.S. DEPARTMENT OF HEALTH AND HUMAN SERVICES), *somatic mutation*, http://www.cancer.gov/dictionary/?CdrID=46586, (downloaded 19.11.2010).

[42] EUROPEAN NUCLEAR SOCIETY, *Deterministic radiation effect*, http://www.euronuclear.org/info/encyclopedia/d/deterministicradiationedffect.htm, (downloaded 19.11.2010).

[43] F. W. STECKER, *Cosmic physics: the high energy frontier,* <Journal of Physics G: Nuclear and Particle Physics> ‖**29**‖, (2003).

[44] J. CRONIN, T.K. GAISSER, S.P. SWORDY, *Cosmic Rays at the Energy Frontier*, <Scientific American> ‖**276(1)**‖, (1997).

[45] M.L. HEFFERIN, A.E. TOMKINSON, *Mechanism of DNA double-strand break repair by non-homologous end joining*, <DNA Repair> ‖**4(6)**‖, 639 (2005).

[46] K.H. KARLSSON, B. STENERLÖW, *Focus formation of DNA repair proteins in normal and repair-deficient cells irradiated with high-LET ions*, <Radiation Research> ‖161(5)‖, 517 (2004).

[47] O. SÖDERBERG ET AL, *Direct observation of individual endogenous protein complexes in situ by proximity ligation*, <Nature Methods> ‖**3**‖, 995 (2006).

[48] *UNITED NATIONS SCIENTIFIC COMMITTEE* ON THE *EFFECTS OF ATOMIC RADIATION*, Sources and *effects of ionizing radiation*, <UNSCEAR 2000 report> ‖**2**‖, (2000).

[49] M. GUNDESTRUP, H.H. STORM, *Radiation-induced acute myeloid leukaemia and other cancers in commercial jet cockpit crew: a population-based cohort study*, <Lancet> ‖**354**‖, 2029 (1999).

[50] T. HALDORSEN, J.B. REITAN, U. TVETEN, *Cancer incidence among Norwegian airline pilots*, <Scandinavian Journal of Work, Environment & Health> ‖**26(2)**‖, 106 (2000).

[51] T. HALDORSEN, J.B. REITAN, U. TVETEN, *Cancer incidence among Norwegian airline cabin attendants*, <International Journal of Epidemiology> ‖**30(4)**‖, 825 (2001).

[52] A. LINNERSJÖ, *Cancer incidence in airline cabin crew: experience from Sweden*, <Occupational and Environmental Medicine> ‖**60**‖, 810 (2003).

[53] V. RAFNSSON, J. HRAFNKELSSON, Incidence *of cancer among commercial airline pilots*, <Occupational and Environmental Medicine> ‖**57(3)**‖,175 (2000).

[54] V. RAFNSSON ET AL, *Breast cancer risk in airline cabin attendants: a nested case-control study in Iceland*, <Occupational and Environmental Medicine> ‖**60(11)**‖, 807 (2003).

[55] P.R. BAND ET AL, *Cohort Study of Air Canada Pilots: Mortality, Cancer, Incidence, and Leukaemia Risk*, <American Journal of Epidemiology> ‖**143(2)**‖, 137 (1996).

[56] M. BLETTNER ET AL, *Mortality from cancer and other causes among male airline cockpit crew in Europe*, <International Journal of Cancer> ‖**106(6)**‖, 946 (2003).

[57] I. LANGNER ET AL, *Cosmic radiation and cancer mortality among airline pilots: results from a European cohort study (ESCAPE)*, <Radiation and Environmental Biophysics> ‖**42(4)**‖**,** 247 (2004).

[58] H. ZEEB ET AL, *Mortality from Cancer and Other Causes among Airline Cabin Attendants in Europe: A Collaborative Cohort Study in Eight Countries*, <American Journal of Epidemiology> ‖**158(1)**‖, 35 (2003).

[59] B. J. LEWIS ET AL, *Cosmic Radiation Exposure on Canadian-Based Commercial Airline Routes*, <Radiation Protection Dosimetry> ‖**86(1)**‖, 7 (1999).

[60] V. RAFNSSON ET AL, *Risk factors for cutaneous malignant melanoma among aircrews and a random sample of the population*, <Occupational and Environmental Medicine> ‖**60(11)**‖, 815 (2003).

[61] E. PUKKALA ET AL, *Cancer Incidence Among 10,211 Airline Pilots: A Nordic Study*, <Aviation, Space, and Environmental Medicine> ‖**74(7)**‖, (2003).

[62] B.S. EVERITT, *Cambridge Dictionary of Statistics*, Cambridge University Press, (2002).

[63] C.L. SISTROM, C.W. GARVAN: *Proportions, Odds, and Risk*, <Radiology> ‖**230(12-19)**‖, (2004).

[64] M.J. SCHERVISH, *P Values: What They Are and What They Are Not*, <American Statistician> ‖ **50(3)**‖, 203 (1996).

[65] D. SCHOTTENFELD, J.F. FRAUMENI JR., *Cancer Epidemiology and Prevention (2nd edition)*, Oxford University Press, 319 (1996).

[66] B.L. DIFFEY, A.H. ROSCOE, *Exposure to solar ultraviolet radiation in flight*, <Aviation, Space, and Environmental Medicine> ‖**61(11)**‖**,** 1032 (1990).

[67] O. SARENIO, *Ermittlung der durch kosmische Strahlung verursachten Strahlenexposition des fliegenden Personals*, <Berichteder Strahlenschutzkommission> ‖**35**‖**,** (2003).

[68] N. RIEHL ET AL, *Einführung in die Lumineszenz (Introduction to Luminescence)*, Verlag Karl Thiemig, (1971).

[69] S.W.S. MCKEEVER, *Thermoluminescence of solids*, Cambridge University Press, (1988).

[70] L. BØTTER-JENSEN, S.W.S MCKEEVER, A.G. WINTLE, *Optically Stimulated Luminescence Dosimetry*, Elsevier, (2003).

[71] M. HAJEK, T. BERGER, N. VANA, M. FUGGER, *A TLD-Based Personal Dosemeter System for Aircrew Monitoring*, <Radiation Protection Dosimetry> ‖**110(1-4)**‖, 337 (2004).

[72] W. SCHÖNER, N. VANA, M. FUGGER, *The LET dependence of LiF:Mg,Ti dosemeters and its application for LET measurements in mixed radiation fields*, <Radiation Protection Dosimetry> ‖**85(1-4)**‖, 263 (1999).

[73] M. HAJEK, T. BERGER , W. SCHÖNER, N. VANA, *Comparison of Measurements with Active and Passive Bonner Sphere Spectrometers*, <Transactions of the American Nuclear Society> ‖**83**‖, 263 (2000).

[74] N. VANA, EL AL, *A computerised TL read out system for data and phototransfer measurements*, <International Journal of Radiation Applications and Instrumentation. Part D. Nuclear Tracks and Radiation Measurements>, ‖**14(1-2)**‖, 181 (1988).

[75] M. HAJEK, T. BERGER, W. SCHÖNER ET AL, *LET dependence of thermoluminescent efficiency and peak height ratio of CaF_2:Tm*, <Radiation Measurement> ‖**43**‖, 1135 (2008).

[76] M. HAJEK, *Applied neutron spectrometry – applications atop high-altitude mountains and onboard aircraft*, Technische Universität Wien, Dissertation, (2002).

[77] A. MITAROFF, M. SILARI, *The Cern-EU high-energy Reference Field (CERF) Facility for Dosimetry at Commercial Fight Altitudes and in Space*, <Radiation Protection Dosimetry> **‖102(1)‖**, 7 (2002).

[78] P. BILSKI, P. OLKO, T. HORWACIK, *Air-crew exposure to cosmic radiation on board of Polish passenger aircraft*, <Nukleonika> **‖49(2)‖**, 77 (2004).

[79] D.T. BARTLETT, *Measurements on Concorde of the Cosmic Radiation Field at Aviation Altitudes*, <Radiation Protection Dosimetry> **‖91(4)‖,** 365 (2000).

[80] E.R. BENTON, A.L. FRANK., E.V. BENTON, *TLD efficiency of ^{7}LiF for dose deposited by high-LET particles*, <Radiation Measurements> **‖32(3)‖**, 211 (2000).

[81] P. LANTOS, N. FULLER, J.F. BOTTOLLIER-DEPOIS, *Methods for estimating radiation doses received by commercial aircrew*, <Aviation, Space, & Environmental Medicine> **‖74(7)‖**, 746 (2003).

[82] G. BATTISTONI EL AL, *The FLUKA code: Description and benchmarking, Proceedings of the Hadronic Shower Simulation Workshop 2006*, <AIP Conference Proceeding> **‖896‖**, 31 (2007).

[83] J. R. DAVIS, R. JOHNSON, J. STEPANEK, *Fundamentals of Aerospace Medicine*, Lippincott Williams & Wilkins, 228 (2008).

[84] K. O'BRIEN ET AL, *World-wide radiation dosage calculations for air crew members*, <Advances in Space Research> **‖31(4)‖**, 835 (2003).

[85] M. HAJEK, T. BERGER, M. FÜRSTNER ET AL, *BRADOS – Dose determination in the Russian Segment of the International Space Station*, <Advances in Space Research> **‖37(9)‖**, 1664 (2006).

[86] M. HAJEK, T. BERGER, N. VANA, *Extended pair method for neutron dosimetry at high atmospheric altitudes*, <Transactions of the American Nuclear Society> **‖89‖**, 750 (2003).

[87] J.F. BOTTOLLIER-DEPOIS ET AL, *An operational approach for aircraft crew dosimetry: the SIEVERT system*, <Radiation Protection Dosimetry> **‖125(1-4)‖**, 421 (2007).

[88] FEDERAL AVIATION ADMINISTRATION (FAA), *Heliocentric Potential*, http://www.faa.gov/data_research/research/med_humanfacs/aeromedical/radiobiology/heliocentric/, (downloaded 19.01.2009).

List of Figures

List of Tables